

Ab-Initio Investigations of Fundamental Adsorption Mechanisms of Organic Molecules on Solid Surfaces

Dissertation

zur Erlangung des akademischen Grades
doctor rerum naturalium (Dr. rer. nat.)

vorgelegt dem Rat der Physikalisch-Astronomischen Fakultät
der Friedrich-Schiller-Universität Jena

von Dipl.-Phys. Martin Preuß
geboren am 5. November 1976 in Stadthagen

Gutachter:

1. Prof. Dr. F. Bechstedt, Friedrich-Schiller-Universität Jena
2. Prof. Dr. P. Krüger, Westfälische Wilhelms-Universität Münster
3. Prof. Dr. G. P. Srivastava, University of Exeter

Tag der letzten Rigorosumsprüfung: 31. Januar 2007

Tag der öffentlichen Verteidigung: 6. Februar 2007

ἐπεὶ δὲ τὸ ἕκ τινος σύνθετον οὕτως ὥστε ἓν εἶναι τὸ πᾶν,
ἀλλὰ μὴ ὡς σωρὸς ἀλλ' ὡς ἡ συλλαβή.

Aristoteles, *Metaphysik* (Buch VII, Kap. 17, 1041b)

Contents

1	Introduction	1
1.1	Motivation	1
1.2	Sources of information	2
1.3	Outline	3
2	Theoretical background and numerical methods	6
2.1	Foundations of density-functional theory	6
2.1.1	Born-Oppenheimer approximation	6
2.1.2	Hohenberg-Kohn theorem and Kohn-Sham formalism	7
2.1.3	Total energy and Hellmann-Feynman forces	9
2.1.4	Exchange-correlation functionals	9
2.1.5	The gap problem in density-functional theory	10
2.1.6	Delta-self-consistent field method	11
2.2	Implementation	12
2.2.1	Frozen core approximation and pseudopotentials	13
2.2.2	Plane-wave expansion and Brillouin-zone integration	14
2.3	Supercell approach	16
2.3.1	Repeated slabs	16
2.3.2	Monopole and dipole corrections	17
2.3.3	Symmetry and modeling	19
2.4	Adsorbate and substrate vibrations	23
2.5	Technical parameters of the calculations	25
3	Methylchloride adsorption on Si(001)	27
3.1	Adsorption geometries and energies	27
3.2	Charge transfer	29
3.3	Bandstructures	30
3.4	Surface dipoles	33
4	Pyrrrole-functionalized SiC surfaces	35
4.1	Surface core-level shifts	35
4.2	X-ray photoelectron spectra	37
4.3	Relation between adsorption energy and desorption temperature	38
4.4	Clean surfaces	39
4.5	Pyrrrole-adsorbed surfaces	40
4.5.1	Phase diagrams	41

4.5.2	Dissociated structures	42
4.5.3	Intact structures	43
5	Vibrational spectra of NH₃, C₆H₆, and C₆H₆/Si(001)	46
5.1	Ammonia	46
5.2	Benzene	48
5.3	Benzene adsorbed on Si(001)	51
6	Properties of perylene adsorbed on Si(001)	55
6.1	Vibrational spectrum of perylene	55
6.2	Adsorption structures	57
6.3	STM images	60
6.4	HREEL spectra	61
7	Adenine adsorbed on Cu(110)	64
7.1	Single-molecule adenine on Cu(110)	64
7.1.1	Adsorption geometry and energy	64
7.1.2	Nature of the amino-group–metal bond	66
7.2	Adenine rows on Cu(110)	68
7.2.1	Adenine dimers	68
7.2.2	Adsorption geometry and energy of dimer chains	69
7.2.3	STM images	71
8	Summary	74
	Bibliography	77
	Publications	84
	Zusammenfassung	87

Chapter 1

Introduction

1.1 Motivation

The formation of organic thin films on crystal surfaces has attracted much attention in the surface science community during the last years, from both a fundamental and practical point of view [1–3]. Many organic molecules consist of specific atomic arrangements that will react similarly. The existence of these functional groups explains the central role that is attributed to the concept of organic functionalization: it consists of imparting some of the molecular functionality to well-characterized surfaces in a controlled way. In particular, this method is becoming an indispensable tool for the development of semiconductor-based devices. This technique comprises the possibility to overcome the size-limitations inherent to current-day silicon-based transistors by contacting source and drain with a molecular gate. Hereby interactions at a sub-nanometer scale are beginning to dominate the functionality of such devices. This has stimulated intensive research on the phenomena at an atomic level that occur directly in the interface regions. The intrinsic variability of organic overlayers opens up the prospect of tailoring the properties of the hybrid device more easily than with traditional inorganic materials. The success of this approach has already been demonstrated by the fabrication of organic light-emitting diodes covering the entire visible spectral range [4].

From the surface science point of view, the formation of ordered molecular overlayers is desirable because well-established surface-sensitive techniques can be used to characterize the interface. Long-range order on Si(001) surfaces has been observed especially for alkenes that form cycloaddition products between the π bonds of the surface dimers and the carbon-carbon double bonds [5–7]. However, also dissociative reactions such as NH cleavage [8] or dative bonding [9, 10] may result in ordered interface structures. In the latter pathway the molecule donates both of the electrons necessary for the formation of a covalent bond, thus it is likely to occur for molecules with lone-pair orbitals.

In contrast to the bonding to semiconductors where strong covalent bonds prevail, the attachment of molecules to metal surfaces is governed by relatively weak interactions due to the non-existence of directed dangling bonds at the surface. This simplifies the emergence of self-organized structures that are stabilized mostly by intermolecular interactions. Studies have shown the formation of nearly defect-free overlayers that exhibit a long-range order over tens or hundreds of nanometers [11–13]. These systems are exam-

ined to aid in the understanding of complex intermolecular processes which are deemed important, e. g., in the origin of life research [14].

1.2 Sources of information

There are a variety of direct and indirect methods to elucidate surface and interface structures. The dispersion of surface states in the Brillouin zone can be determined by photoemission (PE) or inverse photoemission (IPE) spectroscopy to obtain information on occupied or unoccupied bands, respectively. Density-functional theory (DFT) calculations are a powerful means to aid in the interpretation of the resulting bandstructures. The analysis of the calculated density of states in the energy range of the valence electrons allows for a detailed examination of the electronic levels of a system near the Fermi edge. The deep-lying core states, although not participating in the chemical bonding, experience subtle changes upon the change of the local chemical environment that can be rationalized by the theoretical and experimental determination of core-level shifts. Among the most prominent experimental approaches are low-energy electron diffraction (LEED) for the elucidation of the surface periodicity, scanning tunneling microscopy (STM) for imaging the local electronic density of states, and vibrational spectroscopy, which is indeed one of the most powerful experimental techniques for the characterization of materials [15, 16]. There is such a wealth of information on the vibrational properties of molecules and adsorbate complexes that, over the decades, a large database of wavenumbers and eigenvectors of molecular vibrations has become available to researchers working both in chemistry and physics. The usefulness of these data lies in the fact that the vibrations can be classified according to a relatively simple scheme consisting of only a few number of characteristic types of vibrations, e. g., bending, stretching, rocking, and wagging modes, each of which have, depending on the species of the involved atoms, characteristic frequencies. Thus vibrational spectroscopy not only probes the symmetry and the geometry of the atomic arrangement in question, but also, to a certain extent, the chemical composition. Thereby it provides insight into such complex issues as bonding mechanisms and adsorbate-substrate interactions.

The most important experimental techniques subsumed under the generic term “vibrational spectroscopy” are optical infrared (IR) spectroscopy, where light in the infrared region is shone on the sample, and high-resolution electron energy loss spectroscopy (HREELS) which probes the vibrations at the surface with a low-energy electron beam. The underlying physical process of IR spectroscopy is the coupling of the incident electric field to the dipoles accompanying the excitation of vibrational modes. This gives rise to resonant absorption peaks in dependence on the primary photon energy. In the case of normal incidence only in-plane dipoles are probed. HREEL spectroscopy, on the other hand, exploits the effect of inelastic scattering of the incident electrons from the long-range dipole field above the crystal where the scattering is strongest in forward direction [17]. Due to the grazing incidence geometry in which HREEL experiments are mainly carried out this method dominantly probes vibrational dipoles perpendicular to the surface. Common to both kinds of spectroscopy is that excitations of vibrational

modes are associated with vanishing or small momentum transfer so that zone-center optical modes are observed. Moreover, they are subject to the same selection rules [18].

Because of the complexity of either an IR or an HREEL spectrum the assignment of vibrational modes is usually not straightforward. However, the knowledge of vibrational eigenfrequencies and eigenvalues from theory allows to interpret the peak structures of an experimental spectrum. This is where DFT calculations prove especially helpful. Vibrational frequencies calculated within the harmonic approximation are usually reproduced within an error bar of less than 4%. The *first-principles* DFT approach allows for the realistic modeling of surface and adsorbate systems without any empirical input parameters besides the species and positions of the constituting atoms. Thus such calculations not only serve to reproduce and confirm or confute experimental conjectures, but to provide detailed insights into physical mechanisms that are not easily accessible in the measurements. For example, the normal modes corresponding to a vibrational transition can be easily visualized and assigned to a certain group of the molecule.

In addition to the frequencies and normal modes the intensities of the vibrational transitions are crucial for the identification of characteristic features in a spectrum. These intensities are directly related to a dynamical dipole which corresponds to the change of the total dipole moment of the system as a response to a distortion along a certain normal mode. One major result of the present thesis is the development, implementation and application of an easy yet accurate method for the calculation of the dynamical dipoles in the framework of DFT with periodic boundary conditions which paves the way for the straightforward prediction of complete vibrational spectra including the transition intensities.

1.3 Outline

This thesis is organized as follows. In Chapter 2 an overview of the theoretical background of DFT and the numerical methods is given; the newly implemented approach to the calculation of a full vibrational spectrum is presented in Sec. 2.4. Chapters 3–7 contain the results obtained for the examined adsorption systems. The thesis concludes with a summary in Chapter 8.

In Chapter 3 we study the interaction of methylchloride with the Si(001) surface. This interface has been investigated by electron energy loss spectroscopy, Auger electron spectroscopy, and temperature programmed desorption as well as scanning tunneling microscopy [19–21]. From the experiments it was concluded that methylchloride adsorbs dissociatively on Si(001). Here we focus in particular on the interplay between surface bonding and surface electronic properties of the energetically most relevant interface geometries.

In Chapter 4 the bonding mechanisms of pyrrole-adsorbed SiC surfaces are elucidated. The system is experimentally characterized by LEED, STM, and x-ray photoelectron spectroscopy (XPS) [22]. The subject was inspired by the prospect of future sensing applications using organically functionalized surfaces that obtain sensitivity towards chemical stimuli by imparting molecular functionality onto the substrate. If such hybrid systems are to be used, however, as highly selective sensors *in vivo*, non-toxicity in the

living organism must be assured which leads to the demand of biocompatibility [23]. Silicon carbide (SiC) is a promising candidate for such applications because it is mechanically extremely stable and indeed biocompatible. The electronic properties of SiC can be tailored due to the large number of possible polytypes simply by variation of the SiC bilayer stacking along the [111] or [0001] direction. Pyrrole has been chosen because it is a small aromatic molecule, resulting in a relatively limited number of conceivable bonding possibilities on SiC. Moreover, it possesses as functional units an NH-group and two carbon-carbon double bonds which may be used for further functionalization of the surface.

In Chapter 5 the newly implemented method for the calculation of IR and HREEL spectra is practically applied and tested for the isolated molecules ammonia and benzene. A major part of the elaborations is dedicated to the role of the symmetry and its relation to the vibrational spectra concerning the normal modes and the allowed transitions. Afterwards we proceed to the more complicated, but well-characterized system of benzene adsorbed on Si(001) which we consider as a benchmark problem.

In Chapter 6 we scrutinize the adsorption of perylene on Si(001) in order to understand the molecule-surface interaction. Perylene is an interesting model system because it consists of five six-membered carbon rings which define its aromaticity and π -conjugated character. Moreover, perylene constitutes the core of the widely known organic semiconductor 3,4,9,10-perylene-tetracarboxylic dianhydride (PTCDA), but is easier in that it lacks the carboxylic anhydride functionality. Many studies [24–26] have shown that PTCDA adsorbs in an essentially flat-lying fashion on many different substrates where the interaction between adsorbate and substrate is mainly mediated by dispersion forces [27,28]. Perylene, on the other hand, apparently adsorbs on Si(001) more or less vertically and establishes a strong covalent bond to the surface [29]. A variety of model geometries is analyzed with respect to the structural, energetic, and spectroscopic properties. It turns out that only a combination of these fingerprints permits the unambiguous identification of the realized adsorption structure.

In the first Section of Chapter 7 the question is tackled of what governs the bonding between the molecular amino group of adenine and copper surfaces. This system has been chosen because it is well characterized by scanning tunneling microscopy, low-energy electron diffraction and electron energy loss spectroscopy [11,30]. The amino-group-metal bond is of particular interest and has given rise to a number of interpretations. Experimentally as well as theoretically relatively low energy gains upon bonding between molecular amino groups and metal substrates are found. For ammonia on Cu(110) an adsorption energy of 0.78 eV was calculated and explained by both covalent and ionic contributions [31]. A similar energy is reported for the bond formed between the amino group of glycine and the Cu(110) surface [32] which has been interpreted in terms of formation and partial occupation of bonding and antibonding combinations of the $N2p_z$ orbital with the metal valence d band. We argue here that the bonding between adenine and Cu(110) is not covalent, but can nevertheless be explained within a simple and intuitive picture: The charge transfer from the molecule to the substrate as well the mutual polarization of the amino-group N lone pair of electrons and the metal substrate lead to a preferred-site interaction that largely accounts for the bonding energy calculated from *first principles*. The second part of this Chapter is devoted to the identification

of the driving forces that govern the formation of self-assembled adenine chains on the Cu(110) surface as observed in scanning tunneling microscopy images [11]. Additional diffraction results show the emergence of a long-range order that can be described with a surface unit cell commensurate with the underlying substrate. Moreover, the diffraction pattern indicates that two adenine molecules, rotated against each other by 180° , dimerize in one unit cell.

Chapter 2

Theoretical background and numerical methods

2.1 Foundations of density-functional theory

An accurate description of a many-particle system on an atomic scale must be invariably based on quantum mechanics. Even a seemingly simple system like the hydrogen atom is beyond the reach of a classical treatment because in Newtonian mechanics the concept of stationary states is inherently unknown so that the explanations of the stability and the spectral features as discontinuous transitions between these states remain elusive.

Where the Schrödinger equation for the hydrogen atom can be solved analytically, this is impossible for a many-atom molecule or an extended solid state body. The interaction of the electrons is responsible for the major physics of these systems – therefore the corresponding wave function does not factorize which even hampers a direct numerical solution. Only physically sensible approximations allow for tackling these problems with justifiable effort.

2.1.1 Born-Oppenheimer approximation

In the Born-Oppenheimer approximation [33] the electronic and ionic problem are treated separately: The nuclei of the atoms are much heavier than the surrounding electrons so the kinetic energy of the nuclei is much smaller than that of the electrons. It is therefore sensible to assume that the electrons instantaneously follow the motion of the ions. This means that for every atomic configuration the electron distribution follows from the Schrödinger equation for *fixed* atomic positions \mathbf{R}_k which enter the Hamiltonian of the electronic problem parametrically by means of the attractive electrostatic potential that an electron at position \mathbf{r} experiences,

$$V_{\text{e-ion}}(\mathbf{r}) = - \sum_k \frac{Z_k e^2}{|\mathbf{r} - \mathbf{R}_k|}, \quad (2.1)$$

where Z_k denotes the nuclear charge number and e the electron charge. The electronic Hamiltonian consists of three major parts, the kinetic energy T of the electrons, the po-

tential energy V of the electrons in the field of the nuclei plus possible external potentials, and the operator of the electron-electron interaction U :

$$\hat{H} = \hat{T} + \hat{V} + \hat{U}. \quad (2.2)$$

A priori the operator \hat{U} contains contributions from the transverse interaction of the electrons mediated by a vector potential the sources of which are the magnetic moments of the nuclei, the spin moments of the electrons and the associated currents. Diamagnetic systems, however, for which the expectation value of the current density vanishes in the ground state, are sufficiently characterized by keeping only the longitudinal Coulomb repulsion,

$$v(\mathbf{r} - \mathbf{r}') = \frac{e^2}{|\mathbf{r} - \mathbf{r}'|}. \quad (2.3)$$

The Hamilton operator of the electronic systems therefore reads

$$\hat{H} = \sum_i \left\{ -\frac{\hbar^2}{2m} \Delta_i + V^{\text{ext}}(\{\mathbf{R}_k\}; \mathbf{r}_i) + \frac{1}{2} \sum_{j \neq i} \frac{e^2}{|\mathbf{r}_i - \mathbf{r}_j|} \right\} \quad (2.4)$$

where the external potential V^{ext} is understood to encompass $V_{\text{e-ion}}$; the parametric dependence on the positions of the nuclei is indicated by $\{\mathbf{R}_k\}$. The electron mass is denoted by m and the Laplace operator with respect to \mathbf{r}_i by Δ_i . Generalizations of the Hamiltonian (2.4) with regard to, e. g., explicit spin dependence to account for spin-orbit coupling or other relativistic effects like non-collinear magnetism, are of course possible, but will not be pursued here. Furthermore, we will assume spin degeneracy.

2.1.2 Hohenberg-Kohn theorem and Kohn-Sham formalism

The many-electron system characterized by the Hamiltonian (2.4) is, in general, far too large to be solved directly by wave function based methods like Hartree-Fock [34] or Møller-Plesset [35]. Another approach are the *density functional* methods: instead of the many-particle wave function the electron density becomes the fundamental quantity on which the salient properties depend, most notably the total energy. Empirically, already in 1927 Thomas and Fermi [36, 37] suggested the description of the electronic system by a density functional. In 1964 Hohenberg and Kohn [38] showed in the eponymous theorem that for every interacting many-electron system the electronic energy is a functional of the electron density,

$$E = E[n(\mathbf{r})] = F[n(\mathbf{r})] + \int d\mathbf{r} n(\mathbf{r}) V^{\text{ext}}(\{\mathbf{R}_k\}; \mathbf{r}), \quad (2.5)$$

with the *universal* (but unknown) functional $F[n(\mathbf{r})]$. The second part of the Hohenberg-Kohn theorem states that the energy functional (2.5) assumes its minimum E_0 at the groundstate electron density $n_0(\mathbf{r})$. Hohenberg and Kohn originally formulated and proved the theorems under the assumption of a non-degenerate groundstate and V -representable electron densities $n(\mathbf{r})$, i. e., densities of the groundstate of the Hamiltonian (2.4) with a suitably chosen local external potential V^{ext} . Subsequently, the Hohenberg-Kohn theorem has been generalized to overcome these limitations [39].

The physical significance of the functional $F[n]$ becomes clearer when it is decomposed into the kinetic energy $T_s[n]$ of non-interacting electrons, the Hartree energy $E_H[n]$, and the *exchange-correlation* energy $E_{XC}[n]$,

$$F[n] = T_s[n] + \frac{e^2}{2} \int \int d\mathbf{r} d\mathbf{r}' \frac{n(\mathbf{r})n(\mathbf{r}')}{|\mathbf{r} - \mathbf{r}'|} + E_{XC}[n], \quad (2.6)$$

where the latter contains all quantum-mechanical contributions to the functional $F[n]$, notably the stabilizing electron-electron exchange energy as a consequence of the Pauli principle, the correlation energy as a result of correlated electron density fluctuations¹, and the difference between the true kinetic energy $T[n]$ and the kinetic energy of non-interacting electrons, $T_s[n]$. The exchange-correlation energy, however, is also unknown as a functional of the electron density, so one still needs physically sound approximations to make the density-functional theory work *in praxi*, see Sec. 2.1.4.

The second part of the Hohenberg-Kohn theorem allows for determining the ground-state energy of the many-particle system by means of variation of the total energy with respect to the electron density² under the condition of particle conservation $\int d\mathbf{r} n(\mathbf{r}) = \text{const}$:

$$\frac{\delta}{\delta n(\mathbf{r})} \left\{ E_{\text{tot}}[n] - \mu \int d\mathbf{r} n(\mathbf{r}) \right\} = \frac{\delta T_s[n]}{\delta n(\mathbf{r})} + V^{\text{ext}}(\{\mathbf{R}_k\}; \mathbf{r}) + V_H(\mathbf{r}) + \frac{\delta E_{XC}[n]}{\delta n(\mathbf{r})} - \mu \quad (2.7a)$$

$$= \frac{\delta T_s[n]}{\delta n(\mathbf{r})} + V_{\text{eff}}[n(\mathbf{r}); \mathbf{r}] - \mu. \quad (2.7b)$$

The Lagrange parameter μ is interpreted as the chemical potential of the electrons. In (2.7b) an effective potential has been defined where the functional derivative of the exchange-correlation energy is identified with the exchange-correlation potential $V_{XC}[n] = \delta E_{XC}[n]/\delta n(\mathbf{r})$. The interacting many-electron system can thus be formally mapped onto a fictitious system of non-interacting electrons under the influence of an effective potential V_{eff} with the Kohn-Sham Hamiltonian

$$\hat{H}_{\text{KS}} = \sum_i \left\{ -\frac{\hbar^2}{2m} \Delta_i + V_{\text{eff}}(\mathbf{r}_i) \right\}. \quad (2.8)$$

The structure of the above Hamilton operator suggests a product *ansatz* of single-particle orbitals φ_i for the many-particle wave function. The variation of the total energy with respect to these orbitals under the particle conservation constraint³ leads to the *Kohn-Sham equation*

$$\left\{ -\frac{\hbar^2}{2m} \Delta + V_{\text{eff}}[n(\mathbf{r}); \mathbf{r}] \right\} \varphi_i(\mathbf{r}) = \varepsilon_i \varphi_i(\mathbf{r}) \quad (2.9)$$

with the Kohn-Sham eigenvalues ε_i . They enter the Kohn-Sham equation as Lagrange multipliers during the variational procedure and are as such *a priori* void of physical significance. However, they exhibit in general the correct dispersion behavior in the

¹Formally the correlation energy can be defined as the difference between the exact electron-electron interaction energy due to the Coulomb repulsion and the Hartree-Fock exchange energy.

²For the simplicity of presentation we assume V -representable densities $n(\mathbf{r})$.

³Within the single-particle orbital ansatz this is equivalent to the demand of orthonormalization of the respective wave functions.

Brillouin zone and may be therefore be interpreted as bandstructure eigenvalues. The particular problems associated with the Kohn-Sham eigenvalues are briefly discussed in Sec. 2.1.5.

Although Eq. (2.9) is of the Schrödinger type, it can only be solved *self-consistently* because the effective potential V_{eff} functionally depends on the electron density

$$n(\mathbf{r}) = \sum_i |\varphi_i(\mathbf{r})|^2 \quad (2.10)$$

which, itself, depends on the solutions φ_i of the Kohn-Sham equation. But thanks to the Hohenberg-Kohn theorem unique solutions exist so that the self-consistency cycle is bound to terminate indeed at the electronic groundstate.

2.1.3 Total energy and Hellmann-Feynman forces

According to the Born-Oppenheimer approximation, see Sec. 2.1.1, the ionic and electronic degrees of freedom can be separated. Correspondingly, the total energy is decomposed into the energy of the ion-ion interaction and the electronic energy,

$$E_{\text{tot}} = E_{\text{ion-ion}} + E[n] = \frac{e^2}{2} \sum_{k \neq l} \frac{Z_k Z_l}{|\mathbf{R}_k - \mathbf{R}_l|} + E[n]. \quad (2.11)$$

The force on the k th atom is obtained by applying the gradient with respect to \mathbf{R}_k to the total energy,

$$\mathbf{F}_k = -\nabla_{\mathbf{R}_k} E_{\text{tot}} = \mathbf{F}_k^{\text{ion}} + \mathbf{F}_k^{\text{el}}. \quad (2.12)$$

The ionic contribution is solely determined by the ion-ion interaction, $\mathbf{F}_k^{\text{ion}} = -\nabla_{\mathbf{R}_k} E_{\text{ion-ion}}$, where the electronic part consists of the contributions from the external potential that is parametrically dependent on the atomic positions plus a so-called *variational force* that arises due to the implicit dependence of the electron density $n(\mathbf{r})$ on the atomic sites:

$$\mathbf{F}_k^{\text{el}} = - \int d\mathbf{r} n(\mathbf{r}) \nabla_{\mathbf{R}_k} V^{\text{ext}}(\{\mathbf{R}_k\}; \mathbf{r}) - \int d\mathbf{r} \frac{\delta E[n]}{\delta n(\mathbf{r})} \nabla_{\mathbf{R}_k} n(\mathbf{r}). \quad (2.13)$$

By construction, the second part vanishes in the electronic groundstate, so only the first part plus the ionic contribution, the so-called Hellmann-Feynman forces [40], are of physical origin. The vanishing of the Hellmann-Feynman forces, on the other hand, is the necessary condition for the structural equilibrium of the system.

2.1.4 Exchange-correlation functionals

For the practical implementation of the density-functional theory one must find suitable approximations for the exchange-correlation energy E_{XC} . For a long time the method of choice was the local-density approximation (LDA) [41] in which the exchange-correlation energy density $\epsilon_{\text{XC}}^{\text{hom}}$ of the homogeneous electron gas is evaluated at the actual electron density of the electronic system in question so that

$$E_{\text{XC}}[n] \approx \int d\mathbf{r} \epsilon_{\text{XC}}^{\text{hom}}(n(\mathbf{r})) \cdot n(\mathbf{r}). \quad (2.14)$$

By definition, the homogeneous electron gas has a spatially constant XC energy, so that, consequently, the exchange-correlation potential entering the Kohn-Sham Hamiltonian is given by

$$V_{\text{XC}} \approx \frac{d}{dn} \left[\epsilon_{\text{XC}}^{\text{hom}}(n) \cdot n \right]_{n=n(r)}. \quad (2.15)$$

The exchange-correlation energy of the homogeneous electron gas for different electron density regimes has been calculated by Ceperly and Alder [42] using Quantum Monte Carlo techniques, and Perdew and Zunger [43] developed a parametrization of the results. Although it may seem a crude approximation for inhomogeneous electronic systems, the LDA yields good results for, e. g., bond lengths and lattice constants, vibrational frequencies, and adsorption energies. Parts of this success are related to the facts that the LDA fulfills general sum-rules and that only a spherically averaged exchange-correlation density enters the expression for the XC energy. This success contributed strongly to the wide-spread use of density-functional theory methods and inspired a lot of work on better functionals, a field which is still very active today. One major disadvantage of the LDA, however, is the failure to predict accurate band gaps in semiconductors and insulators: it is consistently underestimated by factors between 50% and 100%. The reasons will be briefly discussed in Sec. 2.1.5.

The most common generalizations above the LDA are the generalized gradient approximations (GGA) which try to capture more of the inherently non-local exchange contributions in a local (or semi-local) functional. The idea to exploit informations from the density gradient goes back to Hohenberg and Kohn [38], but it turned out that a formal Taylor expansion of the exchange-correlation energy in terms of the density does not lead to a systematic improvement of the results because then scaling and limit properties of the exchange-correlation energy [44] are violated. Instead, the generalized gradient approximations start from the analytical behavior of the XC energy and interpolate suitably between the limiting cases. A versatile and highly transferable exchange-correlation energy functional is the PW91-functional [45,46] by Perdew and Wang.

2.1.5 The gap problem in density-functional theory

The Kohn-Sham gap is defined as the energy difference between the conduction band minimum and valence band maximum calculated within DFT in case of periodic crystals. For molecules the difference between the energies of the lowest unoccupied (LUMO) and the highest occupied molecular orbital (HOMO) is generally called HOMO-LUMO gap.

The underlying physical processes for the experimental determination of bandstructures are photoemission (PE) and inverse photoemission (IPE) for probing occupied and unoccupied states, respectively: an electron is either ejected from (PE) or injected to (IPE) a formerly occupied (PE) or unoccupied (IPE) state. In both cases the number of electrons changes by 1 with respect to the ground state, a process which changes the effective potential of the electronic system discontinuously.

The exchange-correlation potentials in either LDA or GGA, though, do not exhibit this discontinuity upon change of the number of electrons [39]. Therefore one cannot expect that the Kohn-Sham gap for semiconductors comes close to the experimental gap. The *dispersion* of occupied and unoccupied electronic states in the Brillouin zone, on the

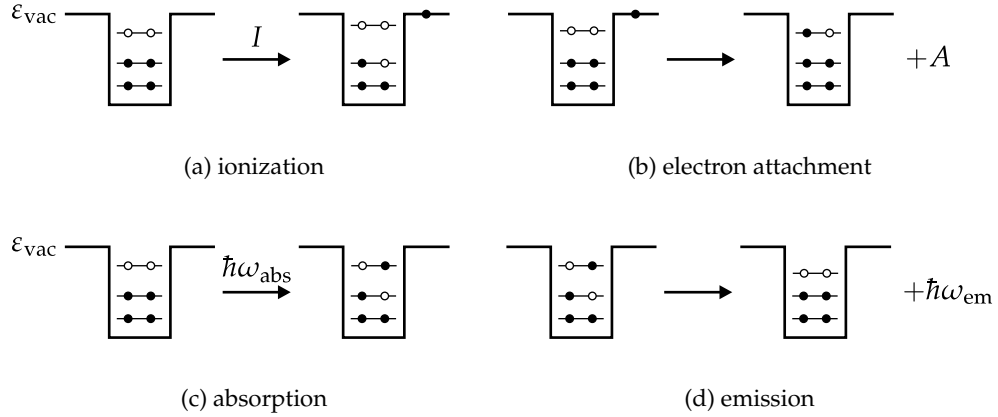


Figure 2.1: Schematic representation of the processes of (a) ionization, (b) electron attachment, (c) photon absorption, and (d) photon emission in a localized system. The vacuum level is denoted by ε_{vac} , occupied (unoccupied) electronic states are depicted as filled (empty) circles. The ionization energy I and the electron affinity A characterize charged excitations [(a) and (b)] in the system because the number of electrons changes where the neutral excitations [(c) and (d)] change the occupation of electronic levels while the number of electrons remains the same. Absorption and emission energies are indicated by $\hbar\omega_{\text{abs}}$ and $\hbar\omega_{\text{em}}$, respectively.

other hand, in general closely resembles the observed bandstructure because important contributions of the many-particle effects are covered within the DFT.

The systematic way to alleviate the gap problem and to take the excitation aspect into account is to start from Hedin’s fundamental system of coupled partial integro-differential equations [47] including all orders of electron-electron and electron-hole interaction to derive the *GW* and higher-order approximations [48]. This way will not be pursued here. Instead, where quantities like ionization energies and electron affinities are needed, we will resort to the so-called Delta-self-consistent field method sketched below.

2.1.6 Delta-self-consistent field method

The Delta-self-consistent field method (Δ SCF) aims at calculating physical quantities as a difference between two total energies arising from two fully self-consistent calculations for different systems. It is suited for systems where the charged excitations, e. g., ionization and electron attachment, or the neutral excitations, i. e., photon absorption, are sufficiently localized. This is generally the case for molecules and clusters with a diameter below approximately 10 \AA . A drastic exception in case of electron attachment to adenine will be shown and discussed in relation to the supercell approximation in Sec. 2.3.

The naïve approach to the calculation of the ionization energy I as a difference between the total energies of the $N - 1$ and N electron system, respectively,

$$I = E_{\text{tot}}(N - 1) - E_{\text{tot}}(N) \quad (2.16)$$

fails to recognize that the effective potentials and, hence, the vacuum levels $\varepsilon_{\text{vac}}(N)$ and $\varepsilon_{\text{vac}}(N - 1)$ of the N and $N - 1$ electron system are, in general, different. If ionization is understood as extracting one electron from a bound state and lifting it to the vacuum

level without transferring kinetic energy, see Fig. 2.1(a), then Eq. (2.16) must be expanded to

$$I = [E_{\text{tot}}(N-1) - \varepsilon_{\text{vac}}(N-1)] - [E_{\text{tot}}(N) - \varepsilon_{\text{vac}}(N)]. \quad (2.17)$$

In other words, the total energies of the N and $N-1$ electron system can only be compared if the different vacuum levels are aligned properly. The same holds in case of the electron affinity, see Fig. 2.1(b), which is given by

$$A = [E_{\text{tot}}(N) - \varepsilon_{\text{vac}}(N)] - [E_{\text{tot}}(N+1) - \varepsilon_{\text{vac}}(N+1)]. \quad (2.18)$$

One may then define a quasi-particle gap E_g^{QP} as the difference between the ionization energy and the electron affinity,

$$E_g^{\text{QP}} = I - A. \quad (2.19)$$

This quantity should agree better with the experimental gap energy because it includes interaction information from the wave functions of the $N \mp 1$ electron systems. If in addition the geometry in the excited states is allowed to relax one obtains from the resulting total energies the *adiabatic* ionization and electron affinities, respectively, instead of the vertical values from Eq. (2.17) and (2.18).

The ΔSCF approach can also be advantageously applied to approximately take into account the electron-hole interaction prominent in neutral pair excitations, see Fig. 2.1(c) and 2.1(d),

$$E_{\Delta\text{SCF}} = E_{\text{tot}}(N) - E_{\text{tot}}^{\text{e-h}}(N) \equiv \hbar\omega_{\text{abs}}, \quad (2.20)$$

where $E_{\text{tot}}^{\text{e-h}}(N)$ denotes the ground-state energy of the N electron system in the presence of an electron-hole pair. The transition to the excited state is mediated by, e. g., the absorption of a photon with a frequency ω_{abs} . If the transition occurs between the valence band maximum and conduction band minimum (or between HOMO and LUMO in case of molecules) the energy obtained from Eq. (2.20) is often called *optical gap* because it is, by definition, indicative of the onset of optical absorption in the system. A subsequent geometry optimization in the excited state corresponds physically to its non-radiative decay into a metastable state from which emission of a photon is possible with an energy $\hbar\omega_{\text{em}} \leq \hbar\omega_{\text{abs}}$, see Fig. 2.1(d). The difference $\Delta_{\text{Stokes}} = \hbar(\omega_{\text{abs}} - \omega_{\text{em}})$ between absorption and emission energy defines the Stokes shift. It should be noted that the optical gap usually does not coincide with the quasi-particle gap from Eq. (2.19) which plays a role in electron transport theory [49, 50] where it is consequently denoted *transport gap*.

Mind that all total energies entering Eq. (2.17), (2.18), and (2.20) are actually calculated for different systems: $E_{\text{tot}}(N)$ and $E_{\text{tot}}(N \mp 1)$ are the ground-state energies of an N and an $N \mp 1$ system in their respective ground-state occupation where $E_{\text{tot}}^{\text{e-h}}(N)$ corresponds to the ground-state energy of an N electron system with one electron excited from an occupied to an unoccupied orbital. These different systems are practically realized by applying an occupation constraint to the electronic states throughout the entire self-consistency cycle.

2.2 Implementation

There are a couple of possibilities for the practical implementation of the density-functional theory. Aspects to be considered are: the treatment of the external (ionic)

potentials (Sec. 2.2.1), the choice of the basis set for the expansion of the Kohn-Sham orbitals, and the method of discretizing the real space or reciprocal space domain of calculation (Sec. 2.2.2). The methods presented in the following are implemented in the *Vienna ab-initio simulation package* VASP developed by Kresse and Furthmüller [51] that is used throughout this thesis. It shows a very favorable scaling behavior with respect to the system size due to advanced and stable algorithms that keep the number of calls to cubically scaling parts of the code small. The latter, in fact, contribute to the overall execution time only with a small prefactor. The pseudopotentials that are shipped with VASP belong to the most transferable and well-tested potentials that are currently available. The code runs equally well on a number of diverse platforms ranging from PCs over workstation to massively parallel supercomputers or vector computers. More technical details and the consequences for practical calculations can be found in the original paper [51], the VASP manual [52] and a couple of proceedings of high-performance computing workshops [53–55].

2.2.1 Frozen core approximation and pseudopotentials

The electronic structure of an atom consists of core states and valence states. Due to the singular Coulomb potential contained in the ionic potential the core states are localized in the core region; thus, the valence states heavily oscillate in the core region because they must be orthogonal to the core state wave functions. These oscillations pose problems for the expansion of the valence states in most basis sets since the basis functions must be able to cover the qualitatively different characters of the wave functions in the core and interstitial regions.

Fortunately, the main contribution to the bonding arises from the valence wave functions outside the core region. Therefore, both the valence wave function and the ionic potential need to be treated exactly in this region only, whereas inside the core region they may be altered so that the oscillations vanish. The formal separation of the atom into a core that is independent of the environment and a valence region that determines the bonding properties has become known as the “frozen core approximation”. It is directly applicable for atoms with, energetically as well as spatially, well-separated, non-overlapping electronic states. For partially filled d levels in the transition metal elements or shallow d levels like, e. g., in Ga, this approach becomes questionable. Notwithstanding, the principal idea can be recovered by treating the outer core states as valence states.

The degree of freedom of altering the wave function in the core region allows for the construction of a pseudopotential that represents a pseudo atom which replaces the true atom by an effective core and a valence shell. The pseudopotential is constructed such as to describe the core electrons and their interaction as well as their influence on the valence electrons. The pseudopotential concept goes beyond the frozen-core approximation because it supposes, in addition to the *de facto* inertness of the core electrons, that the wave functions and charge densities of the valence electrons in the core region do not participate in the chemical bonding.

There are various approaches to the construction of pseudopotentials. These schemes have in common that they demand several conditions to be fulfilled which aim at recovering most of the physical and chemical properties of the true atom in the pseudo atom,

and, prominently, at improving the transferability of the pseudopotentials in different chemical and crystal environments. The so-called norm-conserving pseudopotentials go back to Hamann, Schlüter, and Chiang [56]. They rely on the DFT solution of the radial Schrödinger equation or, to include relativistic effects, the Dirac or Pauli equation for the single atom under four prerequisites: the eigenvalues of the true atom must equal those of the pseudo atom, the angular-moment dependent radial wave functions must coincide beyond a certain cutoff radius, the pseudo-charge inside the cutoff sphere must be identical to the true charge, and the energy derivative of the scattering phase must be the same for the true atom and the pseudo atom. The inversion of the radial Kohn-Sham equation leads to a pseudopotential that depends on the radial part of the pseudo wave function and as such on the angular momentum quantum number. It must consequently be described by a non-local operator. There are different practical schemes to the construction of these *ab initio* pseudopotentials because the pseudo wave functions may be altered with a substantial degree of freedom within in the cutoff sphere [57–59].

In this thesis we use generalizations over norm-conserving potentials like the ultrasoft pseudopotentials (US) [60] or pseudopotentials created within the so-called projector-augmented wave (PAW) scheme [61, 62] that are able to describe even first-row elements and atoms containing d electrons with a relatively low number of plane waves. In these two methods the demand of charge conservation inside the cutoff sphere is relaxed to obtain an additional degree of freedom that can be used to soften the pseudopotential [60], i. e., to increase the cutoff radius without losing accuracy. To ensure transferability the “wrong” pseudocharge must be corrected by so-called *depletion* charges (in case of the ultrasoft pseudopotentials) or *augmentation* charges (in case of the PAW pseudopotentials). Both corrections demand the introduction of a non-local overlap operator to account for these charges. This additional numerical complication is counterbalanced by a drastic reduction of the computational load. The methods differ mainly in the approach to the description of the pseudo wave functions inside the core-region. However, the US and PAW potentials are comparable with respect to the accuracy of the resulting properties and the numerical efficiency and are therefore used interchangeably in this thesis, US potentials in Chapters 3 and 6, PAW potentials in Chapters 4, 5, and 7.

2.2.2 Plane-wave expansion and Brillouin-zone integration

An expansion of the Kohn-Sham orbitals in a basis of plane waves in the space regions between the cores offers a couple of advantages. Notably, it is in the spirit of treating an infinitely extended crystal⁴ by employing a cell-based approach and Born-von-Kármán periodic boundary conditions: plane waves of the form $\chi_k(\mathbf{r}) \propto e^{i\mathbf{k}\mathbf{r}}$ with the wave vector \mathbf{k} trivially fulfill the Bloch theorem $\psi_k(\mathbf{r} + \mathbf{R}) = e^{i\mathbf{k}\mathbf{R}}\psi_k(\mathbf{r})$ for every lattice vector \mathbf{R} . Thanks to the periodicity the crystal can be described by considering one unit cell and the atomic basis which results in a drastic reduction of the computational effort. Further, if the Kohn-Sham orbitals are expanded in a Fourier series,

$$\phi_i(\mathbf{r}) \equiv \phi_{n\mathbf{k}}(\mathbf{r}) = \frac{1}{\sqrt{\Omega}} \sum_{\mathbf{G}} c_n(\mathbf{k} + \mathbf{G}) e^{i(\mathbf{k} + \mathbf{G})\mathbf{r}}, \quad (2.21)$$

⁴The infinite extent is a consequence of the demand for full translational symmetry.

with the sum over the reciprocal lattice vectors \mathbf{G} and the periodicity volume Ω , the electronic structure is completely characterized by the band index n and the wave vector \mathbf{k} restricted to the first Brillouin zone. Obviously, the wave functions defined above are periodic in reciprocal space.

Because of the completeness of a plane wave basis set the representation of the Kohn-Sham wave functions in the form Eq. (2.21) allows for an easy control of the convergence behavior by systematically increasing the number of Fourier coefficients \mathbf{G} . The so-called cutoff energy determines the maximum \mathbf{G} vector in the Fourier expansion by fixing the quantity $E_{\text{cut}} = \hbar^2 |\mathbf{G}_{\text{max}}|^2 / 2m$.

The disadvantages of using plane waves instead of, e. g., problem-adapted wave functions that come to mind quickly are the possibly large number of basis functions needed to obtain convergence for localized states and the uneasy feeling that plane waves themselves lack physical significance. Nevertheless, the convergence issue turns out to be rather uncritical in practical applications, and all physical quantities are derived from a well-defined wave packet as a superposition of suitably weighted exponentials.

Two points that go along with the interplay between the straightforward plane-wave expansion and the cell-based approach, on the other hand, demand closer attention. These are, first, the fact that the calculation of electric multipole moments becomes more complicated with periodic boundary conditions because the dipole moment is ill-defined [63]; second, for genuinely finite or isolated systems one must resort to the supercell approximation to effectively decouple the images of these systems that are present due to the artificially imprinted periodicity. These topics will be discussed in Sec. 2.3.

Upon inserting the wave function ansatz (2.21) into the Kohn-Sham equation a linear system of equations for the expansion coefficients c_n results with matrix elements of the effective potential. The necessary transformation of the latter to and from reciprocal space can be efficiently implemented using the Fast Fourier Transform (FFT). This is advantageous because the exchange-correlation potential is usually calculated in real space with the real-space charge density.

Numerically, the Brillouin-zone integrations are carried out as summations over a discrete mesh of \mathbf{k} points. The systematic approach to the construction of \mathbf{k} -point sets by Monkhorst and Pack [64] yields \mathbf{k} points that respect the space group symmetry of the system in question. By reduction to the irreducible part of the Brillouin zone the convergence of the total energy can be usually obtained with a low number of special points, even for small real-space unit cells. What holds for the total energy need not necessarily still be true for derived quantities like the frequency-dependent dielectric tensor: experience has shown that the optical properties are in critical cases better described when using random \mathbf{k} points for the Brillouin-zone summations [65]. The reason for this, at first glance, peculiar finding is that the Monkhorst-Pack scheme, by construction, creates symmetry-respecting \mathbf{k} points at which the optical transition matrix elements are calculated so that the oscillator strengths at intermediate points are neglected although these may contribute substantially to the optical spectrum.

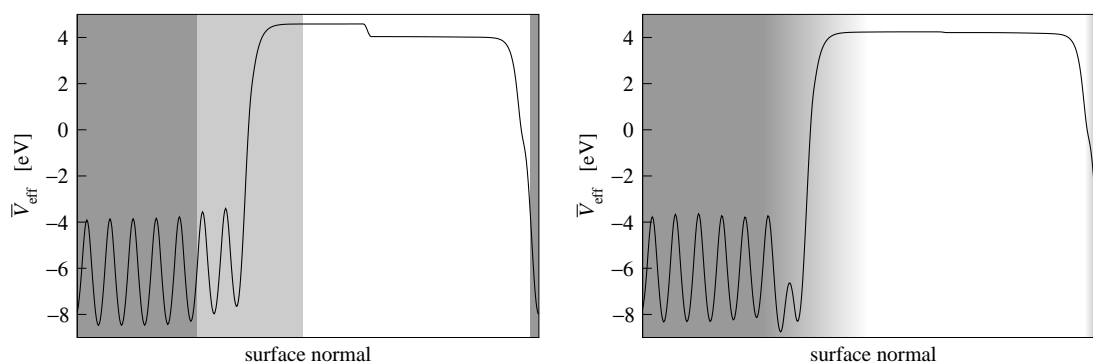


Figure 2.2: Laterally averaged effective Kohn-Sham potential \bar{V}_{eff} along the surface normal of an eight-layer hydrogen-terminated Si(001) slab. The length of the supercell amounts to 27.35 Å. Even in case of ideal bulk termination (left) a sharp distinction between bulk (dark gray), surface (light gray), and vacuum (white) regions is artificial. After relaxation and dimerization a 2×1 reconstruction results which leads to substantial changes to the potential (right) that give rise to pronounced surface states. The jump of the potential in the vacuum region is due to the electronic inequivalency of the two sides of the slab.

2.3 Supercell approach

2.3.1 Repeated slabs

While an ideal, infinitely extended bulk crystal is, by definition, periodic in all three space dimensions⁵, this full translational symmetry is broken upon creation of a surface. This perturbation in general goes along with drastic, intertwined changes to the geometric and electronic structure of the truncated bulk system. In case of metals one usually observes *relaxation* of the first couple of surface layers because at the abrupt interface the charge density is smeared out into the vacuum region. In case of semiconductors, in addition to the relaxation, frequently a *reconstruction* takes place that is connected with a change of the two-dimensional surface periodicity. The often complicated rearrangements and rebondings of the surface and sub-surface atoms are mainly driven by the tendency towards minimization of the number of *dangling bonds* that are created at the surface upon bulk truncation, and compensation of surface charges [66].

Irrespective of the approach to the description of crystals one is confronted with the problem of accurately treating the bulk–surface–vacuum interface. A method suitable for relatively simple model systems consists of augmenting the entire set of Bloch states by evanescent waves and matching the extended basis to solutions of the Schrödinger equation in the surface region [67,68]. The definition of the latter constitutes the uncertainties inherent to this approach because the delimitation between bulk and surface regions is not a sharp one, see Fig. 2.2. Moreover, numerical instabilities have hampered a widespread application to real-life systems.

To circumvent these difficulties an artificial translational symmetry is introduced by using unit cells with a large extent in direction of the surface normal [69]. This so-called “supercell” contains a slab of the material in question of finite thickness which must, firstly, be large enough to effectively decouple the electronic surface states on both sides

⁵This definition can also be read *vice versa*, see the corresponding footnote on page 14.

of the slab. Secondly, the electrostatic potential must reach a plateau in the vacuum region so that the corresponding value can be used as a reference for the calculation of, e. g., ionization energies as outlined in Sec. 2.1.6. Furthermore, it is used for the energy level alignment in interface systems consisting of different materials to derive band offsets [70]. The requirement of a flat vacuum level may lead to very large slabs which make the practical calculations very demanding. The dipole corrections introduced in the next Section improve the convergence of the vacuum level to a constant value with respect to the dimension of the supercell dramatically so that the calculations become feasible. If polar surfaces⁶ are treated, thirdly, one has to ensure that there is no charge transfer between both sides of the slab. Shiraishi [71] suggested to passivate one side of the slab with hydrogen or pseudo-hydrogen with variable valence in dependence of the coordination number of the surface atoms. The electronic states resulting from these bondings generally lie far below the Fermi energy of the system so that their influence on the properties of the unpassivated surface side is negligible. However, the slab sides become electronically inequivalent which leads to the formation of a small dipole potential in the supercell, see Fig. 2.2. Methods to correct for this additional potential are introduced in the next section.

The statements above apply, by obvious generalizations, also for the treatment of isolated molecules. The three-dimensional periodicity enforced by the supercell approach means that actually a diluted gas of molecules is calculated; to extract single-molecule properties the supercell must be large enough to prevent electrostatic interactions between the molecules in adjacent cells. The dipole corrections that were initially developed for surface slabs can be used advantageously to achieve this aim and at the same time limit the extent of the vacuum region to a manageable size.

2.3.2 Monopole and dipole corrections

The problems arising from the supercell approach to the calculation of surface or molecular properties outlined above can be consistently solved by accounting for an *additional* electrostatic potential in the Kohn-Sham Hamiltonian. Such a potential serves several purposes: it may be used to improve the numerical efficiency of supercell calculations by limiting the sizes of the slab and vacuum regions, it allows for an accurate physical description of polar surfaces, it enables direct access to electronic dipole moments which, in turn, are important ingredients for the determination of vibrational surface spectra, and, last, but not least, it may be employed to model the influence of an externally applied macroscopic electric field on the molecular or surface system.

The approach to the correction of the spurious contributions from an artificial dipole or, as a matter of fact, to the determination of a truly physical dipole, is most readily understood in case of a surface system described within a repeated-slab geometry. Let A denote the surface area and c the length of the supercell in direction of the surface normal. The laterally averaged electronic charge density \bar{q}_{el} shall assume its minimum at

⁶In the strict sense, a surface derived from an ionic crystal is polar if the ion termination is different on the two sides of the slab. Examples are GaAs(001) and SiC(0001) surfaces.

a position z_0 in the vacuum region in the slab. Due to the finite size of the slab there is, in general, a non-vanishing dipole moment μ per surface area,

$$\mu = \int_{z_0}^{z_0+c} dz z [\bar{\rho}_{\text{el}}(z) + \bar{\rho}_{\text{ion}}(z)], \quad (2.22)$$

where $\bar{\rho}_{\text{ion}}$ denotes the laterally averaged ionic charge density. This dipole moment is compensated for by a dipole layer parallel to the surface placed at z_0 which corresponds to the electrostatic potential

$$V_{\text{el}}(z) = -\frac{4\pi\mu}{V_{\text{cell}}} [z - c \cdot \Theta(z_0 - z)] \quad (2.23)$$

where V_{cell} is the cell volume. z is restricted to lie between 0 and c so that V_{el} is a saw-tooth potential because of the periodic boundary conditions. The electric field $\mathcal{E} = \mu/(4\pi V_{\text{cell}})$ is aligned along the z -axis of the cell. The change in the total energy due to the presence of the additional external potential (2.23) is given by

$$\Delta E = \int dz [\bar{\rho}_{\text{el}}(z) + \bar{\rho}_{\text{ion}}(z)] V_{\text{el}}(z) = -\mu\mathcal{E} \quad (2.24)$$

which is the classical interaction energy of a dipole μ with an electric field \mathcal{E} . Equations (2.22)–(2.24) constitute the basics of the dipole corrections implemented in modern density-functional theory codes. As the derivation is quite general, they are also suited for the determination of genuine permanent electric dipole moments of molecules and clusters by obvious generalizations to the other components of the dipole. In this case it is crucial to carefully choose the point of reference with respect to which the dipole moment is calculated. This is especially critical if this point does not fall into the vacuum region because the dipole moment itself then loses its physical significance. Nonetheless, differences between such dipole moments may still be used to derive information about the dynamical properties of the vibrating lattice, see Sec. 2.4.

For charged systems the total energy converges very slowly with respect to the dimensions of the unit cell. Therefore in practical implementations a neutralizing background is included in the calculations. This procedure is also known as monopole correction, in analogy to the dipole corrections. It allows for determining, e. g., ionization energies and electron affinities of molecules according to the Δ SCF method outlined in Sec. 2.1.6 (page 11) within an accuracy of about 0.1 eV. The Δ SCF approach, though, requires a sufficient localization of the states that are affected by these charged excitations. While this prerequisite is usually fulfilled in case of ionization, i. e., for the HOMO state, the injection of an additional electron into the LUMO can lead to a delocalized electronic state with an energy above or too close to the vacuum level where the correct description of its character may be hampered by the supercell approximation. A very drastic example is shown in Fig. 2.3 for the adenine molecule: the singly occupied electronic state after the electron attachment lies energetically below the vacuum level and is as such a bound state. As it exhibits substantial probability density in the corners of the supercell the dipole corrections fail to work, and one cannot expect to obtain a reliable result for the electron affinity of adenine. Indeed, in the $20 \text{ \AA} \times 20 \text{ \AA} \times 10 \text{ \AA}$ cell the adenine anion turns out to be unstable. Louie [72] hinted at a workaround for these kinds of problems: a delocalized

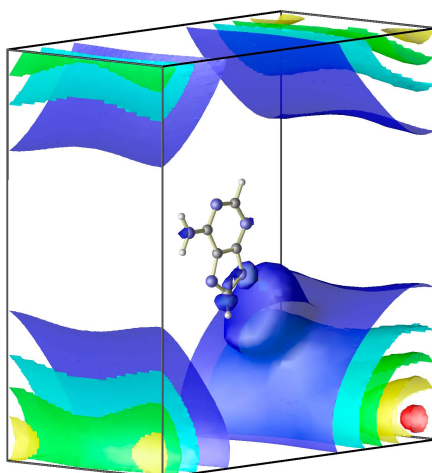


Figure 2.3: Isosurfaces of the square modulus of the wave function corresponding to the singly-occupied state after electron attachment to adenine with values varying linearly between $0.5 \cdot 10^{-3} \text{ e}/\text{\AA}^3$ (blue) and $4.5 \cdot 10^{-3} \text{ e}/\text{\AA}^3$ (red). Blue (gray, white) spheres depict nitrogen (carbon, hydrogen) atoms. The supercell with dimensions $20 \text{ \AA} \times 20 \text{ \AA} \times 10 \text{ \AA}$ is indicated.

bound state tends to localize in the supercell if the Brillouin-zone integrations are carried out with more than one k point although the dispersion of the state is seemingly negligible. Moreover, adenine is a special case because there are experimental indications that the additional electron occupies a Rydberg state the center of which is found about 10 \AA away from the molecular frame [73]. So the supercell would have to be much larger in order to correctly describe this spatially separated state.

2.3.3 Symmetry and modeling

The notion of symmetry plays a major role in diverse areas of the natural sciences because in general every physical or, for that matter, chemical or biological system possesses certain symmetries that determine and influence the system's properties. The theory of finite groups provides the mathematical methods to describe and quantitatively exploit the symmetries by classifying the possible states of a system according to the irreducible representations of its point or space group⁷. In this thesis the historically grown Schönflies terminology will be used to denote point groups because, to the author's mind, it captures the geometric content of point group symmetries in a more intuitive way than the international Hermann-Mauguin notation. In Table 2.1 the two notations are juxtaposed for the 32 point groups that are possible in three-dimensional crystals.

An n -fold rotation axis C_n lends its name directly to the corresponding point group. The same holds for the mirror-rotation axis S_{2n} where n is the order of rotation. Note that a five-fold rotation is not possible in crystals; no such restrictions, of course, exist for free molecules. If there is only a single symmetry plane in the system, the respective point group is denoted by C_s or equivalently by C_{1h} . If no rotational axis and no symmetry

⁷The space group can be understood as the union of a point group and a translational group plus fractional translations. Generally speaking, the set of symmetry elements under which equivalent atomic positions are invariant is called space group.

Table 2.1: Symmetry notations (H-M: Hermann-Mauguin, Sf: Schönflies) for the 32 possible point groups or classes in three-dimensional crystals (after [74]) together with the classification into the seven crystal systems.

System	Class	H-M	Sf	System	Class	H-M	Sf
triclinic	1	1	C_1	trigonal	16	3	C_3
	2	$\bar{1}$	C_i		17	$\bar{3}$	S_6
monoclinic	3	m	C_s		18	$3m$	C_{3v}
	4	2	C_2	19	32	D_3	
	5	$2/m$	C_{2h}	20	$\bar{3}m$	D_{3d}	
orthorhombic	6	mm	C_{2v}	hexagonal	21	6	C_6
	7	222	D_2		22	$\bar{6}$	C_{3h}
	8	mmm	D_{2h}		23	$6/m$	C_{6h}
	tetragonal	9	4		C_4	24	$\bar{6}m2$
10		$\bar{4}$	S_4		25	$6mm$	C_{6v}
11		$4/m$	C_{4h}	26	622	D_6	
cubic	12	$4mm$	C_{4v}	27	$6/mmm$	D_{6h}	
	13	$\bar{4}2m$	D_{2d}	28	23	T	
	14	422	D_4	29	$m\bar{3}$	T_h	
	15	$4/mmm$	D_{4h}	30	432	T_d	
	31	432	O	31	432	O	
				32	$m\bar{3}m$	O_h	

plane are present, there may be only a center of symmetry, denoted by i , or no symmetry element besides the identity operation E , corresponding to the point group C_1 . Mirror planes are labeled by σ , the most important are vertical mirror planes that contain the rotation axis (σ_v) and horizontal mirror planes that are perpendicular to the rotation axis (σ_h). The indices v and h at the group symbols indicate the presence of such mirror planes in the corresponding system. An additional mirror plane that does not coincide with either σ_v or σ_h is generally denoted by σ_d and, correspondingly, the index d attached to the group name. The D_n point groups are characterized by the existence of n additional two-fold rotation axes perpendicular to the C_n axes. Each of the cubic point groups T , T_h , T_d , O , and O_h has four three-fold rotation axes. The symmetry elements in Hermann-Mauguin notation are the identity 1, the inversion $\bar{1}$, the n -fold rotation axis n , the n -fold mirror-rotation axis \bar{n} , the mirror plane m , and the n -fold rotation axis with a mirror plane perpendicular to it, n/m .

There is an intimate connection between the geometrical symmetry of system and its wave function due to the Wigner-Eckart theorem [75]: the eigenfunctions of the system can be classified according to the irreducible representations of the point group of the system. In other words, the eigenfunctions transform according to these representations. Therefore it is of utmost importance that the symmetry of the system is determined correctly. Otherwise all properties derived from the eigenfunctions are incorrect. While this is of minor significance for integrated properties like the total energy, it becomes critical when, e. g., individual matrix elements of certain operators between the eigenfunctions are involved. If symmetry-induced degeneracies of electronic states are

erroneously lifted, transitions may become allowed that are in fact forbidden due to the symmetry selection rules.

The point group of the crystal is determined by the supercell arrangement and the atomic basis. It is therefore, in general, a subgroup of the point group of the isolated molecule. During the work on the present thesis it has been observed that in some cases the description of isolated molecules within the supercell approach poses problems with regard to the determination of the correct molecular symmetry. The examples given concern the molecules ammonia (NH_3) and benzene (C_6H_6). The problems, consequences, and remedies are discussed in the following.

Ammonia

If the ammonia molecule is aligned in a cubic supercell in such a way that the nitrogen lone pair orbital points in a direction parallel to one of the unit cell axes (inset on the left part of Fig. 2.4), the three-fold rotational symmetry of the molecule is not recovered by the *ab initio* code. The geometry optimization finishes with one hydrogen atom 0.1 \AA (0.05 \AA) off the plane of the other two hydrogen atoms if treated in a $10 \text{ \AA} \times 10 \text{ \AA} \times 10 \text{ \AA}$ ($20 \text{ \AA} \times 20 \text{ \AA} \times 20 \text{ \AA}$) supercell, corresponding to a $C_{1h} \equiv C_s$ symmetry. We thus find a strong finite-size effect as an artifact of the supercell approximation that directly affects the geometry *and* the symmetry. While the *quantitative* amount of the error can be reduced by increasing the size of the supercell and/or applying dipole corrections, the *qualitative* error cannot be eliminated in such a way; the symmetry keeps being determined incorrectly. One consequence is illustrated in Fig. 2.4: the reduced supercell symmetry leads to an infrared spectrum with an additional peak (left) that is not present if the correct C_{3v} symmetry (right) is used to calculate the corresponding dynamical dipoles (see next Section for details of the computational procedure). Fortunately, the problem can be circumvented here easily by an arrangement of the molecule in the cell in such a way that the three N-H bonds and, for that matter, the nitrogen lone-pair axis, are aligned parallel to the corner-to-corner diagonals of the cube. Then the *ab initio* code identifies the correct C_{3v} symmetry, irrespective of the size of the supercell, provided it is large enough to prevent molecule-molecule interactions between adjacent cells. The reason for this, at first

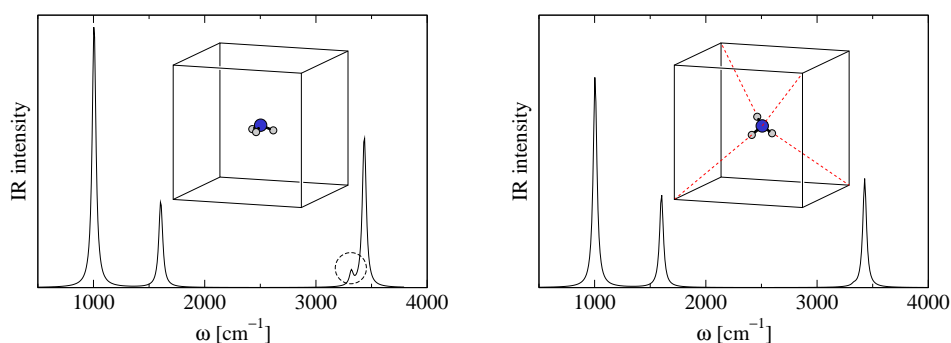


Figure 2.4: Calculated infrared spectra of ammonia. Left: The arrangement of the molecule in the supercell as sketched in the inset yields a wrong $C_{1h} \equiv C_s$ symmetry which leads to the appearance of an additional absorption peak, indicated by the dashed circle. Right: The additional peak disappears if the molecule is arranged such as to yield the correct C_{3v} symmetry.

sight, peculiar behavior is that in this way the point group of the crystal is the same as the point group of the free molecule because the vertical mirror planes contain one of the C_3 axes of the cube which coincides with the rotational axis of the molecule.

Benzene

Benzene (C_6H_6) represents the prototypical aromatic molecule that exhibits a delocalized π -electron system. The six carbon-carbon bonds are of the same length (1.398 Å) in the mesomeric limiting state which is the ground state of benzene. The molecule is planar, and, consequently, the molecular point group of benzene is D_{6h} . However, if the molecule is described in a cubic $20 \text{ \AA} \times 20 \text{ \AA} \times 20 \text{ \AA}$ cell with the molecular plane parallel to one of the faces of the supercell, the geometry analysis routine of the employed *ab initio* code VASP determines only the much lower crystal point group D_{2h} ; even after the geometry optimization the correct point group is not recovered although the carbon-carbon bond lengths turn out to be equal with deviations of less than 10^{-3} \AA . The left panel of Fig. 2.5 shows the direct consequences for the electronic structure: the highest occupied molecular orbital lacks the six-fold rotational symmetry demanded by the true D_{6h} point group (right panel). Because of the very different selection rules for dipole or quadrupole matrix elements of the groups D_{2h} and D_{6h} this immediately affects the allowed transitions in absorption spectra in all spectral regions.

As in the case of ammonia, the problem can be solved by the choice of an adapted supercell. If the benzene molecule is arranged in a hexagonal cell in such a way that two carbon-carbon bonds are parallel to the lateral basis vectors, the correct D_{6h} symmetry is indeed determined because then the generators of the point group of the molecule and of the associated full space group of the crystal are the same. Consequently, the highest occupied molecular orbital is invariant under the action of the D_{6h} group elements (right panel of Fig. 2.5).

It should be noted that the determination of reduced point group symmetries is not due to an actual error in the *ab initio* code. The symmetry routine developed by J. Furthmüller was initially intended for the analysis of crystalline systems like bulk materials or slabs where the user's freedom of choosing a supercell is rather limited. Moreover, in the spirit of treating infinite solids within periodic boundary conditions, the symmetry analysis is restricted to find one of the 32 point groups possible in translationally invari-

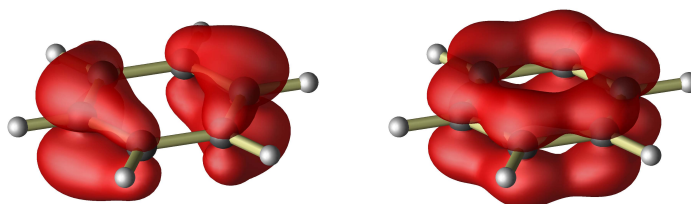


Figure 2.5: Isosurfaces of the charge density associated with the wave function of the highest occupied molecular orbital (HOMO) of benzene. In the molecule dark gray (light gray) spheres depict carbon (hydrogen) atoms. Left: 0.05 e/\AA^3 -isosurface of the HOMO with apparent D_{2h} symmetry, right: 0.05 e/\AA^3 -isosurface of the HOMO with D_{6h} symmetry.

ant solid state bodies. For example, the $C_{\infty v}$ symmetry of the carbon monoxide molecule CO cannot be recovered in this framework, irrespective of the choice of the supercell.

Summarizing, it is worthwhile to spend enough time on the modeling of the system in question in order to obtain the correct symmetry. This additional effort may not only save valuable computational resources, but, even more importantly, prevents the occurrence of unexpected and seemingly unexplainable results. This statement of course not only holds for molecules, but for bulk and surface systems as well.

2.4 Adsorbate and substrate vibrations

A system with atoms in equilibrium positions responds to geometrical distortions with resulting forces which can be easily calculated by the Hellmann-Feynman theorem [76] as derivatives of the total energy with respect to (Cartesian) atomic coordinates, see Sec. 2.1.3. The linearization of these forces in the atomic displacements generates a $3N \times 3N$ -matrix (N : number of atoms) called the Hessian or dynamical matrix of the system constructed as follows. Let $F_{\alpha\beta}^{\mu\nu,\pm}$ denote the ν -th Cartesian component of the resulting force on atom β due to a displacement of the α -th atom in the positive (+) or negative (−) Cartesian direction μ . These forces build up the matrix ($K_{\alpha\beta}^{\mu\nu}$)

$$K_{\alpha\beta}^{\mu\nu} = \frac{1}{2} \frac{F_{\alpha\beta}^{\mu\nu,+} - F_{\alpha\beta}^{\mu\nu,-} + F_{\beta\alpha}^{\nu\mu,+} - F_{\beta\alpha}^{\nu\mu,-}}{2d} \quad (2.25)$$

which is symmetric with respect to a simultaneous change of α, β and μ, ν . The displacement d is to be chosen small enough to ensure harmonicity of the vibrations on the one hand and large enough to avoid numerical problems on the other hand. Empirically, values between 0.02 Å and 0.05 Å turn out to be well suited. In the end, of course, the result must be independent of the choice of d . The Hessian is defined as the quadratic matrix H with

$$H_{ij} \equiv H_{3(\alpha-1)+\mu, 3(\beta-1)+\nu} = K_{\alpha\beta}^{\mu\nu}. \quad (2.26)$$

Obviously, as $1 \leq \alpha, \beta \leq N$ and $1 \leq \mu, \nu \leq 3$, the indices of the Hessian cover the range $1 \leq i, j \leq 3N$. The generalized Newtonian equations of motion thus read

$$M\ddot{u} = -Hu \quad (2.27)$$

with the matrix M of atomic masses,

$$M = \text{diag}(m_1 1_3, m_2 1_3, \dots, m_N 1_3), \quad 1_3 = \text{diag}(1, 1, 1), \quad (2.28)$$

and the displacement vector

$$u = (u_1, u_2, \dots, u_{3N})^\top. \quad (2.29)$$

If a harmonic time-dependence of the displacement vectors ($u = ze^{i\omega t}$) is assumed, the equations of motion reduce to the generalized eigenvalue problem

$$Hz = \omega^2 Mz. \quad (2.30)$$

The resulting eigenvectors $z^{(i)}$, $i = 1, \dots, 3N$, are M -orthogonal. This means the matrix $Z = (z^{(1)}, \dots, z^{(3N)})$ of eigenvectors satisfies $Z^\top MZ = 1$, therefore the scaled vectors

$q^{(i)} = M^{1/2}z^{(i)}$ are mutually orthogonal. By derivation, they diagonalize the kinetic energy T and the potential energy V of the vibrating system, respectively,

$$T = \frac{1}{2} \sum_{i=1}^{3N} (\dot{q}^{(i)})^2, \quad V = \frac{1}{2} \sum_{i=1}^{3N} \omega_i^2 (q^{(i)})^2, \quad (2.31)$$

where ω_i is the eigenvalue belonging to the eigenvector $q^{(i)}$. To comply with the standard notation in chemical literature, a dimensionless so-called normal-mode coordinate q_i is introduced as an ‘‘amplitude’’ of the normalized eigenvector $q^{(i)}$. Derivatives of physical quantities A with respect to q_i are understood as infinitesimal changes A in direction of the respective eigenvector so that one defines such normal-mode derivatives as

$$\frac{\partial A}{\partial q_i} \equiv \frac{\partial A}{\partial x} \cdot q^{(i)} = \sum_{\alpha=1}^N \sum_{\tau=1}^3 \frac{\partial A}{\partial x_{\tau}} q_{3(\alpha-1)+\tau}^{(i)}, \quad i = 1, \dots, 3N, \quad (2.32)$$

where $\partial A/\partial x$ denotes the $3N$ -dimensional gradient of A with respect to Cartesian coordinates. The scalar product on the right-hand side of Eq. (2.32) is written in a way to indicate separately atoms, enumerated by α , and the vector components belonging to an atom, enumerated by τ . A central quantity derived from the changes of the system’s dipole moment μ with respect to the Cartesian coordinates of the α -th atom is the *atomic polar tensor* $A^{(\alpha)}$ (APT), defined by its matrix elements as

$$A_{\nu\tau}^{(\alpha)} \equiv \frac{\partial \mu_{\nu}^{(\alpha)}}{\partial x_{\tau}}, \quad \nu, \tau = 1, 2, 3. \quad (2.33)$$

The intensity of the i th normal mode in an infrared spectrum is given by [77]

$$I_i \propto \left| \frac{\partial \mu}{\partial q_i} \right|^2, \quad (2.34)$$

where we suppress any prefactors that depend on the measurement conditions because we are mainly interested in relative intensities. By combining Eqs. (2.32) and (2.33) the relation between changes of the system’s total dipole moment along the i th normal mode and the atomic polar tensors is established as

$$\frac{\partial \mu_{\nu}}{\partial q_i} = \sum_{\alpha=1}^N \sum_{\tau=1}^3 \frac{\partial \mu_{\nu}^{(\alpha)}}{\partial x_{\tau}} q_{3(\alpha-1)+\tau}^{(i)} \quad (2.35a)$$

$$= \sum_{\alpha=1}^N \sum_{\tau=1}^3 A_{\nu\tau}^{(\alpha)} q_{3(\alpha-1)+\tau}^{(i)}, \quad \nu = 1, 2, 3. \quad (2.35b)$$

The numerical implementation with a finite-difference approach to the calculation of changes of the dipole moment is done using a central-difference scheme,

$$\frac{\partial \mu_{\nu}^{(\alpha)}}{\partial x_{\tau}} = \frac{\mu_{\nu}(x_{\tau}^{(\alpha)} + d) - \mu_{\nu}(x_{\tau}^{(\alpha)} - d)}{2d}, \quad (2.36)$$

where $\mu_{\nu}^{(\alpha)}$, as in Eq. (2.33), indicates the ν -th component of the total dipole of the system that results from the displacement of the α -th atom in the τ -th Cartesian direction.

There are three technical points to address. Firstly, the construction of the full Hessian for N atoms within the central-difference scheme requires $2 \times 3N = 6N$ fully self-consistent calculations if no symmetry arguments help to reduce the computational cost. The demand in computing time can thus be high, depending on the system size. However, because the distortions from the equilibrium geometry are small, the electronic self-consistency cycle usually finishes after a few steps if it starts with the already converged electronic wave functions of the equilibrium configuration. As Eq. (2.36) is structurally the same as Eq. (2.25) the elements of the Hessian and the dipole moment can be calculated accompanyingly. Secondly, especially in slab geometry, the number N of atoms chosen to include in the calculation determines to some extent the attainable range of the vibrational spectrum. If the adsorption of molecules on surfaces is studied then the high-frequency region will be dominated by the adsorbate vibrations whereas the low-frequency part, say, below 300 cm^{-1} , is mostly the domain of lattice vibrations of the substrate. If deeper-lying substrate atoms have to be included in the calculation, one will fall in the range of phonons where the validity of the above-mentioned method of calculation of intensities becomes questionable. The lattice dynamics is then more appropriately treated in the closely related so-called *ab initio* force constant method [78] or the density-functional perturbation theory [79] which yields full phonon dispersion curves.

Thirdly, in the case of vibrations of adsorbates at surfaces the *absolute* values of the calculated in-plane dipole moment components are less useful due to the periodic boundary conditions. Nevertheless, when related to a common point of reference, our test calculations have shown that the respective *changes* of these values can be used for the calculation of vibrational intensities in the same way as in the case for isolated molecules.

2.5 Technical parameters of the calculations

All total-energy and electronic-structure calculations presented here are performed using the gradient-corrected (PW91) [46] density-functional theory (DFT) as implemented in the Vienna Ab-initio Simulation Package (VASP) [51]. Although PW91, as well as other gradient approximations [80], does intrinsically not account for dispersion interactions it has been successfully applied to physisorbed geometries [81]. However, in Ref. [82] the failure of GGA has been demonstrated in the case of graphite where the interlayer bonding is exclusively mediated by van-der-Waals contributions. Therefore the results where physisorption prevails must be interpreted with due caution.

The electron-ion interaction is described by ultrasoft pseudopotential in Chapters 3 and 6 and within the projector-augmented wave scheme in Chapters 4, 5, and 7. In all cases treated in this thesis it turned out that due to the softness of the pseudopotentials an expansion into plane waves up to an energy cutoff of 25 Ry is sufficient to obtain numerically converged results for the total energy and derived properties, even for adsorbate systems containing first-row elements.

The total energy is consistently minimized using the *residual minimization method – direct inversion in the iterative subspace* (RMM-DIIS) algorithm [83, 84]. The molecular and surface atomic structures are considered to be in equilibrium when the Hellmann-Feynman forces are smaller than $10 \text{ meV}/\text{\AA}$.

Throughout the thesis the free and adsorbed surfaces are described using the repeated-slab method, see Sec. 2.3. The Si(001) surface is modeled with a periodically repeated slab where the supercell consists of 8 atomic layers and a vacuum region equivalent in thickness to 12 atomic layers. The Si bottom layer is hydrogen-saturated and kept frozen during the structure optimization while all other degrees of freedom are allowed to relax. All calculations are done using the theoretical Si equilibrium lattice constant of 5.456 Å (US potentials) or 5.470 Å (PAW potentials). The relative deviation of the lattice constants due to the usage of different pseudopotentials amount to less than 0.3% and does not influence the reliability of the results as long as both substrate and adsorbate are consistently described by the same type of pseudopotentials. The integrations in reciprocal space for the Si(001) systems are performed with Monkhorst-Pack points corresponding to four (two, one) k point(s) in the irreducible part of the Brillouin zone for the nominal $c(4 \times 2)$ and 2×1 (2×6 and 6×2 , 4×4) surface periodicities.

The SiC surfaces are described in a supercell with a slab thickness of six Si-C bilayers and a vacuum region corresponding to 12 bilayers. Cubic stacking has been assumed along the (111) direction in each slab. Our previous calculations have shown that the actual stacking and, hence, the polytype of the substrate, is of minor influence on the geometry and energetics of the surface layers [85,86]. Analogously to the case of Si(001), the slab bottom layer is hydrogen-saturated and kept fixed. The calculated SiC equilibrium lattice constant of 4.387 Å is used throughout the computations. The Brillouin-zone integrations are carried out with four (eight) k points in its irreducible part in case of the 3×3 ($\sqrt{3} \times \sqrt{3}$) reconstructions.

The supercell for the Cu(110) surface plus one adenine molecule consists of a six-layer copper slab and a vacuum region that equivalently amounts to 44 atomic layers. The large extent of the supercell in normal direction of about 25 Å is necessary to get rid of unwanted interactions between the molecule and the bottom layer of the Cu(110) surface during the constrained-dynamics calculations in which the molecule is successively brought farther away from the surface. All calculations are performed at the theoretical lattice constant of 3.6368 Å using a $p(3 \times 4)$ surface periodicity to prevent molecule-molecule interactions between neighboring supercells. The lattice constant corresponds to the spacing of neighboring copper rows so that the intrarow spacing of adjacent copper atoms is $3.6368 \text{ Å} / \sqrt{2} = 2.5716 \text{ Å}$. The uppermost two copper layers as well as the molecular overlayer are free to relax. The Brillouin zone integrations are restricted to the Γ point.

In accordance with the diffraction results from Ref. 30 the adenine rows on the Cu(110) surface are described in a surface unit cell spanned by the lattice vectors $\mathbf{a} = \mathbf{a}_{1 \times 1} + 2\mathbf{b}_{1 \times 1}$ and $\mathbf{b} = 6\mathbf{a}_{1 \times 1}$ with the surface lattice vectors of the Cu(110) 1×1 unit cell, $\mathbf{a}_{1 \times 1} = d(1, 0, 0)$ and $\mathbf{b}_{1 \times 1} = d(0, \sqrt{2}, 0)$ where $d = 2.5716 \text{ Å}$ corresponds to the intrarow copper-atom spacing in the $[1\bar{1}0]$ direction. In conventional matrix notation the unit cell is characterized by the matrix $\begin{pmatrix} 1 & 2 \\ 6 & 0 \end{pmatrix}$. The vector \mathbf{a} encloses an angle of 70.53° with the copper row axis. The unit cell consists of four layers of copper plus molecular overlayer. As above the length of the supercell along the surface normal amounts to about 25 Å to prevent interactions of the adenine molecules with the bottom layer of the Cu slab. A $3 \times 3 \times 1$ Monkhorst-Pack mesh results in five k points in the irreducible part of the Brillouin zone.

Chapter 3

Methylchloride adsorption on Si(001)

3.1 Adsorption geometries and energies

Clean Si(001) surfaces reconstruct due to the dimerization of the topmost atoms. The dimers are asymmetric, consisting of an sp^2 -like bonded “down” atom, which moves closer to the plane of its three nearest neighbors, and an “up” atom, which moves away from the plane of its neighbors and possesses an s -like dangling bond. The process of rehybridization is accompanied by a charge transfer from the “down” to the “up” atom. The direction of buckling alternates within each dimer row. To reduce the energy due to relaxation of local stress and electrostatics, the buckling in the neighboring dimer rows is such that the Si(001) surface ground state is $c(4 \times 2)$ reconstructed [87, 88]. This $c(4 \times 2)$ reconstructed Si(001) surface serves as starting point for our calculations on the adsorption of methylchloride. In the following we consider a coverage of one molecule adsorbed per $c(4 \times 2)$ surface unit cell.

Fig. 3.1 shows schematically the energetically favored subset of Si(001):CH₃Cl interface configurations studied here. The nomenclature is chosen such as to indicate the character of the adsorption: P and P' denote physisorbed (or weakly adsorbed), D and D' dissociated, and F and F' fragmented configurations, where part of the molecule is ejected from the adsorption site. The clean surface will be referred to as “C” in the following.

The respective adsorption energies are given by

$$E_{\text{ad}} = E_{\text{subs}} + E_{\text{ads}} - E_{\text{subs/ads}} \quad (3.1)$$

where E_{subs} , E_{ads} and $E_{\text{subs/ads}}$ are the total energies of the substrate, the adsorbate and the substrate-adsorbate system, respectively. The calculated values are compiled in Table 3.1.

In order to obtain realistic estimates for the relative stabilities of the fragmented states F and F' we assume that, after adsorption of methylchloride, the remaining fragments are ejected into vacuum, reacting to form either Cl₂ or C₂H₆. Thus we obtain the following adsorption energies:

$$E_{\text{ad}}(F) = \left\{ E[\text{Si}(001)] + E[\text{CH}_3\text{Cl}] - \frac{1}{2}E[\text{Cl}_2] \right\} - E[\text{Si}(001)\text{CH}_3] = 0.38 \text{ eV} \quad (3.2a)$$

$$E_{\text{ad}}(F') = \left\{ E[\text{Si}(001)] + E[\text{CH}_3\text{Cl}] - \frac{1}{2}E[\text{C}_2\text{H}_6] \right\} - E[\text{Si}(001)\text{Cl}] = 1.92 \text{ eV} . \quad (3.2b)$$

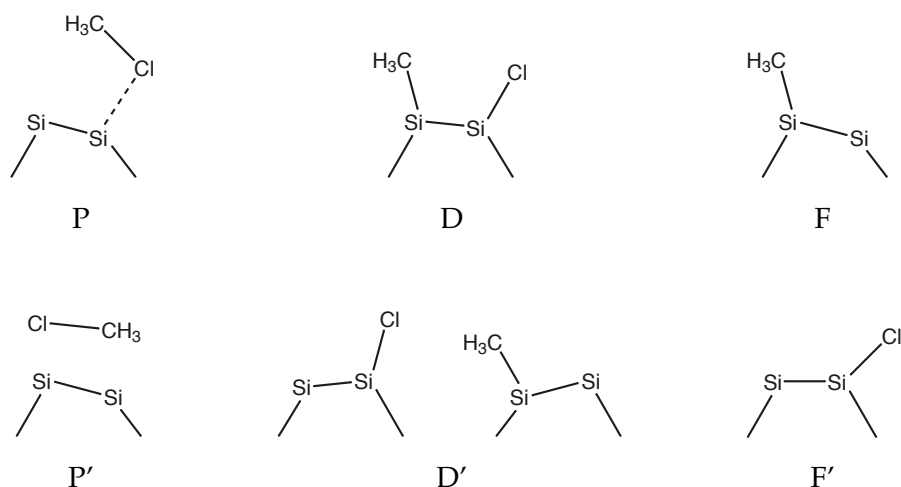


Figure 3.1: Sketches of the six adsorption geometries considered. For clarity only relevant Si surface atoms are indicated.

It is interesting to note that, assuming equilibrium of the surface with a Cl_2 or C_2H_6 reservoir, the adsorption of a single methyl group releases considerable less energy than the adsorption of chlorine. This is in agreement with the experimental observation of a $\text{Cl}:\text{CH}_3$ ratio on the surface of approximately 2:1 after heating the exposed sample to 150°C [20]. Also in Ref. 20 a pronounced tendency for the formation of extended monochloride islands was found. That can be explained by the attractive interaction between adsorbed Cl atoms, that manifests itself in the considerable increase of the adsorption energy from 1.92 to 4.11 eV upon increasing the Cl coverage from 0.125 to 1 ML. Also the interaction between the methyl groups is attractive. We find a corresponding increase of the adsorption energy from 0.38 to 0.98 eV. Due to the temperature and pressure dependence of the respective chemical potentials, however, the relative stability of F and F' will strongly depend on the preparation conditions. In fact, Brown and Ho [19] found no chlorine on the Si(001) surface for exposure temperatures $\geq 700\text{ K}$.

Table 3.1: Adsorption energies, dimer lengths and dimer angles for the geometries shown in Fig. 3.1. For comparison DFT results from Ref. 89 are included in parentheses.

model	E_{ad} [eV]	d^a [\AA]	ω^b [deg]
D	3.21 (3.07)	2.41	2.0 (2.4)
D'	2.64 (2.83)	2.34 ^c 2.43 ^d	-1.7 ^c 2.7 ^d
P	0.34 (0.29)	2.39	8.6
P'	0.32 (0.27)	2.30	4.2
F	0.38	2.34	7.8
F'	1.92	2.39	1.3

^adimer length, $d_{\text{clean}} = 2.35\text{ \AA}$

^bdimer angle, $\omega_{\text{clean}} = 10.9\text{ deg}$

^cvalue for chlorine-terminated Si dimer

^dvalue for methyl-terminated Si dimer

Our findings concerning the adsorptions geometries and adsorption energies agree very well with the results of Romero *et al.* [89], as can be seen from Table 3.1. The agreement is particularly good for the data of Ref. 89 that were obtained using the PBE parametrization [90] of the exchange and correlation energy. Romero and co-workers calculate for the structure P, for instance, adsorption energies of 0.10 and 0.29 eV, using the BLYP [91] and PBE parametrization of exchange and correlation, respectively. The latter value is very close to the 0.34 eV obtained in the present work using PW91. This is due to the fact that PBE is essentially a re-parametrization of PW91 and should therefore yield very similar adsorption energies. The deviation of the BLYP results may be attributed to the different composition of exchange (Becke [91]) and correlation (Lee, Yang, Parr [92]) parts in this functional.

In agreement with Ref. 89 as well as with the semiempirical calculations of Lee and Kim [21], we find the dissociative adsorption of methylchloride with CH₃ and Cl fragments bonded to the same dimer (structure D) to be the most favored among the investigated adsorption geometries, at least for the complete adsorption of one molecule, i.e., neglecting the formation of, e. g., monochloride dimers. Bonding of the methyl group and the chlorine to different Si dimers (structure D') leads to an adsorption energy that is lower by 0.57 eV. However, as discussed by Romero *et al.* [89], the activation energy to form structure D' may be substantially lower than the one that needs to be overcome to form configuration D.

3.2 Charge transfer

In order to quantify the charge transfer induced by the adsorption of methylchloride we calculate the spatially resolved charge density difference

$$\Delta q(\mathbf{r}) = \rho_{\text{ads/subs}}(\mathbf{r}) - \rho_{\text{subs}}(\mathbf{r}) - \rho_{\text{ads}}(\mathbf{r}), \quad (3.3)$$

where $\rho_{\text{ads/subs}}$, ρ_{subs} and ρ_{ads} are the (negative) charge densities of the relaxed adsorbate-substrate system, of the clean relaxed surface and of the adsorbate without substrate, respectively. From this quantity the number of transferred electrons,

$$Q^{\pm} = \int_{\Delta q(\mathbf{r}) \gtrless 0} d\mathbf{r} \Delta q(\mathbf{r}), \quad (3.4)$$

the length of the Q^+Q^- dipole projected onto the surface normal,

$$d_z = \frac{1}{Q^+} \int_{\Delta q(\mathbf{r}) > 0} d\mathbf{r} z \cdot \Delta q(\mathbf{r}) - \frac{1}{Q^-} \int_{\Delta q(\mathbf{r}) < 0} d\mathbf{r} z \cdot \Delta q(\mathbf{r}), \quad (3.5)$$

and the z -component of the dipole $p_z = |Q^{\pm}| d_z$ are derived. By averaging the charge density difference over the surface area we obtain the vertical charge redistribution

$$Q_{\parallel}^{\pm} = \int_{\overline{\Delta q}(z) \gtrless 0} d\mathbf{r} \overline{\Delta q}(z) \quad \text{with} \quad \overline{\Delta q}(z) = \frac{1}{A} \int_A dx dy \Delta q(\mathbf{r}). \quad (3.6)$$

The corresponding vertical charge separation length d_{\parallel} is then given by Eq. (3.5) with $\Delta q(\mathbf{r})$ replaced by $\overline{\Delta q}(z)$. The calculated values are compiled in Tab. 3.2.

Table 3.2: Characteristics of adsorbate-substrate charge transfer (see text).

model	$ Q^\pm $	$ Q_\parallel^\pm $	d_z [Å]	d_\parallel [Å]	p_z [D]
D	$3.46 e$	$0.81 e$	-0.42	-1.78	-7.0
D'	$7.02 e$	$1.15 e$	0.18	1.06	5.9
P	$2.39 e$	$0.57 e$	0.10	0.43	1.2
P'	$4.49 e$	$1.85 e$	0.83	2.00	17.9
F	$3.33 e$	$1.49 e$	0.86	1.92	13.8
F'	$4.01 e$	$0.69 e$	0.13	0.75	0.5

From these data it is obvious that the charge transfer across the interface depends strongly on the details of the bonding, in contrast to the situation of simple adsorbates like metal atoms [93]. Models based solely on the difference in electronegativity between the molecule constituents and the substrate do not necessarily hold. Only the structure D shows a charge transfer from Si towards the molecule, as might be expected from the electronegativities of 2.55 (C), 2.20 (H), 3.16 (Cl), and 1.90 (Si). The structure D', where Cl and CH₃ bond to different Si dimers, leads to a nominal charge transfer towards the substrate. The complexity of the charge transfer is due to the electronic properties of the dimerized Si(001) surface: An electric double layer is formed by filled and empty Si dimer atom dangling bonds [93]. Any changes of the dimer tilting will thus automatically result in a charge transfer along the surface normal.

3.3 Bandstructures

Our calculated surface bandstructure of clean Si(001)*c*(4×2) is shown in Figure 3.2; it exhibits a semiconducting surface with an energy gap of about 0.3 eV, in accordance with previous density-functional calculations (see, e. g., Ref. 94). The most important features in the bulk gap region are the D_{up} and D_{down} bands, corresponding to the “up” and “down” dimer contributions. There is nearly no energy dispersion perpendicular to the dimer rows, but strong dispersion along the JK line in the Brillouin zone.

Although models D and D' seem to be comparable with respect to adsorption energy and geometry, their bandstructures are clearly different. This is to be expected, given the

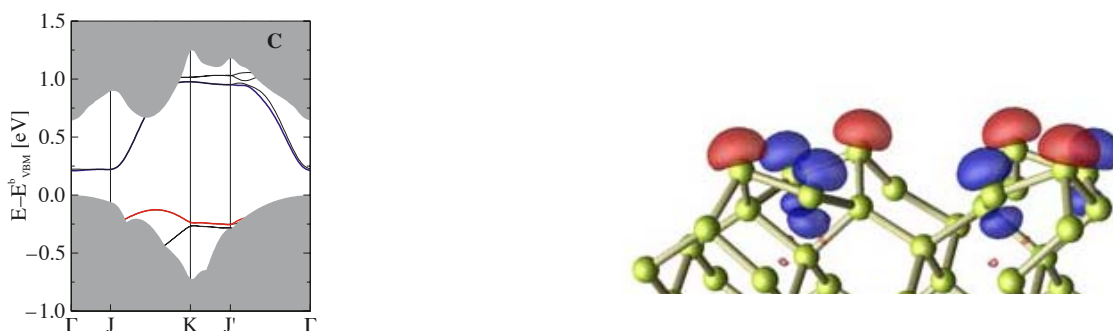


Figure 3.2: Clean surface C—Left: surface bandstructure, gray regions indicate the projected Si bulk bandstructure, red: D_{up} band, blue: D_{down} band, energies given with respect to the bulk valence band maximum (VBM); right: square moduli of the wave functions of HOMO (red) and LUMO (blue) at point K, isosurface value $0.02 e/\text{Å}^3$.

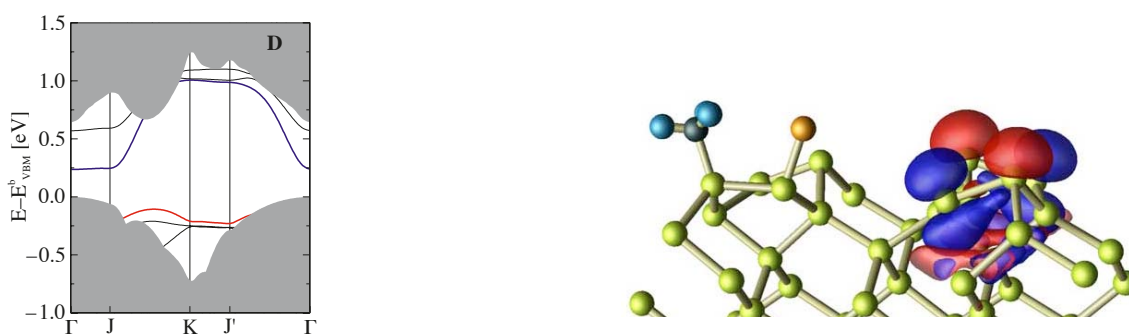


Figure 3.3: Configuration D—Left: surface bandstructure, gray regions indicate the projected Si bulk bandstructure; right: character of HOMO (red) and LUMO (blue) at point K, isosurface value $0.02 \text{ e}/\text{\AA}^3$.

fact the structure D allows for completely occupying all surface bonds, whereas D' leaves unpaired electrons in Si dimer states. Accordingly, the bandstructure of D (Fig. 3.3) is qualitatively similar to that of the clean surface, it remains semiconducting. However, the energetical degeneracy of the D_{down} bands is lifted upon adsorption. In case of the D' model the D_{up} band is shifted upwards by 0.5 eV, the D_{down} band lowered by 0.5 eV, the bands overlap and thus render the surface metallic. These electronic changes are also reflected in structural modifications of the Si surface dimers: The tilting of the chlorine-terminated (methyl-terminated) dimer is reduced to -1.7 (2.7) degrees compared to the clean surface. The energies of the Si dimer dangling bond states are thus very close and overlap due to the interaction. This also explains the result that D is energetically favored over D'. The isosurface plots of occupied and unoccupied surface states confirm the strong qualitative differences between D and D'. Whereas the orbital characters of these states for model D are similar to that of the clean surface, the corresponding wavefunctions in model D' overlap after the formation of covalent bonds between Cl and C and "down" Si atoms. *Note:* In structure D' the relative height of the Si atoms of the chlorine-terminated dimer is changed with respect to the clean surface, indicated by the minus sign of the tilting angle in Tab. 3.1. For consistency reasons in the discussion of the electronic structure, though, the nomenclature of "up" and "down" is maintained.

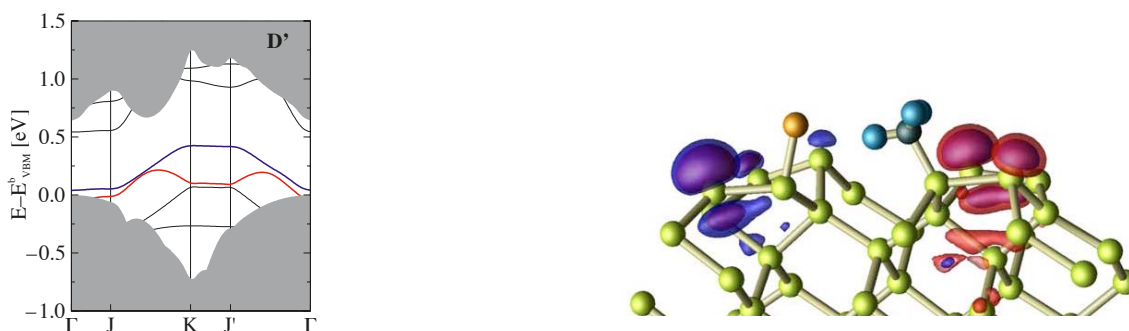


Figure 3.4: Configuration D'—Left: surface bandstructure, gray regions indicate the projected Si bulk bandstructure; right: character of HOMO (red) and LUMO (blue) at point K, isosurface value $0.02 \text{ e}/\text{\AA}^3$.

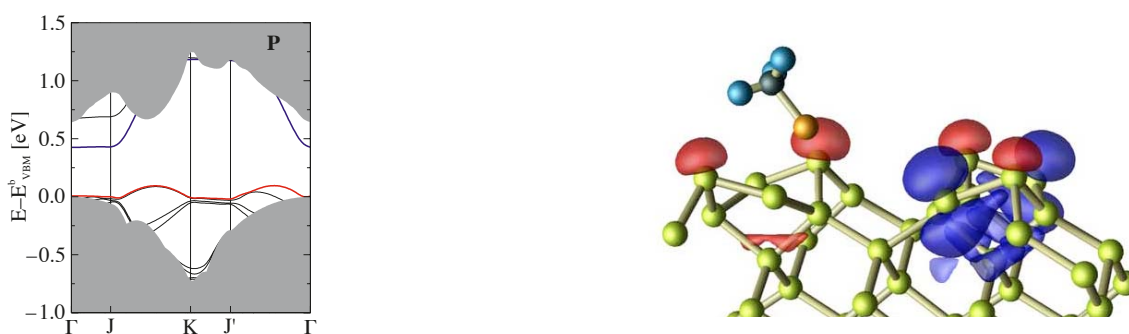


Figure 3.5: Configuration P—Left: surface bandstructure, gray regions indicate the projected Si bulk bandstructure; right: character of HOMO (red) and LUMO (blue) at point K, isosurface value $0.02 e/\text{Å}^3$.

In the models P and P' the methylchloride molecule adopts structures which hint at physisorption. In structure P a weak bond between Cl and the “down” Si atom is formed, like in the geometries D, D', F, and F', whereas model P' is the only configuration with Cl near the “up” Si atom. This difference manifests itself in the bandstructures: the Si surface bands for model P are shifted upwards by roughly 0.5 eV, thus the occupied D_{up} band now completely lies in the energy region of the Si bulk gap, whereas the unoccupied surface bands are pushed towards the bulk conduction band minimum. In configuration P' the energetic position of the D_{up} -like band remains unchanged with respect to the clean surface. The D_{down} -derived band is lowered and reaches the bulk valence band maximum; the surface thus becomes metallic. Its bandwidth is reduced to only 0.4 eV compared to 0.9 eV for the clean surface, resulting from the decrease of the dimer buckling, cf. Table 3.1.

Consistent with the reduction of the Si dimer tilting to only 1.3° , the bandwidth of the D_{down} -derived band of structure F' is only 0.25 eV, thus even smaller than for model P. The bandstructure of F, on the contrary, is again very similar to the one of P: all bands are shifted upwards by about 0.5 eV. Both in model F and F' the D_{down} -like band is occupied with one electron at K, again giving rise to a semi-metallic surface after adsorption.

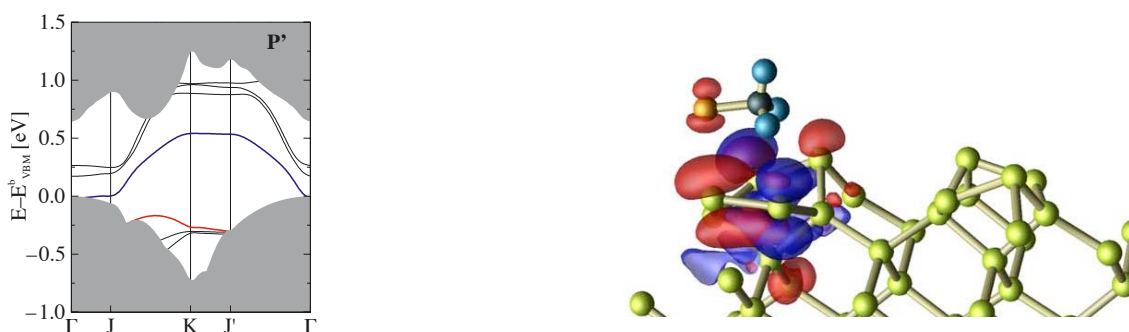


Figure 3.6: Configuration P'—Left: surface bandstructure, gray regions indicate the projected Si bulk bandstructure; right: character of HOMO (red) and LUMO (blue) at point K, isosurface value $0.02 e/\text{Å}^3$.

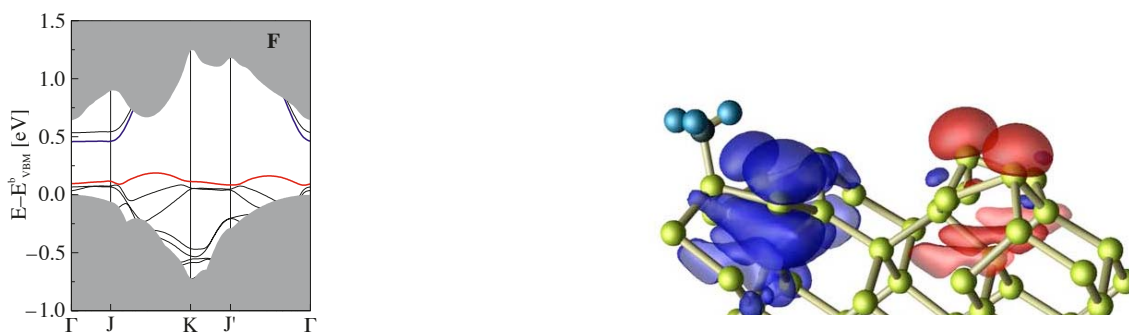


Figure 3.7: Configuration F—Left: surface bandstructure, gray regions indicate the projected Si bulk bandstructure; right: character of HOMO (red) and SOMO (singly occupied molecular orbital, blue) at point K , isosurface value $0.02 e/\text{\AA}^3$.

3.4 Surface dipoles

To account for the variation of the surface dipole layer upon adsorption of methylchloride we consider the microscopic potential

$$V_C(\mathbf{r}) = V_{ps}^{\text{loc}}(\mathbf{r}) + V_H(\mathbf{r}) + V_{XC}(\mathbf{r}) \quad (3.7)$$

calculated within DFT-GGA [95,96]. V_{ps}^{loc} , V_H and V_{XC} denote the local part of the pseudopotential, the Hartree potential and the exchange-correlation potential, respectively. The averaged and smoothed potential in $[001]$ direction is given by

$$\bar{V}_C(z) = \frac{1}{L} \int_{z-L/2}^{z+L/2} dz' \frac{1}{A} \int_A dx dy V_C(x, y, z') \quad (3.8)$$

where A corresponds to the area of the surface unit cell and L to the distance between the substrate layers. The differences $\Delta\bar{V}_C(z)$ between the Si(001):CH₃Cl interfaces and the clean relaxed Si(001) $c(4 \times 2)$ surface are shown in Fig. 3.9.

The results show that the changes of the surface dipole, corresponding to the changes of the ionization energy, cannot directly be related to the (vertical) charge transfer. For example, structures D and D' lead to a vertical charge transfer along and opposite to the direction of the surface normal. Similar observations were recently made for the adsorption of cesium on GaAs [97] and for uracil-covered Si(001) surfaces [98]. Nevertheless, in

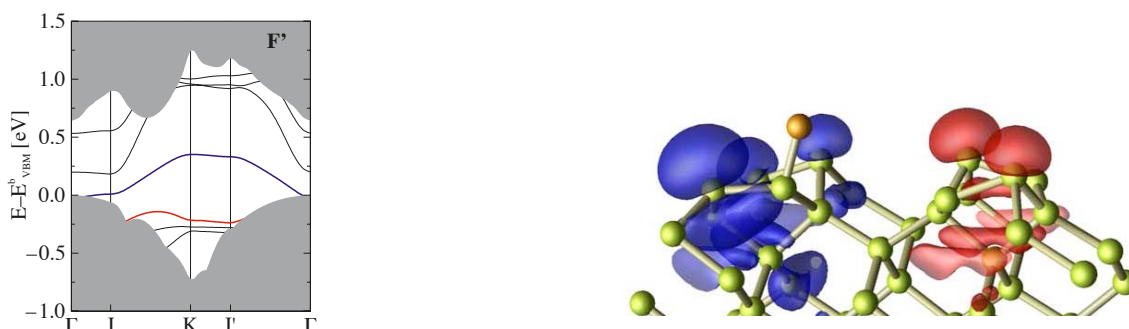


Figure 3.8: Configuration F'—Left: surface bandstructure, gray regions indicate the projected Si bulk bandstructure; right: character of HOMO (red) and SOMO (blue) at point K , isosurface value $0.02 e/\text{\AA}^3$.

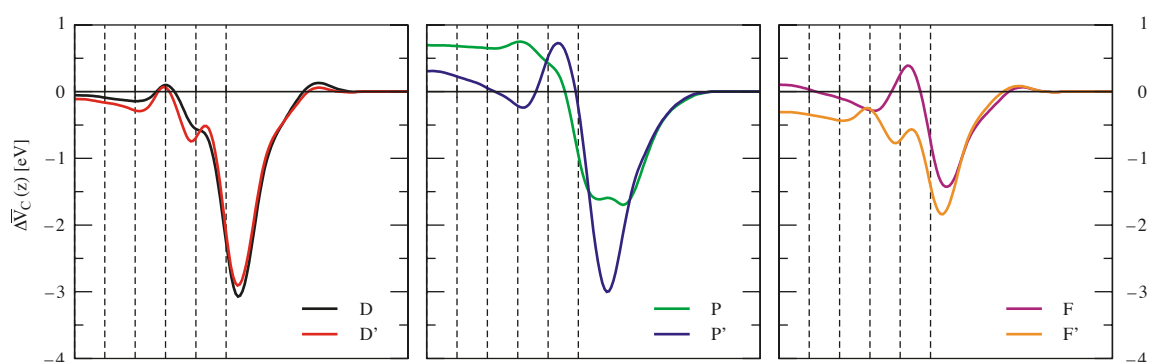


Figure 3.9: Differences of the averaged and smoothed potentials of Si(001):CH₃Cl adsorption configurations and the clean Si(001)c(4 × 2) surface plotted along the surface normal in the interface region. Dashed lines indicate the positions of the Si layers.

both cases the ionization energy is (marginally) increased compared to the clean Si surface. It can be seen that models P and P' lead to a reduction of the surface dipole potential by about 0.70 eV and 0.30 eV, respectively, so the ionization energies of the adsorbed surfaces are also lowered by the same amount. The relatively large value of 0.70 eV in the physisorbed configuration P may be attributed to the interplay between the (still quite prominent) electric dipole layer of the surface and the effective vertical dipole moment due to charge transfer from molecule to surface. For comparison, clean Si(001) surfaces experience a reduction of the ionization energy by about 0.35 eV upon exposure to atomic hydrogen [93]. The difference potentials for the fragmented structures F and F' are, in spite of an overall comparable lineshape, strikingly different. Whereas adsorption of a methyl group on a Si dimer results in a small decrease of the surface dipole by 0.10 eV, the formation of a strong covalent Si–Cl bond is sufficient to increase the surface dipole by 0.30 eV. The changes of the ionization energy for the configurations in which the Si(001) surface is completely passivated by a full monolayer of methyl groups or chlorine atoms are even more drastic: For the monochloride Si surface we find an increase of the ionization energy with respect to the clean surface of 1.04 eV, in good agreement with a previous theoretical result of 1.09 eV obtained by Krüger and Pollmann [99]. For the Si surface covered with a monolayer of methyl groups we predict a strong decrease of the ionization energy by 1.88 eV. The major part of this reduction is attributed to the dipole layer formed between the plane of the hydrogen atoms (charge depletion) and the plane of the carbon atoms (charge accumulation).

Chapter 4

Clean and pyrrole-functionalized Si- and C-terminated SiC surfaces

4.1 Surface core-level shifts

The core-level binding energy E_b that is probed by XPS is, by definition, the energy that is necessary to remove a core electron from an atom. Formally it is given by the modified total energy difference

$$E_b = E(Z(nl) - 1) - E(Z(nl)) - \varepsilon_F. \quad (4.1)$$

Here $E(Z(nl))$ denotes the ground-state energy of the system where the core state of a certain atom of species Z is characterized by the quantum numbers n and l . Correspondingly, $E(Z(nl) - 1)$ is the total energy of the system where one electron is removed from the nl core state. The calculation of the binding energy according to Eq. (4.1) necessitates the sufficient localization of the excited hole in the core of the atom but this weak condition is practically always satisfied. Usually the binding energy E_b is not measured with respect to the vacuum level, but with respect to the Fermi level ε_F of the metallic sample holder.

In order to derive structural or chemical informations about the system, the change of the binding energy due to different environments of the considered atom, the core-level shift, is studied. In particular, the surface core-level shift (SCLS) is the difference between

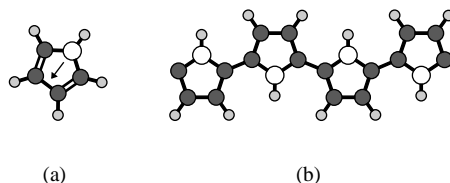


Figure 4.1: (a) Sketch of the pyrrole molecule; white (gray, small gray) discs correspond to N (C, H) atoms, respectively, double bonds are indicated, the permanent dipole moment ($\mu = 1.93$ D) of the free molecule is represented by an arrow; (b): Part of a polypyrrole (PPy) chain.

the core-level binding energies of an atom in a surface (surf) system and the same atom in a certain reference (ref) system [100]:

$$\text{SCLS} \equiv \Delta S = E_{\text{b}}^{\text{surf}} - E_{\text{b}}^{\text{ref}}. \quad (4.2)$$

The screening of the core hole by the valence electrons describes the so-called final-state effects which, consequently, give rise to the so-called final-state surface core-level shift

$$\begin{aligned} \Delta S^{\text{final}} = & [E_{\text{surf}}(Z(nl) - 1) - E_{\text{surf}}(Z(nl))] - \varepsilon_{\text{F}}^{\text{surf}} \\ & - [E_{\text{ref}}(Z(nl) - 1) - E_{\text{ref}}(Z(nl))] + \varepsilon_{\text{F}}^{\text{ref}}. \end{aligned} \quad (4.3)$$

The energies $E_{\text{surf/ref}}$ include the full response of the system towards the core hole. In the explicit calculations the rearrangement of the core-electron density is neglected. If the screening of the core hole by the valence electrons is also discarded, i. e., by employing the frozen-orbital approach resulting in energies $\tilde{E}_{\text{surf/ref}}(Z(nl) - 1)$, the total-energy differences in (4.3) reduce approximately to core-state eigenvalues $\varepsilon_{\text{c}}^{\text{surf/ref}} = \tilde{E}_{\text{surf/ref}}(Z(nl) - 1) - E_{\text{surf/ref}}(Z(nl))$ in accordance with the Koopmans' theorem [101]. Within this so-called initial-state approximation we therefore calculate the initial-state surface core-level shifts as [102, 103]

$$\Delta S^{\text{ini}} = (\varepsilon_{\text{c}}^{\text{surf}} - \varepsilon_{\text{F}}^{\text{surf}}) - (\varepsilon_{\text{c}}^{\text{ref}} - \varepsilon_{\text{F}}^{\text{ref}}). \quad (4.4)$$

The necessary modifications to the DFT code in order to obtain access to the core-state energies ε_{c} as well as to the energies $E(Z(nl) - 1)$ were implemented into VASP by Köhler and Kresse as described in Ref. 102.

We have concentrated on the nitrogen 1s (N1s) core level because nitrogen is not present on the clean surfaces and can therefore act as a direct probe for adsorbed molecules: if nitrogen is present in the XPS spectrum, then pyrrole adsorption has taken place. It is clear that the choice of the reference system is of crucial importance for the values of the calculated SCLS. Here we have examined three different systems. Isolated, gas-phase pyrrole (Py) suggests itself as the natural reference system because it is, ideally, not influenced by hard-to-control interactions. The isolated molecule has been described in a tetragonal $20 \text{ \AA} \times 20 \text{ \AA} \times 10 \text{ \AA}$ supercell. Liquid pyrrole (ℓ Py) might be closer to experimental conditions but is hard to simulate in DFT calculations. Here we have obtained a snapshot of liquid pyrrole from the following considerations: The bonding between the molecules in liquid pyrrole should be stronger than in the gas-phase, but weaker than in a molecular solid. As a compromise, eight pyrrole molecules are put in a $10 \text{ \AA} \times 10 \text{ \AA} \times 10 \text{ \AA}$ supercell so that each occupies roughly 1/8 of the cube in which each one is aligned randomly in space. Also after the full geometry optimization, no apparent order is observed so that the resulting structure is taken as a representative snapshot. Although this is a crude approximation to a liquid, we obtain an energy gain of about 0.2 eV per molecule upon liquefaction compared to the gas phase, and an average N1s core-level energy comparable to the one of the isolated molecule. In this arrangement the density of the pyrrole liquid amounts to about 0.89 g cm^{-3} compared to about 0.97 g cm^{-3} under normal experimental conditions. This slightly diluted liquid should resemble the experimentally attainable reference system closely. Both the gas-phase and the liquid reference systems have in common that the bonding between the molecules is weak so that

the systems are stabilized by physisorption rather than by chemisorption. Polypyrrole (PPy), on the other hand, is a chain molecule with strong covalent bonds between the links, Fig. 4.1(b). Although the nitrogen atom is not involved in the covalent bonding, its chemical environment is changed so drastically that the calculated initial-state SCLS are more than 1.5 eV larger than for the reference systems in which physisorption prevails as shown below. This indicates that even within the initial-state approximation the SCLS are indeed sensitive to the chemical environment and that even subtle differences between seemingly similar reference systems show up in the values. It should be noted that the calculated SCLS with respect to polypyrrole will be quoted for completeness rather than for an actual comparison to experimental values because polypyrrole was definitely not present during the measurements.

4.2 X-ray photoelectron spectra

The x-ray photoelectron spectra of pyrrole on SiC(0001) obtained after different preparation steps revealed three different bonding states of N1s electrons at binding energies of 400.3 eV, 399.6 eV and 398.0 eV. The spectra corresponding to the latter two are shown in Fig. 4.2. The component at highest binding energy (400.3 eV, not shown) was measured for a pyrrole film prepared by wetting a SiC surface in air with liquid pyrrole. That way, the N1s signal of free or physisorbed pyrrole molecules is measured. The lower N1s

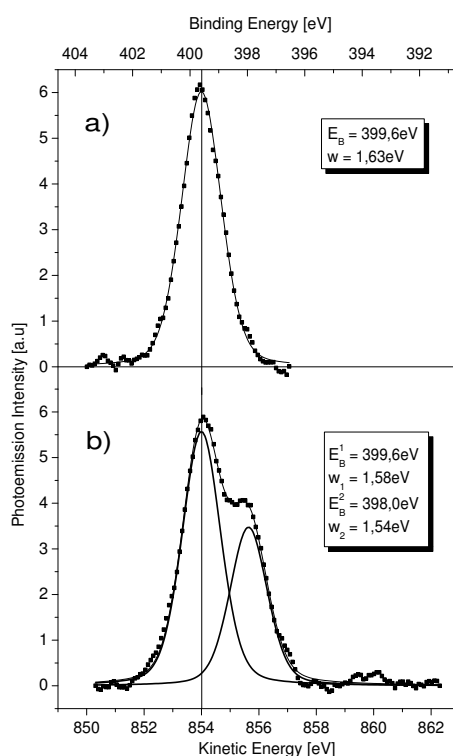


Figure 4.2: Measured nitrogen 1s photoemission signals of pyrrole evaporated in vacuum at room temperature on 6H-SiC(0001)-($\sqrt{3} \times \sqrt{3}$)R30° before (a) and after heating in ultrahigh vacuum at 700 K (b). The peak positions on the binding-energy scale and the peak widths are given in the insets.

binding energy measured at 399.6 eV on pyrrole vapor-deposited in vacuum at room temperature can be assigned to a chemical bonding of the nitrogen atom to the silicon of the SiC substrate. This finding supports the model of NH dissociation and covalent attachment of pyrrole by N-Si bonding. After heating the samples of pyrrole adsorbed on SiC at a temperature higher than 600 K in vacuum, a third component at a lower binding energy of 398.0 eV was measured. The intensity of this component increases with temperature, and the signal at 399.6 eV disappears at 900 K. The low binding energy component can be assigned to silicon nitride bonding due to decomposition of pyrrole at high temperatures.

4.3 Relation between adsorption energy and desorption temperature

To assess the stability of adsorption structures at experimental conditions it is possible to calculate approximate desorption temperatures from the adsorption energies which are equated to the height of the barrier that must be surmounted during the desorption process. The temperature-dependent desorption rate can be described by the Polanyi-Wigner equation [104, 105]

$$k_{\text{des}} = -\frac{dN}{dt} = \nu N^\kappa e^{-E_a/k_B T} \quad (4.5)$$

where N is the (temperature-dependent) number of molecules on the surface, κ the desorption order, usually 0, 1, or 2, E_a the activation or barrier energy per molecule, and ν the frequency prefactor (in s^{-1}). Temperature-programmed desorption experiments are usually conducted employing a constant heating rate β so that $T = T_0 + \beta t$. The desorption of molecules from surfaces is a first-order process, so $\kappa = 1$. The maximum desorption occurs for $dk_{\text{des}}/dt = 0$ which leads to the Randall-Wilkins expression [106]

$$\frac{E_a}{k_B T_m^2} = \frac{\nu}{\beta} e^{-E_a/k_B T_m}. \quad (4.6)$$

It can be rearranged to

$$T_m = \frac{T_c}{\ln r - \ln \frac{T_c}{T_m^2}} \equiv \frac{T_c}{\ln \frac{r}{r_0}} \quad (4.7)$$

with $T_c = E_a/k_B$, $r = \nu/\beta$ and $r_0 = T_c/T_m^2$. This transcendental equation can be solved numerically for the temperature of maximal desorption T_m with a given activation energy and plausible assumptions for the heating rate, $\beta \sim 1 \text{ K s}^{-1}$, and for the frequency prefactor ν . Consistent with the notion that the desorption takes place by occupation of vibrational modes, ν is usually chosen between 10^{12} s^{-1} and 10^{14} s^{-1} . The numerical solution of Eq. (4.7) with activation energies between 0 eV and 6 eV for fixed ratios r reveals an approximately linear relationship (correlation coefficient 0.999) between activation energy and desorption temperature that is not unexpected because $r \gg r_0$ for typical values of $r \sim 10^{13} \text{ K}^{-1}$, $T_c = E_a/k_B \sim 10^4 \text{ K}$ and $T_m \sim 100 \text{ K}$. If the explicit dependence of r_0 on the temperature T_m is neglected, r_0 (or $\ln r_0$, for that matter) can be regarded as a parameter and used in a least-squares fitting procedure. For ratios r between 10^{12} K^{-1} and $5.12 \cdot 10^{14} \text{ K}^{-1}$ it varies linearly between $r_0 = 0.02013 \text{ K}^{-1}$ and $r_0 = 0.02835 \text{ K}^{-1}$. As one

is mostly interested in a rough estimate for the desorption temperature it is sufficient to replace the varying r_0 by, e. g., the arithmetic mean of the maximal and minimal values. This results finally in the expression

$$T_m = \frac{T_c}{\ln \frac{r}{0.02424 \text{ K}^{-1}}}. \quad (4.8)$$

4.4 Clean surfaces

To simplify the notation, the Si-terminated (111)/(0001) face of SiC will be denoted Si-SiC, the C-terminated ($\bar{1}\bar{1}\bar{1}$)/(000 $\bar{1}$) face C-SiC. Si-SiC is known to exhibit a variety of surface structures, the most prominent among them the $(\sqrt{3} \times \sqrt{3})R30^\circ$ and the Si-rich 3×3 reconstruction. The most stable $\sqrt{3} \times \sqrt{3}$ reconstruction over a wide range of preparation conditions consists of a Si adatom located in a effectively fourfold coordinated site on top of an underlying second layer atom (T_4), Fig. 4.3(a) [107, 108].

The Si-rich 3×3 reconstruction contains a full Si adlayer complemented by a Si trimer and an additional Si adatom, Fig. 4.3(c) [109, 110]. These geometries have been taken as a starting point for the calculation of the structural properties of the Si-SiC surfaces. The full geometry optimization yields bond lengths and bond angles which are in excellent agreement with previous experimental and theoretical investigations.

Unfortunately, to the best of our knowledge, there exist no models for the 3×3 and $\sqrt{3} \times \sqrt{3}$ reconstructions of the C face of SiC that are generally accepted, despite a large number of studies during the last decade [111–115]. Although the $\sqrt{3} \times \sqrt{3}$ phase on the C face is not observed in the experiments conducted in this work, we include in the calculations, for the sake of completeness, a model of C-SiC($\sqrt{3} \times \sqrt{3}$) $R30^\circ$ consisting of a Si adatom in a T_4 site, Fig. 4.3(b), as suggested by Sabisch *et al.* in Ref. 107. In case of the 3×3 phase of C-SiC we follow Hoster *et al.* [116] and employ a model for the 3×3 phase of C-SiC similar to the case of Si-SiC, Fig. 4.3(d): On top of the terminating carbon layer

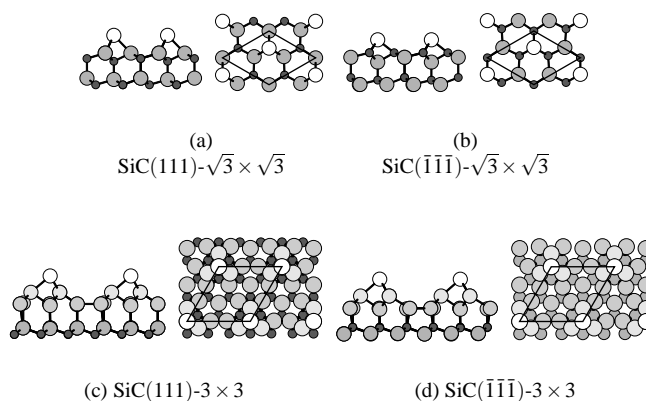


Figure 4.3: Side and top views of the $\sqrt{3} \times \sqrt{3}$ [(a) and (b)] and 3×3 [(c) and (d)] reconstructions of the Si-terminated SiC(111) and C-terminated SiC($\bar{1}\bar{1}\bar{1}$) surfaces studied here. Rhombohedral surface unit cells are indicated by solid lines. Si atoms are depicted as large circles with varying degrees of grayness, C atoms as small dark circles. The white Si adatoms are located in T_4 sites. In the 3×3 reconstructions the Si trimer atoms on the additional full Si adlayer are found in threefold-coordinated hollow sites.

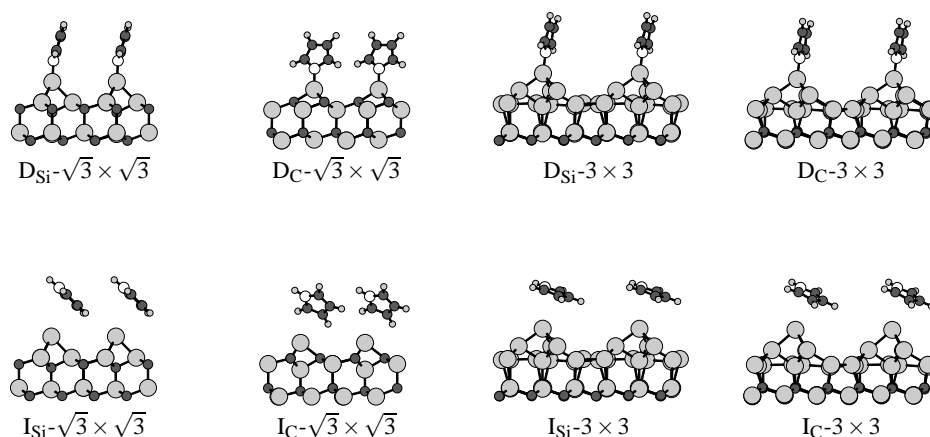


Figure 4.4: Dissociated (D, upper row) and intact (I, lower row) adsorption structures of pyrrole on SiC surfaces with normals parallel to the bilayer stacking direction. The N atom of the five-membered pyrrole ring is rendered as a white circle, the C atoms as gray circles. The indices Si and C refer to the Si-face and C-face adsorption structures, respectively.

a Si wetting layer appears which is covered by the Si tetramer. The surface unit cell thus contains one dangling bond on the topmost Si adatom, in accordance with valence band emission spectra recorded by Li and Tsong [117].

4.5 Pyrrole-adsorbed surfaces

Relaxed bonding geometries resulting from the calculations are depicted in Fig. 4.4 (see Fig. 4.5 for the definition of the tilt angle between molecule and surface normal). In the eight adsorption models studied here the starting geometry was that of the relaxed substrate structure plus one pyrrole molecule (save one H atom in the dissociated case) lying flat on the surface with the N atom about 1 Å away from the Si adatom. In this way it can be ensured that there is a substantial initial repulsive force acting on the atoms of the molecules that drives the structural optimization. The resulting Si-N distances are larger than 1 Å in all cases studied here (Table 4.1). Neither for the choice of the initial pyrrole position nor during the structural relaxation any symmetry considerations or constraints have been employed, molecular as well as substrate atoms were completely free to relax. The computed key structural parameters are listed in Table 4.1. The models have in common that the translational symmetry of the clean surface is kept; furthermore, in agree-

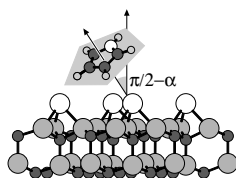


Figure 4.5: Definition of the tilt angle α between the molecular plane and the SiC surface normal. White (gray, small gray) circles correspond to N (C, H) atoms, respectively, large white and gray circles in the substrate represent Si atoms.

Table 4.1: Calculated key structural parameters of the pyrrole adsorbate structures. α corresponds to the tilt angle between the pyrrole molecular plane and the surface normal vector as defined in Fig. 4.5, N-Si denotes the nitrogen-silicon bond length and $A-X_{T_i}$ ($i = 1, 2, 3$) the distance from the Si adatom to the nearest three substrate atoms ($X = C$ for $D_C-\sqrt{3} \times \sqrt{3}$ and $I_C-\sqrt{3} \times \sqrt{3}$, else $X = Si$), and $A-X$ the corresponding distance on the clean reconstructed surface (all lengths in Å).

Surface	α	N-Si	$A-X_{T_1}$	$A-X_{T_2}$	$A-X_{T_3}$	$A-X$
$D_{Si}-\sqrt{3} \times \sqrt{3}$	16.2°	1.77	2.40	2.41	2.43	2.46
$D_C-\sqrt{3} \times \sqrt{3}$	22.7°	1.74	1.96	1.96	1.98	2.10
$D_{Si}-3 \times 3$	12.2°	1.78	2.40	2.42	2.45	2.52
$D_C-3 \times 3$	10.2°	1.76	2.38	2.41	2.42	2.56
$I_{Si}-\sqrt{3} \times \sqrt{3}$	46.0°	4.16	2.47	2.47	2.45	2.46
$I_C-\sqrt{3} \times \sqrt{3}$	42.5°	3.93	2.08	2.09	2.11	2.10
$I_{Si}-3 \times 3$	68.6°	3.48	2.46	2.47	2.49	2.52
$I_C-3 \times 3$	60.5°	3.54	2.54	2.55	2.58	2.55

ment with the LEED and XPS observations, the number of adsorbed pyrrole molecules is directly proportional to the number of dangling bonds. This observation limits the number of conceivable model geometries because it implies bonding of pyrrole at or near the surface adatom dangling bond.

4.5.1 Phase diagrams

For interfaces with different coverages, adsorption energies alone are not sufficient to assess the relative stability of the respective models. Here we simulate the experimental preparation conditions by taking into account the varying supplies of both hydrogen and pyrrole. Therefore we calculate the grand canonical potential Ω in dependence on the chemical potentials μ_P of pyrrole and μ_H of hydrogen [118],

$$\Omega = F - n_P \mu_P - n_H \mu_H, \quad (4.9)$$

where F is the free energy of the slab, and n_P and n_H are the numbers of pyrrole molecules and hydrogen atoms, respectively. Fig. 4.6 indicates that the pyrrole-adsorbate structures can hardly be stabilized if the chemical potentials of hydrogen and pyrrole vary independently. Exemplary we show the calculated two-dimensional phase diagram for the model structure $D_{Si}-\sqrt{3} \times \sqrt{3}$. The energy needed to dissociate a hydrogen atom from the pyrrole molecule amounts to about 2.8 eV so that pyrrole itself therefore acts as a hydrogen reservoir at ambient conditions. The phase diagram shows that over a wide range of hydrogen and pyrrole supplies the most favored pyrrole adsorption structure corresponds to full monolayer pyrrole coverage. The same observation is made for the other adsorption models studied here. This finding is in close agreement with a previous study of pyrrole adsorption on the Si(001) surface [119].

The presentation proceeds as follows: We discuss the structural, energetic, and electronic properties of the model systems characterized by dissociative adsorption (D) in Sec. 4.5.2 and by molecular adsorption (I) in Sec. 4.5.3. In each respective section we begin with the $\sqrt{3} \times \sqrt{3}$ reconstructions and then turn to the 3×3 reconstructions.

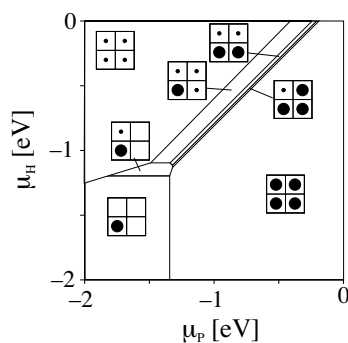


Figure 4.6: Calculated phase diagram for the model structure $D_{\text{Si}}-\sqrt{3} \times \sqrt{3}$ (periodicity doubled in direction of the surface lattice vectors) in dependence on pyrrole (μ_{P}) and hydrogen (μ_{H}) chemical potential. Zero chemical potentials correspond to the free energies of an isolated pyrrole molecule and an isolated H atom, respectively. The square icons stylize the different adsorption phases seen from above: big black disc (●): pyrrole, black dot (·): hydrogen, empty (□): free dangling bond.

4.5.2 Dissociated structures

The four relaxed D-interfaces are similar with respect to the N-Si bond length of about 1.76 Å which is characteristic for a covalent bond between nitrogen and silicon and thus confirms the experimental finding of a N-Si bond formation.

The dissociated pyrrole molecules are not exactly standing upright due to the influence of the nitrogen lone pair, but are only slightly tilted with respect to the surface normal with tilting angles α between 10.2° and 22.7°, see Table 4.1 and Fig. 4.4.

The most striking feature can be observed for the adsorbate structure $D_{\text{C}}-\sqrt{3} \times \sqrt{3}$. During the molecule adsorption the Si adatom is moved from its T_4 site into a H_3 site, see Fig. 4.3(b) and Fig. 4.4 for comparison. As the symmetry change occurs spontaneously during the geometry optimization without any additional external fields or else, the pyrrole molecule obviously lowers the small energy barrier separating the T_4 and H_3 structures of the clean C-SiC- $\sqrt{3} \times \sqrt{3}$ surface. This result shows that the properties of the C-face are remarkably different from those of the Si-face although the starting overlayer configurations strongly resemble each other and should in principle exhibit the same chemistry. This different behaviour may be related to a large extent to the different bond polarities of the Si-Si and the Si-C bonds which influence the further attachment of molecules. This conjecture is corroborated by the observation that the *structural* differences between the C- and Si-face are less pronounced for the 3×3 reconstruction where the additional Si layer reduces the effect of the terminating bilayer.

The *energetic* and *electronic* properties, however, differ drastically for the adsorption structures on the Si- and C-faces with 3×3 reconstructions. The $D_{\text{Si}}-3 \times 3$ model gives rise to a substantial adsorption energy of more than 3.0 eV, Table 4.2, while the $D_{\text{C}}-3 \times 3$ model turns out to be unstable, i. e., the total energy of the interface system is higher than the sum of total energies of substrate and adsorbate alone. Nevertheless, the geometry optimization finds that the dissociated molecule stays at the surface with a bonding between the Si adatom and the N atom which, judging from the bond length of 1.76 Å, has a covalent character. This structure corresponds to a local minimum on the total-energy surface, so consequently there must exist an energy barrier for the detachment of

Table 4.2: Calculated adsorption energies per molecule of full monolayer pyrrole/SiC interfaces, initial and final state N1s surface core-level shifts (SCLS) with respect to liquid pyrrole (ℓ Py), gas-phase pyrrole (Py), and polypyrrole (PPy).

Surface	$E_{\text{ad}} / \text{eV}$	N1s $\Delta S^{\text{ini}} / \text{eV}$			N1s $\Delta S^{\text{final}} / \text{eV}$		
		ℓ Py	Py	PPy	ℓ Py	Py	PPy
$D_{\text{Si}}-\sqrt{3} \times \sqrt{3}$	1.39	0.22	0.05	1.61	-1.39	-2.30	-0.51
$D_{\text{C}}-\sqrt{3} \times \sqrt{3}$	1.63	0.24	0.06	1.63	-1.40	-2.30	-0.52
$D_{\text{Si}}-3 \times 3$	3.18	0.25	0.08	1.64	-1.66	-2.57	-0.78
$D_{\text{C}}-3 \times 3$	-0.11	-0.54	-0.71	0.85	-1.64	-2.55	-0.76
$I_{\text{Si}}-\sqrt{3} \times \sqrt{3}$	0.08	-1.57	-1.74	-0.18	-0.61	-1.51	0.27
$I_{\text{C}}-\sqrt{3} \times \sqrt{3}$	0.14	-1.16	-1.33	0.23	-0.79	-1.69	0.09
$I_{\text{Si}}-3 \times 3$	2.14	-1.06	-1.23	0.33	-0.75	-1.66	0.13
$I_{\text{C}}-3 \times 3$	-0.87	-1.21	-1.38	0.18	-0.71	-1.61	0.17

the fragmented pyrrole which is even higher than 0.11 eV. Therefore this configuration, if realizable at all, is at best a transition state during the formation of ordered overlayers.

For the interpretation of the calculated SCLS we restrict ourselves to the values obtained with respect to liquid pyrrole. This is justified because this reference system comes closest to what is realized in the XPS experiment, see beginning of Sec. 4.5. It is remarkable to note from Tab. 4.2 that initial- and final-state SCLS, ΔS^{ini} and ΔS^{final} , for the surface models $D_{\text{Si}}-\sqrt{3} \times \sqrt{3}$, $D_{\text{C}}-\sqrt{3} \times \sqrt{3}$, and $D_{\text{Si}}-3 \times 3$ are qualitatively different as they differ in sign. This fact suggests that the screening of the core hole in the N1s state plays a major role in the adsorption system pyrrole/SiC, whereas the effect was shown to be of minor importance, e. g., for the Ga3d state of relaxed GaAs(110) surfaces [120]. Although the obtained final-state SCLS for all the four dissociated structures are, in absolute numbers, about twice as large as the experimentally determined shift of -0.7 eV for the $\sqrt{3} \times \sqrt{3}$ Si-face structure, they confirm the experimental observation that the Si-face as well as the C-face structures exhibit shifts with the same sign and in the same order of magnitude; from the x-ray photoelectron spectra of the latter (not shown) a likewise shift of -0.7 eV was derived. Moreover, anticipating the results for the intact adsorption geometries in Sec. 4.5.3, the trend of the final-state SCLS is in accordance with the chemical intuition that atoms in a physisorbed molecular overlayer experience smaller shifts than when covalently attached to the surface. The initial-state SCLS, however, would predict the largely counterintuitive reversed trend.

Thus from the SCLS alone we cannot finally prove or disprove the models for the $\sqrt{3} \times \sqrt{3}$ and 3×3 C-face, but from the negative adsorption energy the (hypothetical) $D_{\text{C}}-3 \times 3$ model turns out to be unable to support a stable molecular overlayer, and indeed the 3×3 reconstruction vanishes on the C-face after dosing with pyrrole.

4.5.3 Intact structures

The adsorption models with intact pyrrole molecules (I), see lower panel of Fig. 4.4 and Table 4.1, vary in numbers and conceptually from the dissociated ones. The adsorption of the intact pyrrole molecules on the SiC substrates does not take place by covalent attachment, but by weak physisorption in case of the models $I_{\text{Si}}-\sqrt{3} \times \sqrt{3}$ and $I_{\text{C}}-\sqrt{3} \times \sqrt{3}$ with adsorption energies of 0.08 eV (Si-face) and 0.14 eV (C-face) which are one order of

magnitude smaller than those for the $D-\sqrt{3} \times \sqrt{3}$ models. These values correspond to desorption temperatures, as calculated from Eq. (4.8), of approximately 26 K (Si-face) and 46 K (C-face) which are way below the experimentally employed vapor-deposition temperatures. Thus at room-temperature these structures are unlikely to appear in contrast to the dissociated pyrrole overlayers with high maximum desorption temperatures of about 470 K ($D_{Si}-\sqrt{3} \times \sqrt{3}$) and 520 K ($D_C-\sqrt{3} \times \sqrt{3}$).

The intact $\sqrt{3} \times \sqrt{3}$ as well as the intact 3×3 models have in common that the pyrrole molecule itself remains flat but assumes a geometry with a large tilting angle α and the NH group far away from the surface (N-Si distances between 3.4 Å and 4.2 Å). That means that the actual weak attractive interaction takes place between the dangling bond of the Si atom and the lowest-lying CH group of pyrrole. Apart from this, they differ considerably. The model $I_C-\sqrt{3} \times \sqrt{3}$ stands out because the molecule adopts a position which can be imagined to be derived from $I_{Si}-\sqrt{3} \times \sqrt{3}$ by substitution of the substrate and a rotation of the adsorbate around a molecular in-plane axis. Although no symmetry change of the Si adatom occurs as in model $D_C-\sqrt{3} \times \sqrt{3}$, the situations are comparable because they show the drastic influence of the nominal surface termination on the molecular adsorption pathway due to the differences in bond polarities.

The intact pyrrole adsorption structures on the 3×3 reconstructed surfaces, on the other hand, are *structurally* similar to each other as it is observed for the respective dissociated adsorption models whereas the *energetics* is found to be antipodal: we predict the $I_{Si}-3 \times 3$ model to be stable with an accompanying energy gain of 2.1 eV whereas the formation of the geometrically alike $I_C-3 \times 3$ model is strongly endothermic with a necessary energy expense of more than 0.8 eV. The relatively high adsorption energy of 2.1 eV for the $I_{Si}-3 \times 3$ model obviously contradicts the identification of this model as a physisorbed structure although the calculated N-Si distance of 3.48 Å is about twice as large as the sum of the covalent radii of N and Si. A possible explanation is that the main contribution to the adsorption energy arises not from the interaction between the adsorbate and the substrate, but from the intermolecular interaction of the pyrrole overlayer. It is stronger than in the intact $\sqrt{3} \times \sqrt{3}$ models because of the substantially larger tilting angle α of 68.6°. Apparently, the smaller tilting angle of 60.5° in the $I_C-3 \times 3$ model corresponds to a smaller lateral interaction that is not sufficient to lead to a positive adsorption energy.

Again, initial-state and final-state SCSL predict contradicting trends. The initial-state SCLS have large negative values ΔS^{ini} of the order of -1.5 eV that indicate a strong change of the atomic nitrogen potential upon intact molecular adsorption, although with respect to liquid pyrrole one expects these changes to be small because the chemical environment of the corresponding nitrogen atom is, at least in an atomic picture, very similar both in the adsorbate and in the reference system. Nevertheless, the final-state SCLS of the order of -0.7 eV show that there is indeed a change of the chemical environment but which is less pronounced than in the case of the dissociated adsorption geometries: the SCLS for the I models are smaller by a factor of 2 than for the D models. From the comparison of final-state SCLS to the experimental shift of -0.7 eV one could be tempted to conclude that the intact adsorption geometries are the ones that are realized in the experiments. However, this interpretation falls short of taking into account the systematically lower adsorption energies of the I models that hamper their occurrence at the experimen-

tal preparation temperatures, see beginning of this Section. Considering the uncertainties of the theoretical models the calculated SCLS are in any case to be interpreted with due caution. Moreover, even the final-state approximation does not include the possible rearrangement of the remaining core electrons.

Especially for the N1s state this effect is expected to lead to a substantial change in the core-level shifts because the extraction of one of the two *s* electrons strongly modifies the character of the state. In the case of the Ga3*d* state, mentioned in Sec. 4.5.2, the emission of one of the ten *d* electrons should alter the state only slightly. Therefore the shifts alone are not sufficient to obtain a final decision on the realized adsorption geometries.

Chapter 5

Vibrational spectra of NH₃, C₆H₆, and C₆H₆/Si(001)

5.1 Ammonia

Ammonia (NH₃) has been described and geometry-optimized in a 20 Å × 20 Å × 20 Å cubic unit cell with the three N-H bonds aligned parallel to the corner-to-corner diagonals of the cube. This arrangement results in identical N-H bond lengths of 1.020 Å and a H-N-H angle of 107.6°, both in close agreement with the values of 1.012 Å and 106.7° from Ref. 121. Furthermore, the correct C_{3v} symmetry is recovered. If, on the other hand, the molecule is aligned in a different way in the supercell, the incorrect C_{2v} symmetry is determined by the ab-initio code. Reasons and remedies for this and related problems are discussed in more detail in Sec. 2.3.3 on page 19 *et seq.*

Ammonia has a computed permanent dipole moment of 1.470 D very close to the experimental value [121] of $\mu_{\text{exp}} = 1.471$ D. During the calculation of the IR intensities with displacements of 0.05 Å in the positive and negative Cartesian directions it is changed by about 0.03 D. The C_{3v} group to which ammonia belongs consists of the identity operation E , two three-fold rotation axes C_3 and three vertical mirror planes σ_v , in total three classes and therefore three irreducible representations. As each normal mode of vibration forms a basis for an irreducible representation of the point group of the molecule, the symmetry of the normal modes can be identified beforehand without knowing their shape. To this end it is convenient to determine the action of the symmetry elements of the respective point group on the atoms constituting the molecule in a Cartesian basis. With a Cartesian coordinate system attached to each atom of the molecule, this leads to a (in general) reducible representation in the form of a $3N \times 3N$ matrix. The characters of these representation matrices under the symmetry operations of the point group C_{3v} read for ammonia

$$\Gamma_E = 12, \quad \Gamma_{C_3} = 0, \quad \Gamma_{\sigma_v} = 2. \quad (5.1)$$

Employing the standard notation of the C_{3v} character table [122], this representation reduces to

$$\Gamma_{\text{tot}} = 3A_1 + A_2 + 4E. \quad (5.2)$$

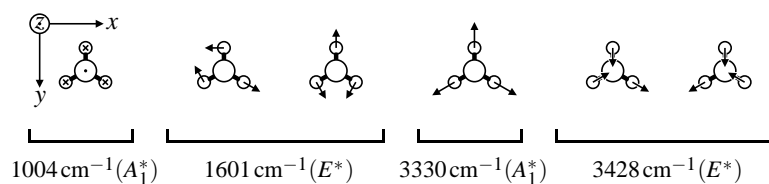


Figure 5.1: Graphic representation of the normal modes of ammonia and their symmetry classification. N (H) atoms are shown as large (small) circles. The out-of-plane “umbrella” mode is depicted in such a way that atoms bearing dots (crosses) are displaced forwards (backwards). For the in-plane modes arrows (to scale for each mode) indicate atomic displacements in the paper plane. Infrared-active modes are labeled with an asterisk.

As we are interested in pure vibrations only we have to subtract the representations corresponding to pure translations and pure rotations. Doing this, we finally obtain

$$\Gamma_{\text{vib}} = 2A_1 + 2E. \quad (5.3)$$

Thus the six possible pure vibrations of the ammonia molecule belong to two one-dimensional and to two two-dimensional representations. Further inspection of the character table shows that all of them are symmetry-allowed, i. e., are IR active and thus may also occur in an electron energy loss spectrum.

From the solution of the eigenvalue problem (2.30) of the vibrating lattice we not only obtain frequencies and mode intensities of a certain spectrum in an easy way, but also the displacement patterns of the normal coordinates. That means, above a quantitative analysis, we can also graphically describe the vibrations. The vibrational modes of ammonia are depicted in Fig. 5.1. They clearly reflect the symmetry of the C_{3v} point group. The symmetry classification according to the irreducible representations is done as follows: If a normal mode, say, $q^{(i)}$, belongs to a one-dimensional representation, any symmetry operation S of the group will carry $q^{(i)}$ on itself or its negative self:

$$Sq^{(i)} = \pm q^{(i)}. \quad (5.4)$$

The symmetry operation can be expressed in a $3N \times 3N$ matrix (which already exists from the above determination of the symmetry species of the normal modes) and applied to the respective eigenvector. The resulting signs for S running through the symmetry operations are collected and compared to the character table. If, on the other hand, an eigenvalue, say, ω_k , is two-fold degenerate, the corresponding eigenvectors $q_1^{(k)}$ and $q_2^{(k)}$ span a two-dimensional subspace in the eigenspace. Thus any symmetry operation S of the group applied to one of the $q_j^{(k)}$ will result in a linear combination of these two:

$$S \begin{pmatrix} q_1^{(k)} \\ q_2^{(k)} \end{pmatrix} = \begin{pmatrix} \alpha_1 & \beta_1 \\ \alpha_2 & \beta_2 \end{pmatrix} \begin{pmatrix} q_1^{(k)} \\ q_2^{(k)} \end{pmatrix}. \quad (5.5)$$

The traces of the coefficient matrices for S running through the symmetry elements are exactly the characters of the two-dimensional representation to which $q_1^{(k)}$ and $q_2^{(k)}$ belong. In other words, $q_1^{(k)}$ and $q_2^{(k)}$ together generate a certain representation or, put in a third way, $q_1^{(k)}$ and $q_2^{(k)}$ together transform according to the two-dimensional representation.

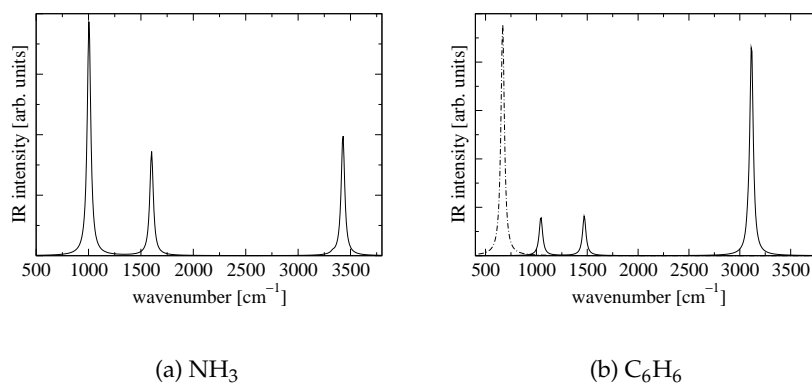


Figure 5.2: Infrared spectrum of gas-phase (a) ammonia (NH_3) and (b) benzene (C_6H_6) calculated using the computed eigenfrequencies from Eq. (2.30) and the relative intensities from Eq. (2.34). For ammonia the total intensity contribution is drawn as a solid line, for benzene the in-plane (out-of-plane) intensity contribution is drawn as a solid (dash-dotted) line. A Lorentzian broadening of 20 cm^{-1} has been applied.

This last mode of speaking becomes clear when looking at the E modes of ammonia: neither one nor the other vibration alone transforms according to the elements of the C_{3v} point group.

Due to the symmetry-induced degeneracy of the E vibrational modes the spectrum in Fig. 5.2(a) consists of only four peaks of which, accidentally, the transition (in parentheses: experimental values from Ref. 123) at 3330 cm^{-1} (3337 cm^{-1}) has, though symmetry-allowed as the corresponding normal mode belongs to the A_1 representation, a very low oscillator strength. The first peak at 1004 cm^{-1} (968 cm^{-1}) corresponds to the normal mode which may be pictorially imagined as the totally symmetric bending or “umbrella” mode, Fig. 5.1, and as such belongs to the totally symmetric A_1 representation. The second peak is due to the collective excitation of the normal modes belonging to the two-fold degenerate frequency of 1601 cm^{-1} (1628 cm^{-1}); the eigenvectors in the corresponding subspace together transform according to the E representation. Each such eigenmode consists of a bond stretching and a bond bending. The totally symmetric A_1 stretching mode at 3330 cm^{-1} does not show up in the spectrum. The fourth peak is a result from the excitation of the two degenerate E eigenmodes with a frequency of 3428 cm^{-1} (3414 cm^{-1}), consisting of bond stretches and contractions. We state an excellent agreement between calculated and measured vibrational frequencies for ammonia: The spectral distance of the A_1 (E) modes is slightly underestimated (overestimated) by 1.8% (2.3%). The absolute differences vary between 3.7% for the lowest A_1 mode and 0.4% for the highest E modes.

5.2 Benzene

Benzene (C_6H_6) has been calculated and geometry-optimized using a hexagonal supercell with primitive basis vectors $\mathbf{a} = a(1, 0, 0)$, $\mathbf{b} = a(-1/2, \sqrt{3}/2, 0)$, and $\mathbf{c} = (0, 0, c)$ with $a = c = 20 \text{ \AA}$. The molecule plane has been aligned parallel to the \mathbf{a} - \mathbf{b} -plane, and two

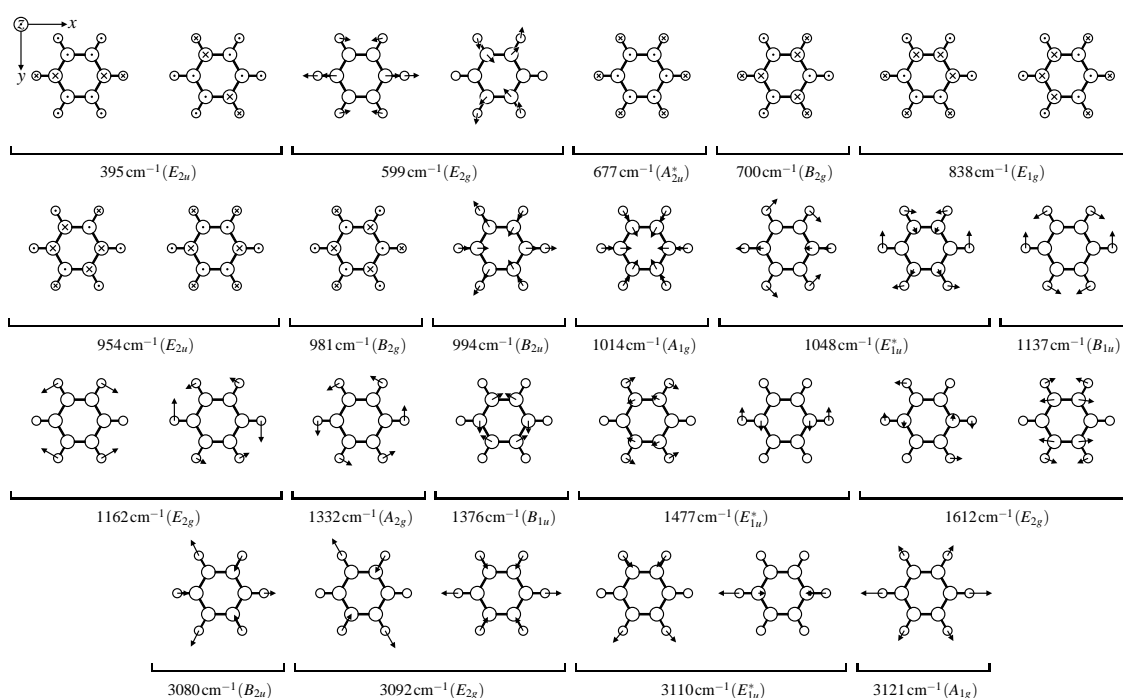


Figure 5.3: Graphic representation of the normal modes of benzene and their symmetry classification. C (H) atoms are shown as large (small) circles. Out-of-plane modes are depicted in such a way that atoms bearing dots (crosses) are displaced forwards (backwards). For the in-plane modes arrows (to scale for each mode) indicate atomic displacements in the paper plane. Infrared-active modes are labeled with an asterisk.

C-C bonds parallel to the a and b axes. This arrangement results in C-C bond lengths of 1.398 Å and C-H bond lengths of 1.095 Å (experimental values from Ref. 121 are 1.399 Å and 1.101 Å, respectively). The correct D_{6h} symmetry demanded by the Kekulé structure is indeed determined by the internal symmetry analysis routine of the employed ab-initio code VASP because of the suitably chosen supercell and molecule arrangement, cf. Sec. 2.3.3.

The vibrations of the benzene molecule can be classified according to the irreducible representations of the D_{6h} point group. Employing the above-mentioned strategy of determining the (reducible) representation in a Cartesian basis, reducing it and omitting pure translational and pure rotational contributions, we end up with in total 30 vibrational modes,

$$\begin{aligned} \Gamma_{\text{vib}} = & 2A_{1g} + A_{2g} + 2B_{2g} + E_{1g} + 4E_{2g} \\ & + A_{2u} + 2B_{1u} + 2B_{2u} + 3E_{1u} + 2E_{2u}. \end{aligned} \quad (5.6)$$

All the vibrational modes of benzene are graphically represented in Fig. 5.3. This figure also indicates their symmetry classifications and the corresponding eigenfrequencies. Only those modes in Eq. (5.6) belonging to the A_{2u} or E_{1u} representation are IR active. These modes show up in the spectrum in Fig. 5.2(b): The A_{2u} out-of-plane mode (in parentheses: experimental values from Ref. 123) excited at 677 cm⁻¹ (673 cm⁻¹) is indeed antisymmetric with respect to a C_2 axis perpendicular to the principal axis. The remaining three peaks in the spectrum at 1048 cm⁻¹ (1038 cm⁻¹), 1477 cm⁻¹ (1484 cm⁻¹), and

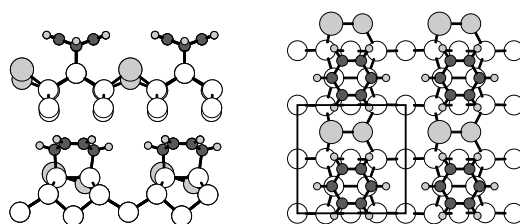


Figure 5.4: Side views along the $[011]$ - and $[0\bar{1}1]$ -directions and top view of benzene adsorbed in a butterfly fashion on the $\text{Si}(001)$ surface. Si atoms are sketched as large white circles, Si dimer atoms with no bonds to benzene as large gray circles, “up” and “down” dimer atoms are distinguished by size. Dark gray circles correspond to C atoms, small gray circles to H atoms. The 2×2 surface unit cell is indicated by a rectangle.

3110 cm^{-1} (3048 cm^{-1}) are due to excitations of normal modes which transform according to the E_{1u} representation of the D_{6h} point group.

The typical variation between the computed and measured eigenfrequencies amounts to 0.7%. Only for the highest allowed modes this discrepancy slightly increases to 2%. Again we may state an excellent description of the vibrational problem of the gas-phase benzene molecule within the developed supercell approach. Together with the good results obtained for other molecules, here shown for ammonia in Sec. 5.1, we suggest that the presented method should be also applicable to more complex systems, i. e., molecules adsorbed on solid substrates.

Here two remarks are appropriate concerning the method. Firstly, of course numerical errors are inevitably introduced by the applied finite-difference approach to molecular motion. This leads to a small numerical lifting of degeneracies where the frequency differences between analytically degenerate modes increase the higher the vibrational energy becomes. The low-frequency E_{2u} modes at 395 cm^{-1} , e. g., are numerically degenerate within 1 cm^{-1} whereas the high-frequency E_{1u} modes at 3110 cm^{-1} are seemingly separated by 10 cm^{-1} . Despite of this error, the symmetry analysis applied to the calculated normal mode vectors indeed recovers all the irreducible representations noted in (5.6) correctly.

Secondly, due to the extremely high symmetry of the benzene molecule, the force constant matrix only has very few independent elements, so in principle it would suffice to displace one H and one C atom to obtain the full matrix with symmetry considerations. This could alleviate some of the numerical problems and may prove useful to save computational time in some cases, but it is restricted to high-symmetry systems. In the case of benzene on $\text{Si}(001)$ we only find a C_1 symmetry for the total system. Nevertheless, we believe that a symmetry analysis of the adsorbed species (where applicable) alone treated as an isolated molecule is important to be better able to assess the changes that occur to the vibrations when adsorbed on the surface, with respect to the frequencies and to the intensities, but as well to the displacement patterns of the normal modes.

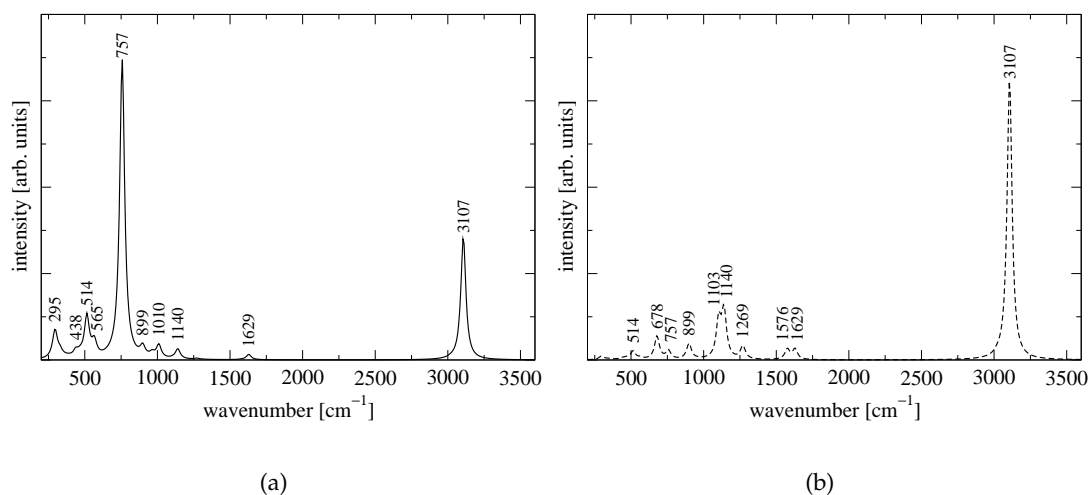


Figure 5.5: IR spectrum of benzene adsorbed on Si(001). The solid line (a) represents the out-of-plane contributions, the dashed line (b) the in-plane contributions. Fundamental vibrations accompanied with a non-zero transition matrix element are referred to by their respective wavenumbers (in cm^{-1}).

5.3 Benzene adsorbed on Si(001)

Various experimental and theoretical work [124–129] has been devoted to the adsorption of benzene on the Si(001) surface which emerged in the general agreement that benzene adsorbs in a butterfly fashion. Other suggested bonding geometries turned instead out to be either unstable or metastable. Thus we have started the structural optimization with a geometry such that the benzene (1,4) C atoms are aligned parallel to one Si dimer where we employed the asymmetrically buckled dimer model of the 2×2 reconstructed Si(001) surface. The indeed resulting 1,4-cyclohexadiene-like butterfly geometry is depicted in Fig. 5.4. It is seen that because of the size of the benzene molecule full monolayer coverage corresponds to one benzene molecule per 2×2 surface unit cell. So benzene relaxes from the planar gas-phase geometry with D_{6h} symmetry to a tilted cyclohexadiene structure with C_{2v} symmetry when adsorbed on Si(001). Despite of this drastic reduction of symmetry it is still possible to uniquely relate the displacement patterns of the vibrations of the adsorbed species to those of the isolated benzene molecule.

Resulting from the interaction with the delocalized π -electron system of benzene, the buckling of the dimer with bonds to benzene vanishes whereas the buckling angle of the remaining Si dimer is essentially unchanged. This is in contrast to the cluster calculations done in Ref. 129 where the authors have *a priori* assumed a C_{2v} symmetry of the entire benzene/Si(001) adsorbate-substrate system. We find, though, that the buckling of the free dimer remains, but this does not affect the results because the vibration of the free Si dimer is a low-frequency lattice vibration that does not mix with the adsorbate-induced or adsorbate-dominated vibrations we are primarily interested in.

The calculated vibrational spectrum of benzene adsorbed on Si(001) is shown in Fig. 5.5. It is divided in out-of-plane (a) and in-plane (b) contributions. Here the terms “out-of-plane” means the intensity resulting from the dynamical dipole perpendicular

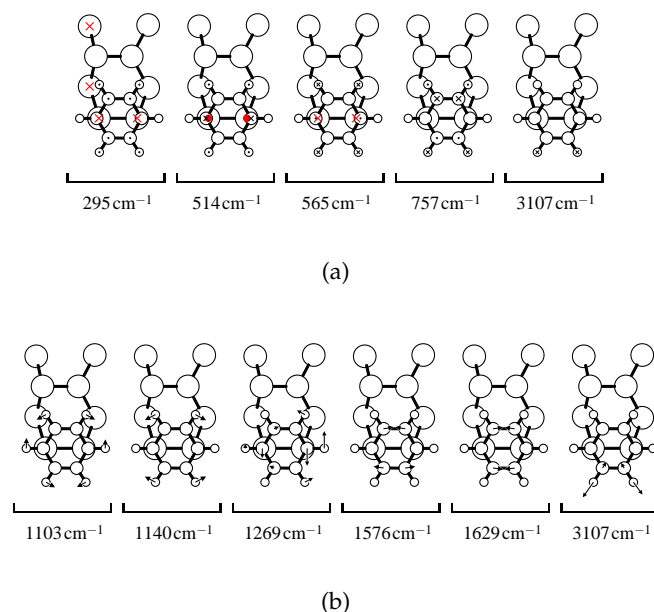


Figure 5.6: Graphic representation of a selection of the IR- or HREELS-active (a) out-of-plane modes and (b) in-plane modes of vibration of benzene adsorbed on Si(001). C (H) atoms are shown as medium-sized (small) circles and Si atoms as large circles. The out-of-plane modes are depicted in such a way that atoms bearing dots (crosses) are displaced forwards (backwards). Red dots and circles belong to distortions of substrate atoms. For the in-plane-modes the small arrows (to scale for each mode) indicate the displacements of the respective atoms.

to the surface where “in-plane” corresponds to the components parallel to the surface. Obviously, the spectrum is much richer than that of the isolated benzene molecule because of the reduced symmetry and the interaction with the substrate. Nevertheless it is possible to interpret the origin of most of the major peaks in terms of the vibrations of gas-phase benzene. To that end we compare the form and frequencies of the vibrations of the adsorbate-substrate system as depicted in Fig. 5.6 with the benzene modes as shown in Fig. 5.3. Afterwards we will identify common features in the calculated and measured HREEL spectrum.

We begin with the most important out-of-plane modes shown in Fig. 5.6(a). Although Si atoms are involved in the 295 cm^{-1} mode, the major displacements take place within the adsorbate which is found to correspond to one of the E_{2u} benzene modes with a frequency of 395 cm^{-1} (cf. Fig. 5.3). So this mode is softened by 100 cm^{-1} due to the interaction with the substrate. An additional feature seen in Fig. 5.6(a) for the 295 cm^{-1} mode is the symmetric up-and-down vibration of the Si dimer the benzene molecule is bonded to. The largest out-of-plane intensity peak at 757 cm^{-1} originates clearly from one of the E_{1g} modes at 838 cm^{-1} ; the frequency shift of 81 cm^{-1} is related to the nearly complete immobilization of the two C atoms forming bonds to the surface Si dimer. The second largest peak at 3107 cm^{-1} results from the E_{1u} mode at 3110 cm^{-1} of benzene. It is shifted by merely 2 cm^{-1} and as such is characteristic for the adsorbate itself, in this case of a C-H stretch; the substrate influence is nearly negligible.

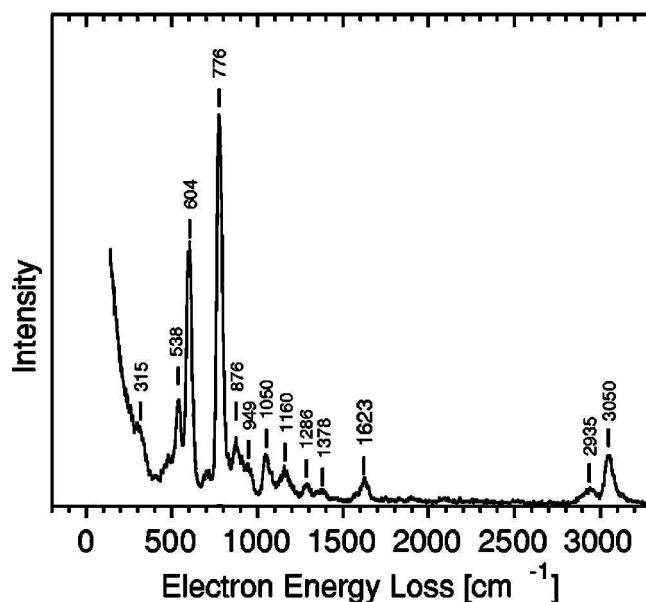


Figure 5.7: Measured HREEL spectrum (modified version of the figure in Staufer *et al.* [129])

The major in-plane modes and their coupling to the electromagnetic field or to electrons are characterized by the spectrum in Fig. 5.6(b). The peak at 1103 cm^{-1} is the result of the excitation of a B_{1u} -like normal mode of benzene at 1137 cm^{-1} which is redshifted by 36 cm^{-1} due to the molecule-substrate interaction. The 1140 cm^{-1} mode in the spectrum is due to one of the E_{2g} modes with a frequency of 1162 cm^{-1} . The mode with a frequency of 1332 cm^{-1} is partly similar to the A_{2g} benzene mode at 1333 cm^{-1} . A close look at the in-plane modes at 1576 cm^{-1} and 1629 cm^{-1} shows that these two are most probably derived from the E_{2g} modes at 1612 cm^{-1} . While the symmetric C-C bond stretch at 1629 cm^{-1} is related directly to the E_{2g} mode, the asymmetric C-C bond stretch 1576 cm^{-1} obviously only becomes apparent when the molecule interacts with the surface. For a free molecule these two modes would be expected to vibrate with the same frequency, in other words, would be expected to be degenerate. The C-H stretch mode at 3107 cm^{-1} also shows up in the in-plane spectrum. All the observed redshifts and mode softening may be simply explained by an increase of the “effective masses” of the atoms due to the presence of the heavier Si atoms.

Figure 5.7 demonstrates that our simple method of calculating frequencies and intensities of vibrational transitions yields a spectrum that for the major peaks compares very well to a measured HREEL spectrum of the adsorbate complex benzene on Si(001). We directly compare the frequencies of the adsorbate modes in Fig. 5.6 with the experimental ones from Fig. 5.7 (given in parentheses). The peak related to the C-H stretching vibration is reproduced at 3107 cm^{-1} (3050 cm^{-1}), but we fail to predict the smaller peak at 2935 cm^{-1} which Staufer *et al.* [129] attribute to the (1,4) C-H stretching, i. e., involving the C atoms bonded to the Si dimer. The measured double-peak structure may be traced back to a combination of the out-of-plane and in-plane modes in Fig. 5.6 with the highest frequencies. The peak at 1629 cm^{-1} (1623 cm^{-1}) results from the excitation of the normal mode involving the symmetric stretch of the remaining two C-C double bonds of

the adsorbate. As discussed above, in the in-plane spectrum we find a mode involving the asymmetric stretch of the C-C double bonds which does not appear in the measured HREEL spectrum. The peak at 757 cm^{-1} (776 cm^{-1}) shows the highest relative intensity in the calculation as well as in the experimental spectrum; it is due to the excitation of an out-of-plane vibration of the C-C double bonds of opposite phase. We attribute the calculated frequencies of 514 cm^{-1} and 565 cm^{-1} to the experimental wavenumbers 538 cm^{-1} and 604 cm^{-1} because the displacement patterns of the corresponding normal modes are in accordance with the assignment of these modes by Staufer *et al.* Although the normal modes seem to be equivalent when looking at the projection on the surface plane, they differ considerably in amplitude. This becomes clear when keeping in mind that the mode with a frequency of 514 cm^{-1} leads to a non-vanishing contribution to the in-plane intensity as shown in Fig. 5.6(b) whereas the 565 cm^{-1} mode is forbidden in the in-plane spectrum. The first discernible experimental peak at 315 cm^{-1} we find to result from the excitation of the "butterfly-bending" normal mode with a calculated frequency of 295 cm^{-1} which we relate to the lowest-lying (395 cm^{-1}) fundamental mode of the isolated benzene molecule.

Chapter 6

Structural and spectroscopic properties of perylene adsorbed on Si(001)

6.1 Vibrational spectrum of perylene

Isolatrd perylene ($C_{20}H_{12}$) has been calculated and geometry-optimized using a hexagonal supercell with primitive basis vectors $\mathbf{a} = a(1,0,0)$, $\mathbf{b} = a(-1/2, \sqrt{3}/2, 0)$, and $\mathbf{c} = (0,0,c)$ with $a = c = 20 \text{ \AA}$. The molecule plane was aligned parallel to the \mathbf{a} - \mathbf{b} -plane, and the long perylene axis parallel to the \mathbf{a} axis. This arrangement results in C-C bond lengths between 1.377 \AA and 1.465 \AA and C-H bond lengths between 1.086 \AA and 1.090 \AA , cf. Fig. 6.1(a), in very good agreement with previous *ab initio* studies [130]. The D_{2h} point group symmetry of perylene manifests itself also in the shape of the frontier orbitals depicted in Fig. 6.1.

Each normal mode of vibration can be regarded as a basis for an irreducible representation of the respective point group. In case of perylene one expects the following

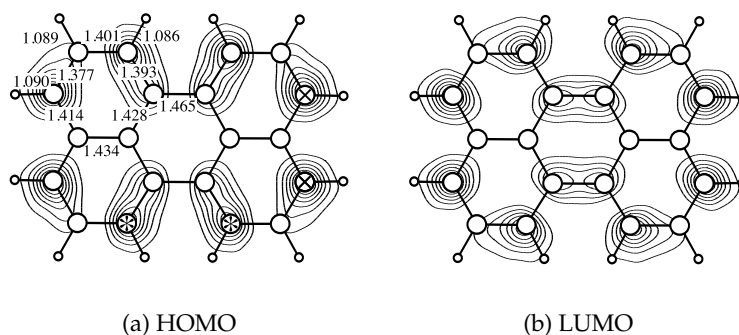


Figure 6.1: Sketch of perylene, C (H) atoms shown as large (small) circles, together with the (a) highest occupied molecular orbital and (b) lowest unoccupied molecular orbital. Lines of constant charge density are equidistantly spaced between $1 \cdot 10^{-2} e/\text{\AA}^3$ and $7 \cdot 10^{-2} e/\text{\AA}^3$. The numbers indicate the inequivalent calculated bond lengths (in \AA). The asterisks (*) and crosses (x) point to the pairs of C atoms likely to participate in a bonding to the Si substrate.

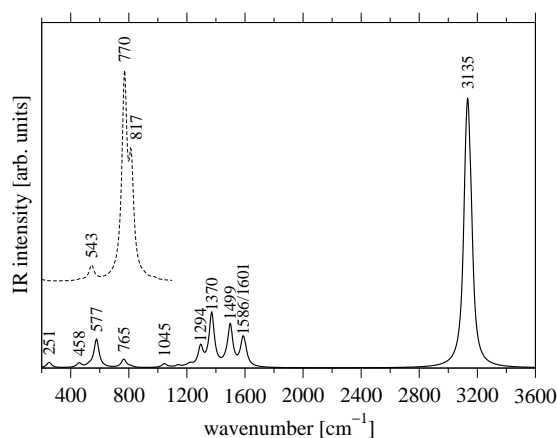


Figure 6.2: Calculated infrared spectrum of gas-phase perylene. Solid line: in-plane spectrum, dashed line: out-of-plane spectrum, shifted in vertical direction.

classification of the ninety ($3 \cdot 32 - 6$) internal molecular vibrations, employing the standard notation of the D_{2h} character table [122]:

$$\Gamma_{\text{vib}} = 16A_g + 15B_{1g} + 6B_{2g} + 8B_{3g} + 7A_u + 8B_{1u} + 15B_{2u} + 15B_{3u}. \quad (6.1)$$

All “ungerade” (u) B -modes are expected to appear in an IR spectrum because they are symmetry-allowed. So despite the high symmetry of perylene the IR spectrum with (potentially) 38 allowed modes will show a rich structure, especially taking into account that no modes are degenerate. The calculated IR spectrum is shown in Fig. 6.2 with the wavenumbers of the strongest transition indicated. In perylene, in-plane and out-of-plane modes are strictly separated; the latter have non-vanishing oscillator strengths only below 817 cm^{-1} . It is noteworthy that perylene exhibits six low-frequency vibrations (not shown in the spectrum) between 6.6 cm^{-1} (B_{3u}) and 224.4 cm^{-1} (A_u), three of which are allowed, but have very low oscillator strengths. This is an indication of the softness of this molecule as these low-frequency vibrations are associated mostly with

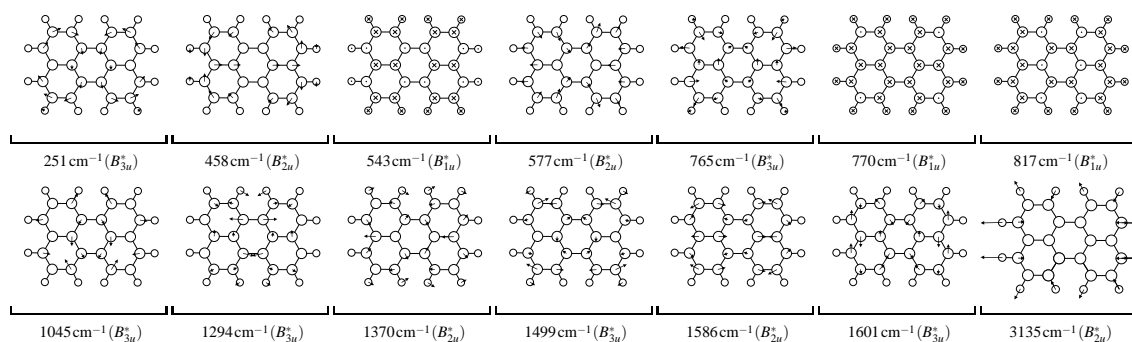


Figure 6.3: Sketch of the displacement pattern of the normal modes with non-vanishing oscillator strengths that contribute to the calculated IR spectrum in Fig. 6.2 with wavenumbers and symmetry classification. The asterisks indicate that the modes are infrared-active. C (H) atoms are shown as large (small) circles. Out-of-plane modes are depicted in such a way that atoms bearing dots (crosses) are displaced forwards (backwards). For the in-plane modes arrows (to scale for each mode) indicate atomic displacements in the paper plane.

slight ring-deformations. So it is to be expected that perylene easily could change its planar gas-phase geometry substantially when it interacts with the Si surface though it remains essentially intact.

The displacement patterns of the vibrations that contribute mainly to the gas-phase spectrum are sketched in Fig. 6.3. The strongest out-of-plane vibrations are excited at 543 cm^{-1} , 770 cm^{-1} and 817 cm^{-1} (all B_{1u}). These are predominantly out-of-plane wagging motions of the H atoms. Ten out of the eleven most important in-plane modes (from 251 cm^{-1} to 1601 cm^{-1}) are characterised mainly by bendings of the C-H bond and strong collective deformations of the carbon rings. The high-frequency mode at 3135 cm^{-1} , on the other hand, consists quasi solely of asymmetric stretches of the C-H bonds, in accordance with the expectations from experience. Compared to the experimental C-H stretch frequency of perylene (3050 cm^{-1}), we find a deviation to the calculated one by about 2.8%.

6.2 Adsorption structures

The adsorption of perylene on the Si(001) surface was studied experimentally by Rada, Chen and Richardson [29] by means of STM and HREELS. By interpretation of STM line profiles, the authors find that perylene adsorbs in an upright way with the longer molecular axis parallel to the surface in a cross-dimer (CD) configuration and forms rows perpendicular to the dimer rows of the Si(001) surface, i. e., the [110] direction. This adsorption behaviour is unexpected for two reasons. First, it contradicts the observations made for other aromatic molecules adsorbed on solid surfaces including Si(001) that adopt a more or less flat-lying geometry [25]. Second, there are geometrical objections (the following values were computed in this work): The dimer length on the Si(001)- 2×1 surface amounts to 2.34 \AA , and the dimers are separated by 3.93 \AA . The distance between the carbon atoms thought to participate in the bonding of perylene to the surface, denoted by asterisks in Fig. 6.1, is 2.94 \AA whereas the nearest short-edge carbon atoms (crosses in Fig. 6.1) of the molecule are only 2.46 \AA away from each other. So one would expect the most probable reaction pathway during adsorption to be hydrogen abstraction from the short edge of the molecule and subsequent top-dimer bonding as this process involves the least rearrangements of the geometry of both molecule and substrate, similar to the case of the adsorption of phenanthrenequinone on Si(001) [131].

To determine the adsorption geometry we consider a number of conceivable bonding scenarios for different coverages and perform a geometry optimization within the DFT and discuss the energetics of the resulting structures in terms of their adsorption energies. After that, we compare simulated STM images to the experimental one from Ref. 29. The remaining potentially possible structure models are then analyzed with respect to their vibrational spectra.

The structures treated in this study are shown in Fig. 6.4. As an exemplary structure with perylene adsorbing in a top-dimer (TD) position we have considered the geometry of Fig. 6.4(a), named lo-TD-facing, indicative of adsorption with the long axis of perylene parallel to the surface. The top-dimer arrangement gives rise to perylene rows parallel to the dimer rows and as such must be discarded as it very clearly contradicts the STM

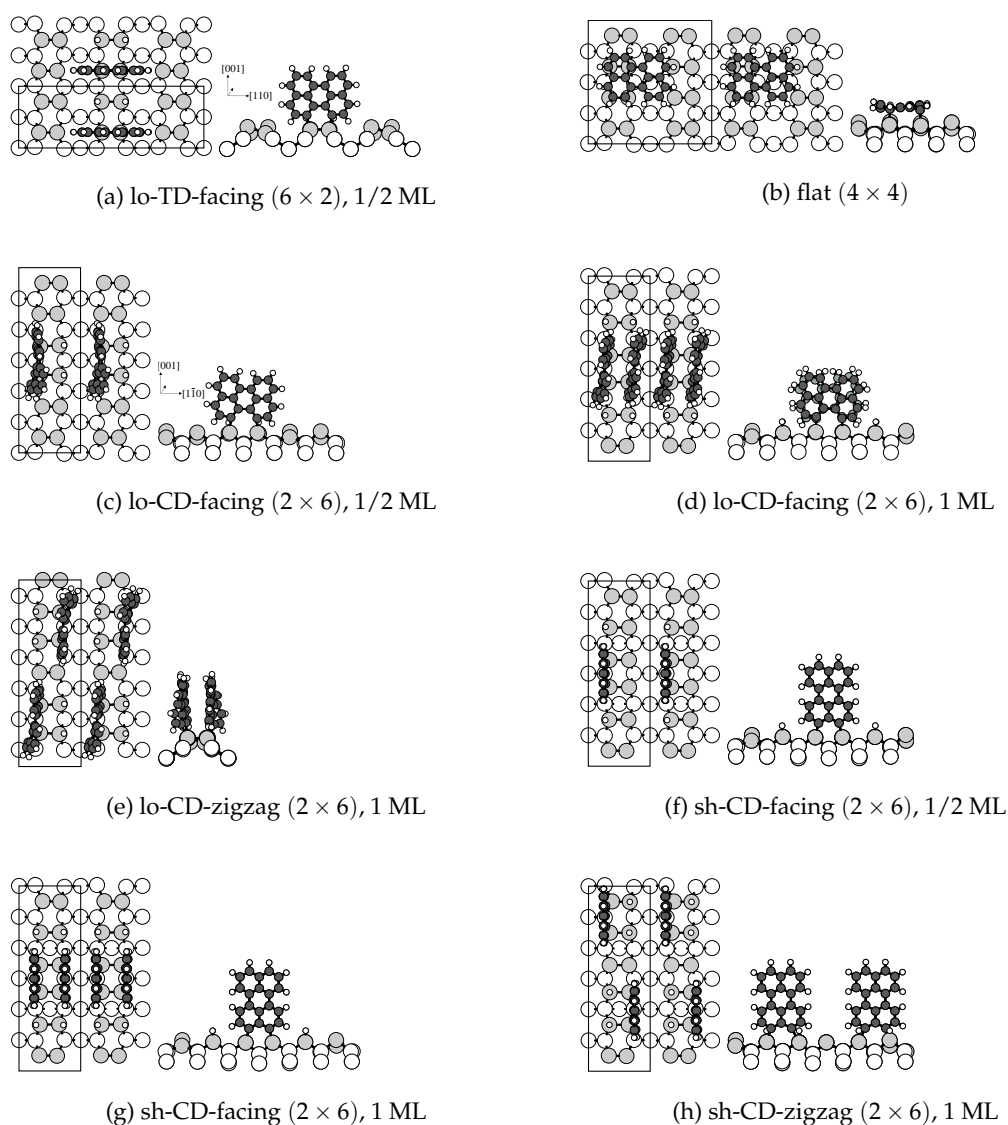


Figure 6.4: Models of adsorption of perylene on Si(001) considered in this work in top view and in side view. Large (small) white circles correspond to Si (H) atoms, medium gray circles to C atoms, and large gray circles to Si dimer atoms. Surface unit cells are indicated by rectangles. The multipliers in parentheses relate indicate the nominal periodicity.

observations of Ref. 29 (shown in Fig. 6.6). Nevertheless it gives rise to a large adsorption energy E_{ad} of 3.29 eV, cf. Table 6.1, calculated according to Eq. (3.1) so that a positive value corresponds to an energy gain. The molecule stays essentially planar upon adsorption but the lower part is slightly expanded so that it accommodates the dimer. The dimers involved in the bonding of the molecule and the remaining two hydrogen atoms become symmetric as expected upon saturation of the dangling bonds.

Figure 6.4(b) depicts the optimized structure that results when a perylene molecule is put flat on the surface, a situation that may have been believed to occur due to previous observations for the adsorption of aromatic molecules on solid surfaces. Therefore we have included this possibility in our calculations although it seems not to be consistent

Table 6.1: Adsorption energies E_{ad} (in eV) per molecule with respect to the clean 6×2 (top-dimer model, TD) or 2×6 (cross-dimer models, CD) Si(001) surface for the adsorption models considered in Fig. 6.4. For full monolayer (ML) coverage the value E'_{ad} denotes the energy gain upon adsorption of the second perylene molecule when the first molecule is already present.

model	E_{ad}	E'_{ad}
(a) lo-TD-facing, 1/2 ML	3.16	—
(b) flat	6.90	—
(c) lo-CD-facing, 1/2 ML	1.21	—
(d) lo-CD-facing, 1 ML	1.15	1.07
(e) lo-CD-zigzag, 1 ML	1.24	1.25
(f) sh-CD-facing, 1/2 ML	1.65	—
(g) sh-CD-facing, 1 ML	2.45	3.25
(h) sh-CD-zigzag, 1 ML	1.69	1.73

with experiment. Despite the very large adsorption energy of almost 7 eV this structure must be discarded, see below. It is interesting to note that there are rearrangements in the molecular framework that resemble those seen in the case of benzene adsorption on Si(001), see, e. g., Ref. 132: The constituting six-membered rings of perylene that are closest to a Si dimer adopt a frustrated butterfly geometry, the full completion of which is hampered by the strong intramolecular bonding.

The group of cross-dimer (CD), long-axis bonding structures, denoted lo-CD, is depicted in Fig. 6.4(c)–(e). The coverage is defined such that two molecules per 2×6 surface unit cell correspond to one monolayer (ML). The 6-fold repetition in [110] direction is necessary to separate the perylene chains in order to avoid mutual interaction. The first two structures in this group, lo-CD-facing with half and full monolayer coverage, share the feature that they give rise to perylene rows perpendicular to the dimer rows like in Fig. 6.6 and therefore show the observed long-range behaviour. The zigzag-structure is included for completeness. The three models have in common that the perylene molecules are subject to strong distortions upon adsorption: the left two and the right two rings of the molecule are twisted against each other by nearly 11° , determined as the angle between least-squares planes fitted against the carbon atoms in the left and the right part of the distorted molecule, respectively. This may explain the inclination of the molecules concluded from the STM observations.

The adsorption energies for the lo-CD and sh-CD structures lie between 1.07 eV and 3.25 eV. In Table 6.1 two values, E_{ad} and E'_{ad} , for the adsorption energy in case of full monolayer coverage are given. The first one is the average adsorption energy per molecule that results if two molecules are thought to approach the surface at the same time. The second one is the energy gained upon adsorption of the second molecule if the first molecule is already adsorbed at the surface. Therefore, the average adsorption energy in case of full monolayer coverage is recovered by $\bar{E}_{\text{ad}} = (E_{\text{ad}} + E'_{\text{ad}})/2$. This value is lowest, 1.07 eV, for the apparently experimentally observed adsorption model lo-CD-facing, and highest for the sh-CD-facing model, 3.25 eV. But adsorption energies are not always sufficient to assess the probability of formation because there may be huge energy barriers that thwart the realization of one or the other structure. In principle the height of these barriers could be estimated by constrained-dynamics calculations [133], but for a

large system like perylene/Si(001) they are unaffordable as yet. In other words, the structures that result from the calculations represent equilibrium geometries that may or may not be accessible under given experimental preparation conditions. Thus the values of the calculated adsorption energies are neither questionable in themselves, nor do they indicate a failure of DFT for these systems. The apparently wrong stability ordering shows, however, that total-energy calculations alone are not sufficient for complex adsorption systems like perylene/Si(001), but must be complemented by consideration of additional fingerprints, see below.

6.3 STM images

The locally integrated density of states as probed by STM may give further hints to decide which structure is the one that actually occurs. To calculate STM images we employ the Tersoff-Hamann approach [134] and show the integrated charge density between ϵ_F and $\epsilon_F + E_{\text{bias}}$ (ϵ_F : Fermi energy, E_{bias} : energy corresponding to the desired bias voltage) mapped to a plane. In order to avoid redundancy only STM images of the flat 4×4 and the full monolayer lo-CD-facing and sh-CD-facing structures are shown in Fig. 6.5. The top-dimer structure could be discarded in the first place due to the differing orientation of the perylene rows compared to experiment, the zigzag structures do not form tightly-packed, well-separated rows at all, and the molecule-molecule distances in the half-monolayer structures are too large to give rise to nearly overlapping bright spots. The flat adsorption structure appears in the simulated STM image as shown in Fig. 6.5(a): it does not remotely resemble the experimental image (Fig. 6.6) as no distinguishable row-structure emerges. So this structure, too, must now be finally rejected as a candidate for the experimentally observed adsorbed structure. The sh-CD-facing geometry, Fig. 6.5(b), shows a very regular and symmetric pattern, a result of the retaining flatness of the adsorbed species, that comes close to the experimental image and is as such a very hopeful aspirant for the realized geometry. But up to this point also the lo-CD-facing model cannot be fully ruled out, although the spot structure is slightly alternating: it

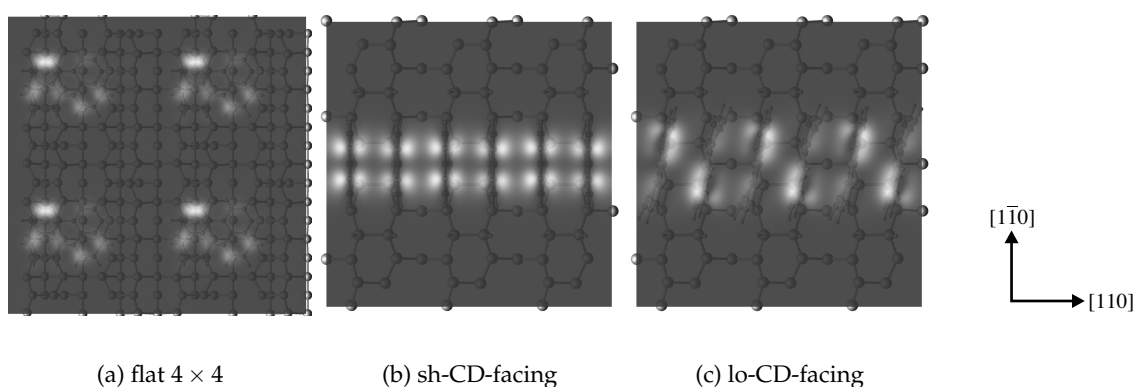


Figure 6.5: Simulated filled-state STM images with a bias voltage of -2.5 V for three exemplary perylene/Si(001) model structures. The imaging plane is placed 1 \AA above the highest point of the adsorbed surfaces.

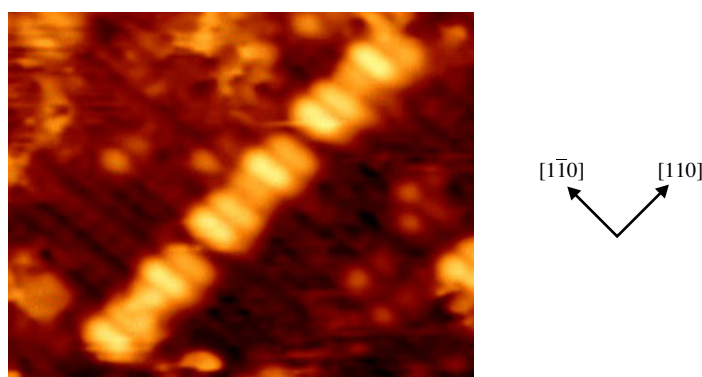


Figure 6.6: Filled-state STM image of perylene on Si(001)- 2×1 at low coverage recorded at a bias voltage of -2.225 V and 0.065 nA. The bright spots correspond to perylene molecules, the rows of weak spots indicate Si dimers.

is not uncommon that in STM experiments the contrast between two spots of different brightnesses is averaged out [135].

6.4 HREEL spectra

To allow for an unambiguous decision on the actual interface structure we compared calculated HREEL spectra for candidate structures to measured data (see right part of Fig. 6.7). To set up the dynamical matrix including the substrate influence on the vibrations we include the complete adsorbate and two substrate layers in these calculations, corresponding to 56 and 88 atoms for half and full monolayer coverage, thus resulting in a 168- and 264-dimensional Hessian, respectively. The obtained spectra for the half monolayer lo-CD-facing and lo-TD-facing as well as the full monolayer sh-CD-facing and lo-CD-zigzag models are shown in the left part of Fig. 6.7. Whereas the line shapes are similar in the high-frequency region that is dominated by C-H stretches in the adsorbate, there are pro-

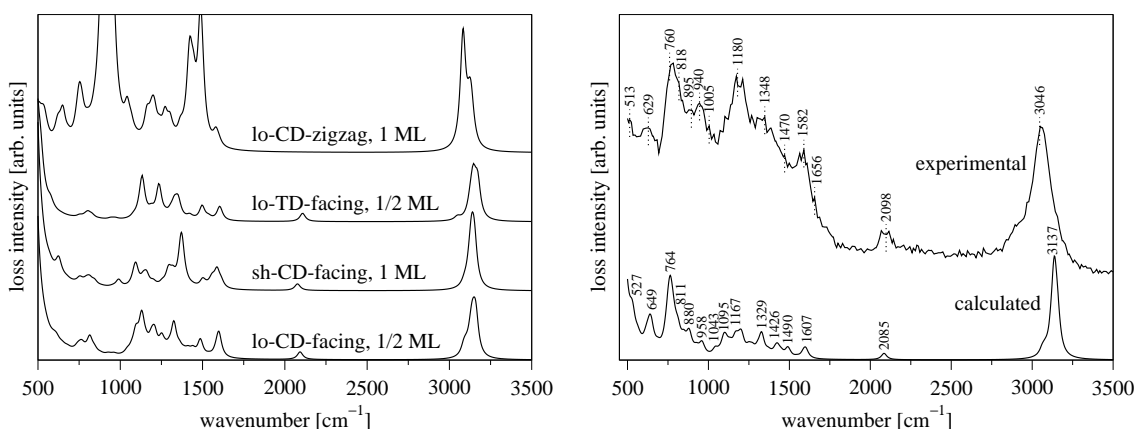


Figure 6.7: Left: Calculated HREEL spectra for selected models of adsorption of perylene on Si(001), right: experimental and calculated HREEL spectrum for the lo-CD-facing (1 ML) adsorption structure of perylene on Si(001). Important transitions are labeled with their respective wavenumbers.

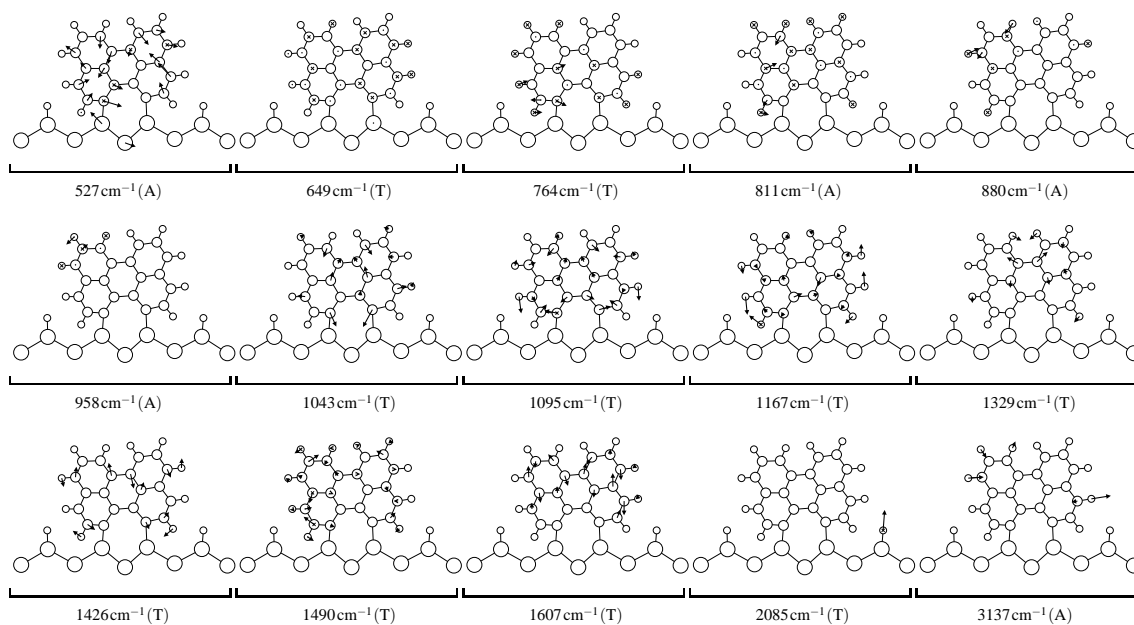


Figure 6.8: Sketch of the displacement patterns of the normal modes with strong oscillator strengths that contribute to the calculated HREEL spectrum of the full monolayer lo-CD-facing model of perylene on Si(001) with wavenumbers and their classification according to translation (T) or antisymmetry (A), see text for details of this scheme. Si (C, H) atoms are shown as large (medium, small) circles. Movements out of the perylene plane are depicted in such a way that atoms bearing dots (crosses) are displaced forwards (backwards). Atomic displacements in the perylene plane are indicated with arrows.

nounced differences between 500 cm^{-1} and 2000 cm^{-1} . None of the left spectra, however, bears even qualitative resemblances to the experimental spectrum. That leaves, from the structures considered here, only one structure that can possibly be the actual surface geometry. Indeed, the full monolayer lo-CD-facing model gives rise to a calculated HREEL spectrum (Fig. 6.7, right panel) which exhibits the same basic features as the experimental one and reproduces the line shape with good accuracy. We attribute the systematically lower oscillator strengths of the calculated spectrum in the region between 500 cm^{-1} and 1600 cm^{-1} to a homogeneous diffuse background due to unordered perylene molecules present in the experiment that are not included in our model. Nevertheless, for most of the peaks we can find a one-to-one correspondence between calculated and measured, a part of which will be discussed in the following with respect to the corresponding displacement patterns (and compared to those of the isolated molecule where applicable) that are shown in Fig. 6.8. In order not to overload the graphical representation the patterns in only one half of the surface unit cell seen in [110] direction are depicted. The movements in the other half can be derived by the newly introduced classification scheme of translation (T) and antisymmetry (A). This notation indicates that the individual vibrations in the two parts of the unit cell blend into each other by either a translation or a point reflection in the surface plane. The latter is to be understood in such a way that the vibrations of the two molecules are antisymmetric to each other with respect to a rotation by 180° around the surface normal. Note that this classification eases discussion

but is somewhat approximate because the perylene molecules are not inherently vibrationally coupled. This is especially true for the 649 cm^{-1} -mode and the 3137 cm^{-1} -mode where the amplitude of the normal mode vibration is larger in one molecule than in the other.

A first skim over the depicted patterns shows that not only the high-frequency modes, but also the low- and medium-frequency modes are dominated by vibrations within the adsorbate, contrary to the case of, e. g., benzene adsorbed on Si(001). The reason for this is the already mentioned softness of the perylene molecule as indicated by its pronounced low-frequency modes that are easily excited. In the following calculated frequencies are given in mid-text and experimental values in parentheses where a clear-cut assignment is possible. We find a notable Si-Si-stretch and a Si-C-bending type of vibration only in the A-mode at 527 cm^{-1} (513 cm^{-1}), but even here the adsorbate performs large-amplitude ring-deformations. The out-of-plane T-mode excited at 649 cm^{-1} (629 cm^{-1}) is at least partially similar to the B_{1u} -mode at 543 cm^{-1} of isolated perylene, Fig. 6.3. There are also out-of-plane vibrations of the Si-substrate atoms, albeit with small amplitude. The 811 cm^{-1} A-mode (818 cm^{-1}) of the system (a shoulder in the spectra) can be seen to come very close to the 817 cm^{-1} B_{1u} -mode of perylene in terms of the displacement pattern and frequency. The frequency shift is very small and as such indicative of the already strongly reduced substrate influence. The complicated ring-deformation present in the T-modes at 1043 cm^{-1} and 1095 cm^{-1} may both be derived from the 1045 cm^{-1} B_{3u} -mode of the isolated molecule where due to the interaction between the two molecules on the surface a frequency splitting has occurred. The C-H-bending vibrations of the 1490 cm^{-1} T-mode (1470 cm^{-1}) correspond almost exactly to those of the 1499 cm^{-1} B_{3u} -mode of perylene: these vibrations are not strongly affected by the distortion from planarity of the adsorbed molecules. Comparing frequencies, we relate the 1607 cm^{-1} T-mode (1582 cm^{-1} or 1656 cm^{-1}) to the 1601 cm^{-1} B_{3u} -mode of the isolated molecule. A close inspection reveals that in the latter the vibrations in the left and right part of the molecule are in phase, whereas in the former they are opposite in phase. Not surprisingly, the C-H-stretch excited at 3137 cm^{-1} can be traced back to the C-H-stretch at 3135 cm^{-1} (3046 cm^{-1}) of gas-phase perylene. As the two molecules on the surface interact with each other the displacement pattern does not reflect the D_{2h} symmetry like the corresponding mode of the gas-phase molecule. The mode that indicates hydrogen abstraction from perylene upon formation of the bonds to the surface is the Si-H-stretch mode at 2085 cm^{-1} (2098 cm^{-1}).

Chapter 7

Adenine adsorbed on Cu(110)

7.1 Single-molecule adenine on Cu(110)

7.1.1 Adsorption geometry and energy

The full geometry optimization starting with the adenine molecule (see Fig. 7.1(a)) lying flat above the Cu(110) surface with a vertical distance of 2.0 Å results in the structure schematically shown in Fig. 7.1(b). The potential energy surface (PES) sketched in Fig. 7.1(d) shows significant structures. For adenine the copper rows are separated by an

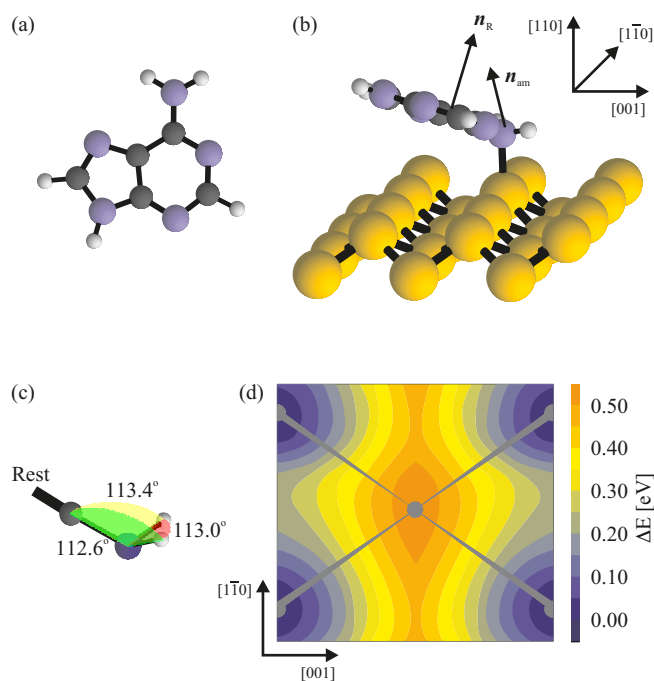


Figure 7.1: (a) Sketch of the adenine molecule and (b) the optimized adsorption geometry of adenine on Cu(110). Blue (dark gray, light gray, golden) spheres correspond to N (C, H, Cu) atoms. (c) Angles of amino-group pyramidalization of adsorbed adenine. (d) The potential energy surface (legend gives energy above the minimum; blue/red indicate favorable/unfavorable adsorption sites) seen by the adsorbed adenine molecule. The positions of the uppermost Cu atoms of one surface unit cell are indicated.

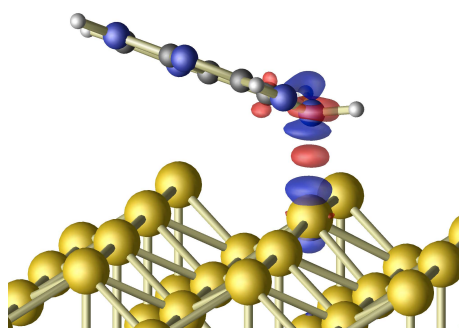


Figure 7.2: Total charge density difference plot. Regions of electron accumulation/depletion are displayed in blue/red, isosurface value: $\pm 0.02 e/\text{\AA}^3$. Note the slight elevation of the Cu atom the bond is established to.

energy barrier of about 0.5 eV, and the most favorable bonding position is reached when the amino-group nitrogen is directly above a copper atom. The N-Cu bonding direction has an off-axis angle of 2.9° with respect to the surface normal.

From Fig. 7.1(b) it can also be seen that the adsorbed adenine molecule in equilibrium position is noticeably deformed with respect to its nearly planar gas-phase structure [136, 137]. Upon bonding to Cu(110) the molecule assumes a strongly tilted geometry. The atoms of the molecule, save the two hydrogen atoms of the amino group, are fitted to a plane in the least-squares sense. The root-mean square deviation amounts to 0.03 Å. The normal vector of this least-squares plane corresponds to the vector of reference to define the tilting angle to the surface plane. The amino group NH_2 itself is bent by 17.7° and the rest of the molecule by 26.4° with respect to the plane of the Cu(110) surface.

In contrast to gas-phase adenine, the amino-group nitrogen is nearly tetrahedrally coordinated with angles ranging from 112.6° to 113.4° , see also Fig. 7.1(c). This is typical for sp^3 hybridized atoms with an sp^2 contribution. Indeed, the wave function analysis for nitrogen indicates nearly sp^3 hybridization ($\chi_s = 0.31$, $\chi_{p_x} = 0.23$, $\chi_{p_y} = 0.22$, $\chi_{p_z} = 0.24$). The computational results concerning the molecule tilting agree with the interpretation of vibrational spectroscopy experiments [30]. There are also small structural changes in the substrate: The Cu atom that bonds to the amino group moves out of the surface plane by 0.15 Å.

The Cu-N distance of 2.32 Å is consistent with the bond lengths in organometallic Cu-N complexes [138] and slightly larger than the length of 2.10 ... 2.13 Å reported for the respective bond of glycine adsorbed on Cu(110) [32, 139]. It certainly exceeds the sum of the covalent radii of Cu and N of about 1.8 Å. Therefore, the bond is unlikely to be covalent. This is corroborated by the wave function analysis (not shown here) which reveals no interface orbitals with clearcut bonding or antibonding character. Consistent with the large Cu-N distance, we calculate a relatively small adsorption energy $E_{\text{ad}} \equiv E_{\text{ads/subs}} - E_{\text{ads}} - E_{\text{subs}} = 0.34$ eV from the energies of the isolated (E_{ads} , E_{subs}) and the total system ($E_{\text{ads/subs}}$), indicating at first glance physisorption rather than chemisorption. There are presently no experimental data available on the adsorption energy. However, due to the deficiency of DFT-GGA to account for van der Waals interactions [140], the actual adsorption energy may be somewhat higher than the calculated 0.34 eV.

In order to elucidate the bonding behavior, we analyze the electron transfer by calculating the spatially resolved charge density difference

$$\Delta\rho(\mathbf{r}) = \rho_{\text{ads/subs}}(\mathbf{r}) - \rho_{\text{subs}}(\mathbf{r}) - \rho_{\text{ads}}(\mathbf{r}), \quad (7.1)$$

where $\rho_{\text{ads/subs}}$, ρ_{subs} and ρ_{ads} are the (negative) charge densities of the relaxed adsorbate-substrate system, of the clean relaxed surface and of the adsorbate without substrate, respectively. In complete analogy to Eqs. (3.4)–(3.5) in Chapter 3 we obtain the number of transferred electrons Q^\pm from which the Cartesian components d_i , $i = 1, 2, 3$, of the length of the dipole spanned by Q^+ and Q^- and the dipole moment components $p_i = |Q^\pm| d_i$ are derived. The adsorption-induced charge density difference is calculated with respect to the isolated molecule in the geometry of the adsorbed species. It is shown in Fig. 7.2. There is a net electron transfer from the molecule to the surface of $|Q^\pm| = 0.49 e$, where Q^+ and Q^- are separated by $\mathbf{d} = (-0.87, 0.02, 0.73) \text{ \AA}$, resulting in an overall dipole moment of $\mathbf{p} = (-2.02, 0.05, 1.73) \text{ D}$ with a square modulus of $|\mathbf{p}| = 2.66 \text{ D}$. Vector components are given parallel to the pairwise orthogonal $[001]$, $[1\bar{1}0]$, and $[110]$ directions, respectively; see Fig. 7.1.

The charge redistribution is related to the molecular structure. The atoms forming the 5- and 6-membered rings of adenine form a partially delocalized HOMO π -electron system confined to the molecule. The amino group is not part of a ring structure and contains a p_z -like lone-pair orbital which acts as the center of reactivity. In particular, the rehybridization of the nitrogen atom from sp^2 to sp^3 allows for easily transforming charge to the down side of the molecule, facing the Cu surface. This in turn polarizes the substrate. We will show in the following that this mutual polarization gives rise to electrostatic interactions that are largely responsible for the bonding between adenine and the metal surface.

7.1.2 Nature of the amino-group–metal bond

It is obvious from Fig. 7.2 that the charge redistribution cannot simply be explained in terms of ionic bonding. We therefore rationalize it by separately studying the substrate and molecule-related charge density changes in two virtual subsystems, denoted I and II, as indicated in Fig. 7.3. The dividing plane is placed half-way between Cu and N atoms.



Figure 7.3: Left: Decomposition in subsystems I and II (see text). Right: Charge-density difference with regions of electron accumulation/depletion displayed in blue/red, isosurface value: $\pm 0.02 e/\text{\AA}^3$, illustrating the dipole accompanying the structural changes in the substrate.

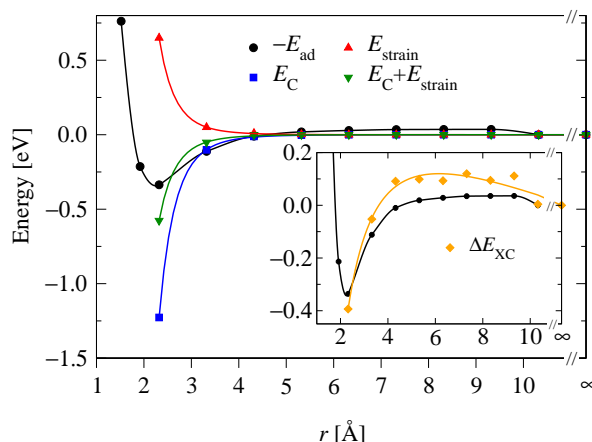


Figure 7.4: Negative adsorption energy (●), strain energy (▲), Coulomb energy (■), and sum of the latter (▼) for adenine adsorbed on Cu(110) as a function of the Cu-N distance. The inset shows the negative adsorption energy compared to the variation of the GGA exchange and correlation energy (◆). Solid lines are guides to the eye.

This allows for expanding the electrostatic interactions between the molecule and the substrate into a series of multipole terms. As an example, we show the adenine-adsorption induced substrate dipole in the right panel of Fig. 7.3. The choice of the dividing plane is not unique. Test calculations have shown, however, that the precise location of the plane is of minor importance.

The dipole moments in the two subsystems calculated according to the aforementioned procedure give rise to the interaction energy

$$E_{\text{dipole}} = \frac{(\mathbf{p}_I \mathbf{p}_II) R^2 - 3(\mathbf{p}_I \mathbf{R})(\mathbf{p}_II \mathbf{R})}{R^5}, \quad (7.2)$$

where \mathbf{R} is the distance vector between the two dipoles. Together with the monopole term from the overall charge transfer this accounts for the major part of the electrostatic interaction responsible for the bonding. In the equilibrium position one obtains for the total Coulomb energy $E_C = E_{\text{mono}} + E_{\text{dipole}} = -1.47 \text{ eV} + 0.24 \text{ eV} = -1.23 \text{ eV}$, i. e., the electrostatic interaction is dominated by the attractive ionic term, but modified by a mildly repulsive dipolar term.

Since the bonding of adenine on Cu(110) is the result of a complex interplay between structural changes and charge transfer within the constituents, we also have to bear in mind the deformation energies. They will reduce the overall energy gain. This has been pointed out already earlier for various hydrocarbons adsorbed on metal substrates, see, e. g., Refs. [141, 142]. In the equilibrium position it costs about $E_{\text{strain}} = 0.65 \text{ eV}$ strain energy to deform the “ideal” constituents into the final bonding geometry. Together with the electrostatics this results in a total energy gain upon adsorption of $E_C + E_{\text{strain}} = -0.58 \text{ eV}$. This value is of the same order of magnitude as the (negative) adsorption energy calculated from *first principles*.

Figure 7.4 shows the reaction pathway of adsorption, obtained by a series of constrained-dynamics calculations with increasing molecule-substrate distance, together with the aforementioned energy contributions. The reaction coordinate corresponds to

the Cu-N distance. If the molecule approaches the surface from infinity, there is a very small energy barrier that can easily be overcome at room-temperature. Starting at about 5 Å the amino group and the metal start to polarize each other, causing an attractive potential the molecule is subject to. As seen in Fig. 7.4, the sum of the attractive Coulomb interaction and the energy required to deform the molecule and the substrate account surprisingly well for the total (negative) adsorption energy until the equilibrium bonding distance is reached.

Obviously, the description of the chemical bonding in terms of such purely classical contributions cannot capture the complete physics of the interactions. This is illustrated in the inset of Fig. 7.4 where the difference of the GGA exchange and correlation energy relative to the isolated constituents is shown versus the bonding distance. We find a repulsive energy contribution for bonding distances larger than 3.5 Å and an attractive interaction for smaller distances. The magnitude, however, is clearly smaller than that of the Coulomb contribution discussed above. As discussed earlier, the wave function analysis shows that no major covalent bonding contributions to the total energy can be expected. We thus identify the Coulomb interaction as the main driving force for the bonding between the amino group and the copper surface.

While the revealed bonding mechanism constitutes an unexpected and interesting result in itself, it is not sufficient to explain the occurrence of self-assembled structures of distinctly oriented adenine chains on the Cu(110) surface. This question will be addressed in the following Section.

7.2 Adenine rows on Cu(110)

7.2.1 Adenine dimers

Due to the structure of adenine, see Fig. 7.1(a), there are a number of possible dimer structures stabilized by hydrogen bridges. In view of the revealed bonding mechanism of adenine to the Cu(110) surface in the above Section we concentrate on dimers in which the functional amino group does not participate in the hydrogen-bridge bonding so that it is left free to mediate the adsorbate-substrate bonding. The dimers considered here are prepared to initially exhibit C_2 symmetry. Each structure has been calculated and geometry-optimized in a $30 \text{ \AA} \times 30 \text{ \AA} \times 15 \text{ \AA}$ supercell to minimize possible dimer-dimer interactions. The resulting dimer geometries are shown in Fig. 7.5 where the denotation

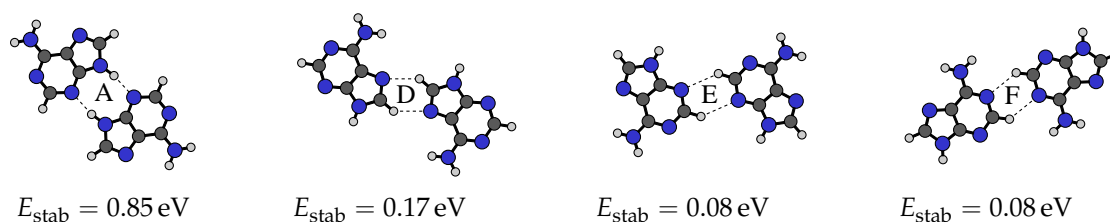


Figure 7.5: Geometries of adenine dimers stabilized by hydrogen bonds (indicated by dashed lines), nomenclature according to Ref. [30]. Blue (gray, white) spheres depict nitrogen (carbon, hydrogen) atoms. The stabilization energy E_{stab} per dimer is given below the respective sketch. The positive values signify energy gains upon dimerization.

follows Ref. [30]. It turns out that the initial C_2 symmetry of the dimer structures A, D, and E is broken in the relaxed geometries of which the different lengths of the hydrogen bonds are indicative: For the A-dimer one finds 1.84 Å and 1.85 Å, for the D-dimer 2.32 Å and 2.33 Å, and for E-dimer 2.54 Å and 2.55 Å. Only dimer F keeps the two-fold rotation symmetry with hydrogen bond lengths of 2.52 Å. Upon adsorption on the surface, however, the C_2 symmetry of the A dimer is recovered, but broken in case of the F dimer (see below). It should be noted that with the exception of dimer A the calculated hydrogen bond lengths somewhat exceeds the values typically found in compounds where this type of bonding plays a major role like in water or DNA [143].

The calculated stabilization energies (also given in Fig. 7.5) in this work lie between 0.08 eV and 0.85 eV and are consistent with the different hydrogen bond lengths: the longer the bond, the smaller the stabilization energy. The calculated values are, however, substantially larger than the values obtained by Chen and coworkers [30] who employed the semiempirical PM3 method [144] which is known to underestimate the strengths of hydrogen bonds, see, e. g., the discussion in Ref. [145]. In addition, the authors find the F dimer to be unstable while we obtain the same small energy gain of 0.08 eV as for the E-dimer.

7.2.2 Adsorption geometry and energy of dimer chains

The diffraction results from Ref. [30] indicate that, for saturation coverage, adenine forms a tightly packed molecular overlayer upon adsorption that is commensurate with the Cu(110) substrate. The surface unit cell, characterized by the matrix $\begin{pmatrix} 1 & 2 \\ 6 & 0 \end{pmatrix}$, contains two adenine molecules that register with the Cu substrate to form dimer chains along the (1,2) direction on the surface. Three possible molecular chains have been considered here, shown schematically in Fig. 7.6. The starting geometries were obtained from the corresponding dimer structures that were aligned to the copper surface with an overlayer–

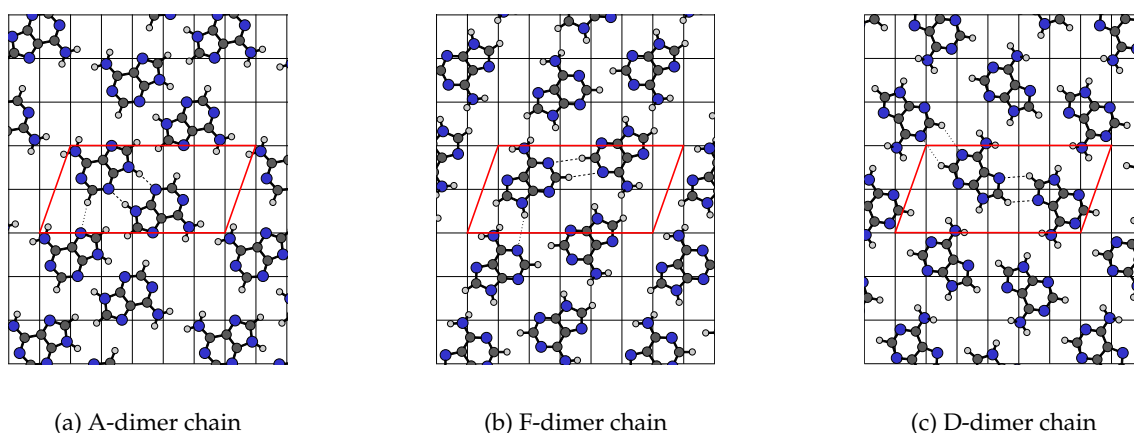


Figure 7.6: Three possible adenine-dimer chain structures emerging on the Cu(110) surface that is represented by 1×1 surface unit cells as black rectangles. Blue (gray, white) spheres depict nitrogen (carbon, hydrogen) atoms of the molecular overlayer. The corresponding unit cell is indicated by a red parallelogram, hydrogen bonds inside a unit cell by dashed lines, between unit cells by dotted lines.

Table 7.1: Calculated key structural parameters of the adenine-dimer chain structures on the Cu(110) surface studied here. $d_{\text{N}_{\text{am}}-\text{Cu}}^{(i)}$ denotes the vertical distance of the amino-group nitrogen atom to the uppermost Cu layer, $d_{\text{N}\dots\text{H}}^{(i)}$ the length of the hydrogen bridge bond in the unit cell, $\beta_{\text{surf}}^{(i)}$ the angle between the molecular plane (without amino group) and the Cu surface, and $\alpha_{\text{tilt}}^{(i)}$ the tilt angle between the amino group and the rest of the molecule, $i = 1, 2$. The superscript index 1 (2) refers to the left (right) molecule in the surface unit cell shown in Fig. 7.6. All lengths in Å, all angles in deg.

Parameter	A-dimer chain	F-dimer chain	D-dimer chain
$d_{\text{N}_{\text{am}}-\text{Cu}}^{(1)}$	3.11	5.31	6.09
$d_{\text{N}_{\text{am}}-\text{Cu}}^{(2)}$	3.11	6.01	6.09
$d_{\text{N}\dots\text{H}}^{(1)}$	1.91	2.89	2.32
$d_{\text{N}\dots\text{H}}^{(2)}$	1.91	2.91	2.30
$\beta_{\text{surf}}^{(1)}$	5.5	10.7	19.0
$\beta_{\text{surf}}^{(2)}$	5.9	8.0	18.9
$\alpha_{\text{tilt}}^{(1)}$	19.7	37.1	36.0
$\alpha_{\text{tilt}}^{(2)}$	20.9	38.1	35.9

substrate distance of 2.0 Å. The denotation is chosen in order to reflect that the dimerization in one unit cell is thought to be the main stabilization mechanism. The three models have in common that the registry with the underlying substrate takes place with the nitrogen atom of the amino group, in accordance with the proposed type of adenine-copper bonding in Sec. 7.1. Apart from that, they differ considerably.

The most pronounced difference concerns the distance between the molecular overlayer and the Cu substrate. As seen from Tab. 7.1, it ranges from 3.11 Å for the A-dimer chain to 6.09 Å for the D-dimer chain. While in case of the A-dimer chain the distances $d_{\text{N}_{\text{am}}-\text{Cu}}^{(i)}$, $i = 1, 2$, are larger than the 2.32 Å calculated in case of single-adenine adsorption on Cu(110), they come close to what is typical for physisorbed structures of organic molecules on metals [28]. On the other hand, the distances of more than 5.3 Å for the F-dimer and D-dimer chains are too large to be actually called bonds. Indeed, an energy minimum is assumed at the obtained geometries, but there are still substantial forces pushing the molecular overlayer away from the substrate. Thus these models correspond at best to metastable states and are discussed in the following mainly for the sake of completeness.

The lengths of the hydrogen bonds $d_{\text{N}\dots\text{H}}^{(i)}$, $i = 1, 2$, between the molecules in one unit cell increase with respect to the values of the free dimers, by the least amount for the A-dimer chain, namely from 1.85 Å or 1.84 Å to 1.91 Å. So only little rearrangement of the molecular overlayer is necessary in this case to achieve commensurateness with the copper substrate. Moreover, the registry with the surface leads again to the formation of C_2 -symmetric dimers. The small angles $\beta_{\text{surf}}^{(i)}$, $i = 1, 2$, between the surface plane and the molecular plane (without amino group) confirms that the initially flat overlayer stays

essentially flat. The special role of the amino group is recovered again in the adsorption structures. The amino groups are tilted by about 20° with respect to the rest of the molecule where the tilt angles $\alpha_{\text{tilt}}^{(i)}$, $i = 1, 2$, are obtained in the same way as explained in the first Section of this Chapter and illustrated in Fig. 7.1(b). Thus there occurs a partial rehybridization of the amino-group nitrogen atoms resulting in a tilting of the amino groups themselves, but the strong intramolecular hydrogen bonds in the A-dimer chain model prevent the rest of the adenine molecules in the unit cell from adopting a geometry more similar to the one found for single-molecule adsorption of adenine on Cu(110), see also Fig. 7.1.

Without discussing the other structures in detail we state that the deformations in the F-dimer and D-dimer chain overlayers are more substantial, see Tab. 7.1, although they adopt a planar geometry as isolated dimers as well. The F-dimer chain structure exhibits the particularity that the hydrogen atoms of the amino group of one molecule in a unit cell point up while those of the other amino group point down. For the A- as well as for the D-dimer chain structure both amino group hydrogen atoms point away from the surface. The formal registry of the adenine molecules with the underlying substrate, specifically of the amino-group nitrogen atom and the nearest Cu atom, is qualitatively comparable between the three models shown in Fig. 7.6. However, as mentioned above, the very large distances between adsorbate and substrate render these structures unlikely to appear in experiment.

Considering the total energies alone, the A-dimer chain structure is the most stable one. The F-chain model lies 0.78 eV and the D-chain model 0.53 eV higher in energy. The adsorption energies per molecule amount to 0.55 eV, 0.16 eV, and 0.28 eV for the A-, F-, and D-dimer chain models, respectively, which favors the A-chain structure as well. The reference to isolated adenine is considered to yield the most realistic value because the single-molecule reference system comes close to what is realized in the experiments where adenine is vapor-deposited at room-temperature. As can be seen from Fig. 7.6(a) the molecular overlayer structure of the A-chain model is stabilized both by the $\text{N} \cdots \text{H}$ hydrogen bonds between the molecules in one unit cell and by an additional $\text{N} \cdots \text{H}$ bridge between adjacent unit cells with a length of 2.66 Å. It is longer than typical hydrogen bonds, but comparable in length to those found for the isolated E and F dimers, Sec. 7.2.1, which resulted in an energy gain of about 0.08 eV. Thus the $\text{N} \cdots \text{H}$ bond present in the A-dimer chain model additionally stabilizes the resulting adsorption structure. The $\text{N} \cdots \text{H}$ bridge bonds extending over one unit cell in the F-dimer and D-dimer chain models, on the other hand, with lengths of 3.18 Å and 3.07 Å, respectively, are both too long to provide a non-zero energy contribution.

7.2.3 STM images

From the considerations above, the most likely overlayer geometry observed in experiment is indeed the A-dimer chain model. This is corroborated by the simulated STM images of the three dimer chain models shown in Fig. 7.7, obtained with the Tersoff-Hamann approach [134] as explained in Sec. 6.3. The flatness of the adsorbate in case of the A-dimer chain model allows to identify distinct features of the single molecules. The C_2 symmetry of the adenine dimer on the surface is reflected by the spot structure.

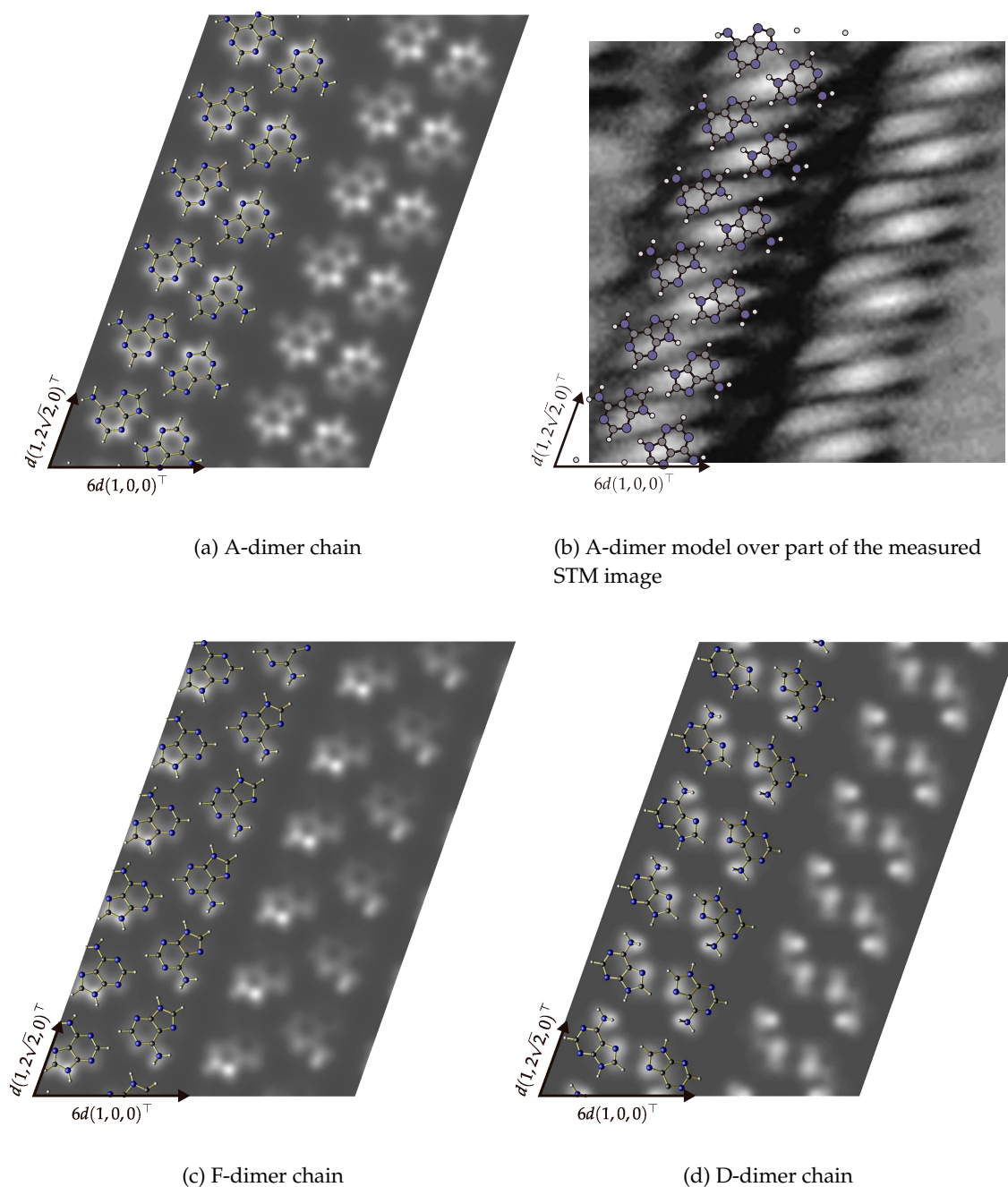


Figure 7.7: Simulated constant-height filled-state STM images [(a), (c), (d)] for three different adenine-dimer chain adsorption systems on Cu(110) at a bias voltage of -10 eV where the imaging plane is placed 1 Å above the highest point of the adsorbed surface. The corresponding structure of the molecular overlayer is superimposed on the respective image; for clarity substrate atoms are omitted. Blue (gray, white) spheres depict nitrogen (carbon, hydrogen) atoms in the adenine molecules. (b): Part of the experimental STM image (modified Fig. 5 from Ref. [30]) overlaid with the A-dimer chain model. Surface unit cell vectors (to scale) are indicated, given in Cartesian coordinates with the intrarow copper-atom spacing $d = 2.5716$ Å.

The brightest spots coincide with the functional NH groups present in the five- and six-membered rings. This sub-molecular resolution cannot be achieved in the experiment: As seen from Fig. 7.7(b), the spots corresponding to single molecules are smeared out, likely as a consequence of the scanning along the copper-row direction. However, we can state a good qualitative agreement between the measured alternating brightness pattern and the calculated spot structure, confirmed by the good fit of the suggested real space model to the spots in Fig. 7.7(b).

The spot structure of the F-dimer chain model, Fig. 7.7(c), asserts the loss of the rotational symmetry within one unit cell, hinted at already by the different $N \cdots H$ bond lengths (see above). While in the left one the density of states is maximal near the carbon atom of the C-H group in the five-membered ring and near the N atoms of the six-membered ring, the maximum brightness in the right molecule is located near the nitrogen atom of the amino group. Thus besides the loss of the C_2 symmetry the amino groups in the F-dimer chain structure become electronically inequivalent upon adsorption on the surface as a consequence of the already observed geometric inequivalency (see above). If it is taken into account that in addition the F-dimer structure gives rise to the smallest adsorption energy among the three models, it should be finally discarded.

Despite the slight difference of the $N \cdots H$ bond lengths of 0.02 \AA in the D-dimer chain model the integrated local density of states exhibits C_2 symmetry, at least approximately. The brightest spots are located at the amino group nitrogen atoms and at the doubly-bonded nitrogen atom of the five-membered ring. This gives rise to a spot structure that is nearly perpendicular to the measured one. Despite the problems associated with the comparison of simulated to experimental STM images [135] we consider the qualitative differences as substantial. Together with the geometrical objections we thus exclude the D-dimer chain structure as well. Summarizing, the structure and energetics in conjunction with the fingerprints from STM render the A-dimer chain model the most probable one.

Chapter 8

Summary

Already the interaction of the seemingly simple molecule methylchloride with the Si(001) surface gives rise to a variety of possible adsorption geometries with a strong tendency towards molecular dissociation and fragmentation. In dependence on the interface structure there are large differences with respect to the charge transfer characteristics. In addition, the surface dipole is shown to vary over a wide range which may open up the possibility of tuning, e. g., the work function of the system. The different types of bonding – covalent attachment after dissociation and/or fragmentation or physisorption – are manifested in the electronic bandstructures that predict semiconducting, semi-metallic, or metallic behavior of the respective systems. While the dispersion of the occupied surface states remains essentially unchanged upon adsorption of methylchloride, the unoccupied states are altered drastically in their character.

The calculations on the adsorption mechanisms of pyrrole on SiC surfaces elucidate two major reaction pathways: NH dissociation and subsequent covalent attachment of the pyrrole rest upon adsorption and physisorption of the non-dissociated molecule. The dissociative adsorption is found to be favored both from the calculations and from the experimental findings. Pronounced differences between both are, above the geometry distinction, the systematically lower adsorption energies of the latter which render their realization improbable at ambient conditions. Furthermore, the calculated final-state surface core-level shifts with respect to liquid pyrrole differ by about a factor of 2. The corresponding initial-state surface core-level shifts, however, not only show a large scatter in the values, but also magnitudes which apparently contradict the expectations from a chemistry point of view. For both the initial- and the final-state shifts the differences in the calculated values are traced back to the drastic changes the N1s state experiences upon extraction of a core electron which are not covered in either of these approaches to the determination of surface core-level shifts.

While the geometries of the clean Si-face of SiC(0001) or SiC(111) with $\sqrt{3} \times \sqrt{3}$ or 3×3 translational symmetries are well established and agreed upon, no such models exist for the corresponding C-faces. One partial aim of the efforts presented in this thesis was to use pyrrole to probe the surface composition of the 3×3 phase of the C-face: the x-ray photoemission spectra hint at the formation of a covalent N-Si bond and, as such, to the presence of Si at the C-face. Unfortunately, no definitive answer concerning the C-face geometry could be obtained by our efforts as yet. Notwithstanding, the idea of using

a small organic molecule as a probe for a surface structure might inspire further work on this topic. Required are well-controlled growth conditions during the preparation processes and well-characterized samples, at best by different experimental methods which complement each other and allow for the emergence of a complete picture the interpretation of which is aided by first-principles calculations. This combined approach offers opportunities for fruitful collaborations between theoreticians and experimentalists.

The proposed adlayer/adtrimer/adatom-model is sufficient to explain the instability of an ordered overlayer of pyrrole molecules because of the negative adsorption energy. But it is unlikely to show the complete picture because, from the preparation point of view, the amount of Si necessary for the formation of this structure seems to be too high.

The simple but accurate method for the calculation of the frequencies and the oscillator strengths of vibrational transitions introduced in Section 2.4 is applicable to systems with partial or full localization in the framework of density functional theory with periodic boundary conditions. The approach is suited for isolated molecules, exemplified by the application of the method to ammonia and benzene, as well as for extended surface geometries that can be described in a slab geometry like the benchmark system of benzene adsorbed on Si(001). Together with the frequencies and the displacement patterns of the calculated vibrations we are able to reproduce and predict IR and HREEL spectra including the correct relative intensities. Moreover, the results of these calculations also allow for a qualitative interpretation in the intuitive graphical picture of normal modes. It is demonstrated that the adsorbate may strongly influence the vibrational spectra. The method is helpful to unambiguously identify or discard suggested adsorption models by quantitatively and qualitatively interpreting the peak structure of experimental IR and HREEL spectra.

This is shown explicitly for the drastically more complicated system of perylene adsorbed on Si(001) which gives rise to a number of conceivable bonding geometries resulting in very different long-range orders concerning orientation and topology. The large number of degrees of freedom present in the system necessitates more than total-energy calculations. Adsorption energies alone are not sufficient to determine the most probably realized adsorption geometry because there may be large reaction barriers. Only the careful interpretation of scanning tunneling microscopy images in conjunction with measured and calculated HREEL spectra permits to single out and characterize the structure that occurs in experiment. The two perylene molecules in one surface unit cell bind in a cross-dimer arrangement after hydrogen abstraction from the long edge of the molecule where the molecule plane is perpendicular to the surface.

While the adsorption of organic molecules on semiconductor surfaces is mainly connected by the formation of covalent bonds, the situation is qualitatively different on metal surfaces where no directed bonds exist within or at the interface of the substrate. Nevertheless, the registry of the adsorbate occurs by attachment of functional groups in preferred sites determined by the topology and symmetry of the surface. In case of adenine adsorbed on Cu(110) a strongly directed interaction takes place between the lone pair of the amino-group nitrogen atom and the nearest top-layer Cu atom of the substrate. The calculated adsorption energy of 0.34 eV is clearly below the values typical for ionic or covalent bonds, but exceeds on the other hand the interaction energies known from van der Waals and even hydrogen bonds. On the basis of the charge transfer characteristics

we explain the bonding as resulting from the combined effects of electrostatic and strain contributions. The peculiar adsorption geometry with a strongly tilted adenine molecule results from the rehybridization of the amino-group nitrogen from sp^2 to sp^3 , related to the intramolecular charge transfer.

The self-organization of tightly packed adenine dimer chains in a commensurate overlayer structure on the Cu(110) surface is traced back to the stabilization by hydrogen bonds between two adenine molecules in one unit cell and between symmetry-equivalent molecules in adjacent cells. While the registry mechanism of the dimer chains is the same as for the single molecule adsorption, the adenine molecules in the most stable overlayer geometry remain essentially flat because the tendency towards strong tilting is counterbalanced by the intermolecular hydrogen bonds.

In this thesis fundamental adsorption mechanisms of molecules on solid surfaces have been examined by means of density-functional theory calculations to obtain adsorption geometries, bonding characteristics, bandstructures, charge transfer properties and, especially, fingerprints from STM and vibrational spectroscopy. On semiconductors like Si(001) or SiC the major reaction pathway is covalent attachment or, in other words, covalent immobilization: After adsorption the molecules stay fixed in a certain position and orientation. This is an advantage for the construction of, e. g., sensing devices that need a defined functionality in the interface region. The formation of covalent bonds is associated typically with large energy gains of the order of a few electron volts and, in dependence on the actual adsorption geometry, with drastically different electronic properties manifested in the bandstructure and in the variation of the surface dipole layer. The knowledge of these pronounced differences can be used to microscopically control the growth process. However, the strong interactions between adsorbate and substrate often hamper the formation of long-range ordered overlayers that can be characterized *in situ* by standard surface science techniques. On metals, on the other hand, long-range order is observed frequently because the molecules can be thought of to float on the electron-gas-like surface charge density with only little interaction between adsorbate and substrate, corresponding to relatively small adsorption energies. This opens up the possibility of molecular self-organization by the formation of extended overlayer networks, often with a surprisingly high symmetry that can be imaged easily by STM. The obvious disadvantage is the lack of precise control from the outside of what happens at the surface because of the high mobility within the actual overlayer. Therefore it is difficult from an application point of view to construct well-characterized devices with predictable and reproducible behavior. However, these systems serve well to study fundamental interactions at an atomic scale and thus constitute a playground for both experimentalists and theoreticians who have only just begun to chart a widely undiscovered land.

Bibliography

- [1] R. J. Hamers, *Nature* **412**, 489 (2001).
- [2] R. A. Wolkow, *Annu. Rev. Phys. Chem.* **50**, 413 (1999).
- [3] M. A. Filler and S. F. Bent, *Prog. Surf. Sci.* **73**, 1 (2003).
- [4] R. H. Friend, R. W. Gymer, A. B. Holmes, J. H. Burroughes, R. N. Marks, C. Taliani, D. D. C. Bradley, D. A. D. Santos, J. L. Bredas, M. Logdlund, and W. R. Salaneck, *Nature* **397**, 121 (1999).
- [5] S. F. Bent, *Surf. Sci.* **500**, 879 (2002).
- [6] S. F. Bent, *J. Phys. Chem. B* **106**, 2830 (2002).
- [7] R. A. Wolkow, *Annu. Rev. Phys. Chem.* **50**, 413 (1999).
- [8] M. H. Qiao, Y. Cao, J. F. Deng, and G. Q. Xu, *Chem. Phys. Lett.* **325**, 508 (2000).
- [9] G. T. Wang, C. Mui, C. B. Musgrave, and S. F. Bent, *J. Am. Chem. Soc.* **124**, 8990 (2002).
- [10] G. T. Wang, C. Mui, C. B. Musgrave, and S. F. Bent, *J. Phys. Chem. B* **105**, 12559 (2001).
- [11] Q. Chen and N. V. Richardson, *Nature Materials* **2**, 324 (2003).
- [12] S. Griessl, M. Lackinger, M. Edelwirth, M. Hietschold, and W. M. Heckl, *Single Mol.* **3**, 25 (2002).
- [13] S. Stepanow, M. Lingenfelder, A. Dmitriev, H. Spillmann, E. Delvigne, N. Lin, X. Deng, C. Cai, J. von Barth, and K. Kern, *Nature Materials* **3**, 229 (2004).
- [14] S. J. Sowerby, P. A. Stockwell, W. M. Heckl, and G. B. Petersen, *Origins Life Evol. B* **30**, 81 (2000).
- [15] M. W. Urban, *Vibrational Spectroscopy of Molecules and Macromolecules on Surfaces* (Wiley, 1994).
- [16] H. Ibach and D. L. Mill, *Electron energy loss spectroscopy and surface vibration* (Academic Press, 1982).
- [17] A. Zangwill, *Physics at Surfaces* (University Press, Cambridge, 1992).

- [18] A. M. Bradshaw and N. V. Richardson, *Pure & Appl. Chem.* **68**, 457 (1996).
- [19] K. A. Brown and W. Ho, *Surf. Sci.* **338**, 111 (1995).
- [20] M. J. Bronikowski and R. J. Hamers, *J. Vac. Sci. Technol. A* **13**, 777 (1995).
- [21] J. Y. Lee and S. Kim, *Surf. Sci.* **482**, 196 (2001).
- [22] M. Preuss, F. Bechstedt, W. G. Schmidt, J. Sochos, B. Schröter, and W. Richter, *Phys. Rev. B*, in production (2006).
- [23] D. Williams, *Med. Device Technol.* **14**, 10 (2003).
- [24] J. B. Gustafsson, E. Moons, S. M. Widstrand, and L. S. O. Johansson, *Surf. Sci.* **572**, 23 (2004).
- [25] Y. Hirose, S. R. Forrest, and A. Kahn, *Phys. Rev. B* **52**, 14040 (1995).
- [26] F. S. Tautz, M. Eremtchenko, J. A. Schaefer, M. Sokolowski, V. Shklover, and E. Umbach, *Phys. Rev. B* **65**, 125405 (2002).
- [27] M. Eremtchenko, J. A. Schaefer, and F. S. Tautz, *Nature* **425**, 602 (2002).
- [28] A. Hauschild, K. Karki, B. C. C. Cowie, M. Rohlfing, F. S. Tautz, and M. Sokolowski, *Phys. Rev. Lett.* **94**, 036106 (2005).
- [29] T. Rada, Q. Chen, and N. V. Richardson, *phys. stat. sol. (b)* **241**, 2353 (2004).
- [30] Q. Chen, D. F. Frankel, and N. V. Richardson, *Langmuir* **18**, 3219 (2002).
- [31] J. Hasselström, A. Föhlisch, O. Karis, N. Wassdahl, M. Weinelt, A. Nilsson, M. Nyberg, L. G. M. Pettersson, and J. Stöhr, *J. Chem. Phys.* **110**, 4880 (1999).
- [32] M. Nyberg, J. Hasselström, O. Karis, N. Wassdahl, M. Weinelt, A. Nilsson, and L. G. M. Pettersson, *J. Chem. Phys.* **112**, 5420 (2000).
- [33] M. Born and J. R. Oppenheimer, *Ann. Phys.* **84**, 457 (1927).
- [34] V. Fock, *Z. Physik* **61**, 126 (1930).
- [35] C. Møller and M. S. Plesset, *Phys. Rev.* **46**, 618 (1934).
- [36] L. H. Thomas, *Proc. Cambridge Philos. Soc.* **23**, 542 (1927).
- [37] E. Fermi, *Rend. Accad. Naz. Lincei* **6**, 602 (1927).
- [38] P. Hohenberg and W. Kohn, *Phys. Rev.* **136**, B864 (1964).
- [39] R. M. Dreizler and E. K. U. Gross, *Density Functional Theory* (Springer, Berlin, 1990).
- [40] R. P. Feynman, *Phys. Rev.* **56**, 340 (1939).
- [41] W. Kohn and L. J. Sham, *Phys. Rev.* **140**, A1133 (1965).
- [42] D. M. Ceperley and B. I. Alder, *Phys. Rev. Lett.* (1980).

- [43] J. P. Perdew and A. Zunger, *Phys. Rev. B* **23**, 5048 (1981).
- [44] M. Levy and J. P. Perdew, *Phys. Rev. A* **32**, 2010 (1985).
- [45] J. P. Perdew, *Electronic Structure of Solids '91* (Akademie-Verlag, Berlin, 1991).
- [46] J. P. Perdew, J. A. Chevary, S. H. Vosko, K. A. Jackson, M. R. Pederson, D. J. Singh, and C. Fiolhais, *Phys. Rev. B* **46**, 6671 (1992).
- [47] L. Hedin, *Phys. Rev.* **139**, A769 (1965).
- [48] F. Aryasetiawan and O. Gunnarsson, *Rep. Prog. Phys.* **61**, 237 (1998).
- [49] D. K. Ferry, *Semiconductor Transport* (Taylor & Francis, 2000).
- [50] L. P. Kouwenhoven, *Mesoscopic Electron Transport* (Springer, 1997).
- [51] G. Kresse and J. Furthmüller, *Comp. Mat. Sci.* **6**, 15 (1996).
- [52] G. Kresse and J. Furthmüller, *VASP – The Guide*.
<http://cms.mpi.univie.ac.at/vasp/>.
- [53] W. G. Schmidt, M. Preuss, P. H. Hahn, K. Seino, and F. Bechstedt, in *High Performance Computing in Science and Engineering Munich 2002* (Springer, Berlin, 2002).
- [54] W. G. Schmidt, K. Seino, M. Preuss, P. H. Hahn, and F. Bechstedt, in *Proceedings of the 2004 Symposium of the John von Neumann Institute for Computing* (NIC Directors, Jülich, 2003).
- [55] M. Preuss, K. Seino, and W. G. Schmidt, in *High Performance Computing in Science and Engineering Stuttgart* (Springer, Berlin, 2004).
- [56] D. R. Hamann, M. Schlüter, and C. Chiang, *Phys. Rev. Lett.* **43**, 1494 (1979).
- [57] G. B. Bachelet, D. R. Hamann, and M. Schlüter, *Phys. Rev. B* **26**, 4199 (1982).
- [58] G. P. Kerker, *J. Phys. C* **13**, L189 (1980).
- [59] N. Troullier and J. L. Martins, *Phys. Rev. B* **43**, 1993 (1991).
- [60] J. Furthmüller, P. Käckell, F. Bechstedt, and G. Kresse, *Phys. Rev. B* **61**, 4576 (2000).
- [61] G. Kresse and D. Joubert, *Phys. Rev. B* **59**, 1758 (1998).
- [62] P. E. Blöchl, *Phys. Rev. B* **50**, 17953 (1994).
- [63] R. M. Martin, *Phys. Rev. B* **9**, 1998 (1974).
- [64] H. J. Monkhorst and J. D. Pack, *Phys. Rev. B* **13**, 5188 (1976).
- [65] P. H. Hahn, W. G. Schmidt, and F. Bechstedt, *Phys. Rev. B* **72**, 245425 (2005).
- [66] F. Bechstedt, *Principles of Surface Physics* (Springer, Berlin, 2003).
- [67] J. A. Appelbaum and D. R. Hamann, *Phys. Rev. B* **8**, 1777 (1973).

- [68] J. A. Appelbaum and D. R. Hamann, *Rev. Mod. Phys.* **48**, 3 (1976).
- [69] F. Bechstedt and R. Enderlein, *Semiconductor Surfaces and Interfaces* (Akademie-Verlag, Berlin, 1988).
- [70] R. Leitsmann, L. E. Ramos, and F. Bechstedt, *Phys. Rev. B* **74**, 085309 (2006).
- [71] K. Shiraishi, *J. Phys. Soc. Jpn.* **59**, 3455 (1990).
- [72] S. G. Louie, private communication (2006).
- [73] K. Aflatooni, G. A. Gallup, and P. D. Burrow, *J. Phys. Chem. A* **102**, 6205 (1998).
- [74] I. Hargittai and M. Hargittai, *Symmetry through the Eyes of a Chemist* (Wiley-VCH, New York, 1987).
- [75] W. Ludwig and C. Falter, *Symmetries in Physics* (Springer, Berlin, Heidelberg, New York, 1988).
- [76] R. P. Feynman, *Phys. Rev.* **56**, 340 (1939).
- [77] E. B. Wilson, J. C. Decius, and P. C. Cross, *Molecular Vibrations* (McGraw-Hill, 1955).
- [78] G. Kern, G. Kresse, and J. Hafner, *Phys. Rev. B* **59**, 8551 (1999).
- [79] S. Baroni, S. de Gironcoli, A. D. Corso, and P. Giannozzi, *Rev. Mod. Phys.* **73**, 515 (2001).
- [80] F. A. Hamprecht, A. J. Cohen, D. J. Tozer, and N. C. Handy, *J. Chem. Phys.* **109**, 6264 (1998).
- [81] L. Benco, J. Hafner, F. Hutschka, and H. Toulhoat, *J. Phys. Chem. B* **107**, 9756 (2003).
- [82] K. R. Kganyago and P. E. Ngoepe, *Mol. Sim.* **22**, 39 (1999).
- [83] P. Pulay, *Chem. Phys. Lett.* **73**, 393 (1980).
- [84] D. M. Wood and A. Zunger, *J. Phys. A* **18**, 1343 (1985).
- [85] F. Bechstedt, P. Käckell, A. Zywietz, K. Karch, B. Adolph, K. Tenelsen, and J. Furthmüller, *phys. stat. sol. (b)* **202**, 35 (1997).
- [86] P. Käckell, J. Furthmüller, and F. Bechstedt, *Diamond Relat. Mater.* **6**, 1346 (1997).
- [87] J. Dabrowski and H.-J. Müssig, *Silicon Surfaces and Formation of Interfaces* (World Scientific, Singapore, 2000).
- [88] P. Krüger and J. Pollmann, *Phys. Rev. Lett.* **74**, 1155 (1995).
- [89] A. H. Romero, C. Sbraccia, P. L. Silvestrelli, and F. Ancilotto, *J. Chem. Phys.* **119**, 1085 (2003).
- [90] J. P. Perdew, K. Burke, and M. Ernzerhof, *Phys. Rev. Lett.* **77**, 3865 (1996).

- [91] A. D. Becke, *Phys. Rev. A* **38**, 3098 (1988).
- [92] C. Lee, W. Yang, and R. C. Parr, *Phys. Rev. B* **37**, 785 (1988).
- [93] W. Mönch, *Semiconductor Surfaces and Interfaces* (Springer, Berlin, 1995).
- [94] A. Ramstad, G. Brocks, and P. J. Kelly, *Phys. Rev. B* **51**, 14504 (1995).
- [95] M. Schlüter, J. R. Chelikowsky, S. G. Louie, and M. L. Cohen, *Phys. Rev. B* **12**, 4200 (1975).
- [96] W. G. Schmidt, F. Bechstedt, and G. P. Srivastava, *Surf. Sci. Rep.* **25**, 141 (1996).
- [97] C. Hogan, D. Paget, Y. Garreau, M. Sauvage, G. Onida, L. Reining, P. Chiaradia, and Corradini, *Phys. Rev. B* **68**, 205313 (2003).
- [98] K. Seino, W. G. Schmidt, and F. Bechstedt, *Phys. Rev. B* **69**, 245309 (2004).
- [99] P. Krüger and J. Pollmann, *Phys. Rev. B* **47**, 1898 (1993).
- [100] S. Lizzit, A. Baraldi, A. Groso, K. Reuter, M. V. Ganduglia-Pirovano, C. Stampfl, M. Scheffler, M. Stichler, C. Keller, W. Wurth, and D. Menzel, *Phys. Rev. B* **63**, 205419 (2001).
- [101] T. Koopmans, *Physica* **1**, 104 (1934).
- [102] L. Köhler and G. Kresse, *Phys. Rev. B* **70**, 165405 (2004).
- [103] M. Gajdoš, A. Eichler, and J. Hafner, *Surf. Sci.* **531**, 272 (2003).
- [104] R. Chen, *J. Mater. Sci.* **11**, 1521 (1976).
- [105] H.-J. Butt, K. Graf, and M. Kappl, *Physics and Chemistry of Interfaces* (Wiley-VCH, 2003).
- [106] J. J. Randall and M. H. F. Wilkins, *Proc. Roy. Soc. London A* **366**, 390 (1945).
- [107] M. Sabisch, P. Krüger, and J. Pollmann, *Phys. Rev. B* **55**, 10561 (1997).
- [108] J. Furthmüller, F. Bechstedt, H. Hüsken, B. Schröter, and W. Richter, *Phys. Rev. B* **58**, 13712 (1998).
- [109] J. Furthmüller, P. Käckell, F. Bechstedt, A. Fissel, K. Pfennighaus, B. Schröter, and W. Richter, *J. Electron. Mater.* **27**, 848 (1998).
- [110] U. Starke, J. Schardt, J. Bernhardt, M. Franke, K. Reuter, H. Wedler, K. Heinz, J. Furthmüller, P. Käckell, and F. Bechstedt, *Phys. Rev. Lett.* **80**, 758 (1998).
- [111] L. I. Johansson, P.-A. Glans, and N. Hellgren, *Surf. Sci.* **405**, 288 (1998).
- [112] S. Nakanishi, H. Tokutaka, K. Nishimori, S. Kishida, and N. Ishihara, *Appl. Surf. Sci.* **41**, 44 (1989).

- [113] M. Hollering, J. Bernhardt, J. Schardt, A. Ziegler, R. Graupner, B. Mattern, A. P. J. Stampfl, U. Starke, K. Heinz, and L. Ley, *Phys. Rev. B* **58**, 4992 (1998).
- [114] I. Forbeaux, J.-M. Themlin, A. Charrier, F. Thibaudau, and J.-M. Debever, *Appl. Surf. Sci.* **162**, 406 (2000).
- [115] U. Starke, *Mat. Sci. Forum* **353**, 205 (2001).
- [116] H. E. Hoster, M. A. Kulakov, and B. Bullemer, *Surf. Sci.* **382**, L658 (1997).
- [117] L. Li and I. S. T. Tsong, *Surf. Sci.* **351**, 141 (1996).
- [118] G.-X. Qian, R. M. Martin, and D. J. Chadi, *Phys. Rev. B* **38**, 7649 (1988).
- [119] K. Seino, W. G. Schmidt, J. Furthmüller, and F. Bechstedt, *Phys. Rev. B* **66**, 235323 (2002).
- [120] W. G. Schmidt, P. Käckell, and F. Bechstedt, *Surf. Sci.* **357–358**, 545 (1996).
- [121] R. C. West (ed.), *Handbook of Chemistry and Physics* (Chemical Rubber Company, Boca Raton, FL, 1984), 65th edn.
- [122] F. A. Cotton, *Chemical Applications of Group Theory* (Wiley, 1990), 3rd edn.
- [123] G. Herzberg, *Infrared and Raman Spectra of Polyatomic Molecules*, vol. 2 of *Molecular Spectra and Molecular Structure* (van Nostrand, 1959).
- [124] G. P. Lopinski, D. J. Moffatt, and R. A. Wolkow, *Chem. Phys. Lett.* **282**, 305 (1998).
- [125] U. Birkenheuer, U. Gutdeutsch, and N. Rösch, *Surf. Sci.* **409**, 213 (1998).
- [126] M. J. Kong, A. V. Teplyakov, J. G. Lyubovitsky, and S. F. Bent, *Surf. Sci.* **411**, 286 (1998).
- [127] K. Okamura, Y. Hosoi, Y. Kimura, H. Ishii, and M. Niwano, *Appl. Surf. Sci.* **237**, 439 (2004).
- [128] K. W. Self, R. I. Pelzel, J. H. G. Owen, C. Yan, W. Widdra, and W. H. Weinberg, *J. Vac. Sci. Technol. A* **16**, 1031 (1998).
- [129] M. Staufer, U. Birkenheuer, T. Belling, F. Nörtemann, N. Rösch, W. Widdra, K. L. Kostov, T. Moritz, and D. Menzel, *J. Chem. Phys.* **112**, 2498 (2000).
- [130] M. Rumi, G. Zerbi, and K. Müllen, *J. Chem. Phys.* **108**, 8662 (1998).
- [131] A. Hermann, W. G. Schmidt, and F. Bechstedt, *J. Phys. Chem. B* **109**, 7928 (2005).
- [132] M. Preuss and F. Bechstedt, *Phys. Rev. B* **73**, 155413 (2006).
- [133] R. Miotto, M. C. Oliveira, M. M. Pinto, F. de León-Pérez, and A. C. Ferraz, *Phys. Rev. B* **69**, 235331 (2004).
- [134] J. Tersoff and D. R. Hamann, *Phys. Rev. B* **31**, 805 (1985).

- [135] W. A. Hofer, *Prog. Surf. Sci.* **71**, 147 (2003).
- [136] M. Preuss, W. G. Schmidt, K. Seino, J. Furthmüller, and F. Bechstedt, *J. Comp. Chem.* **25**, 112 (2004).
- [137] P. Pulay, S. Saebo, M. Malagoli, and J. Baker, *J. Comp. Chem.* **26**, 599 (2005).
- [138] T. P. Balasubramanian, P. T. Muthiah, Ananthasaravanan, and S. K. Mazumdar, *J. Inorg. Biochem.* **63**, 175 (1996).
- [139] J. Hasselström, O. Karis, M. Weinelt, N. Wassdahl, A. Nilsson, M. Nyberg, L. G. M. Pettersson, M. G. Samant, and J. Stöhr, *Surf. Sci.* **407**, 221 (1998).
- [140] O. A. von Lilienfeld, I. Tavernelli, U. Rothlisberger, and D. Sebastiani, *Phys. Rev. Lett.* **93**, 153004 (2004).
- [141] A. Nilsson and L. G. M. Pettersson, *Surf. Sci. Rep.* **55**, 49 (2004).
- [142] L. Triguero, L. G. M. Pettersson, B. Minaev, and H. Ågren, *J. Chem. Phys.* **108**, 1193 (1998).
- [143] P. H. Hahn, W. G. Schmidt, K. Seino, M. Preuss, F. Bechstedt, and J. Bernholc, *Phys. Rev. Lett.* **94**, 037404 (2005).
- [144] J. J. P. Stewart, *J. Comput. Chem.* **10**, 209 (1989).
- [145] B. Kallies and R. Mitzner, *J. Mol. Model.* **1**, 68 (1995).

Publications

Some results contained in this thesis have been published in the following articles:

1. **M. Preuss**, F. Bechstedt, W. G. Schmidt, J. Sochos, B. Schröter, W. Richter
Clean and pyrrole-functionalized Si- and C-terminated SiC surfaces: First-principles calculations of geometry and energetics compared with LEED and XPS
Phys. Rev. B, in production (2006)
2. **M. Preuss**, R. Miotto, F. Bechstedt, T. Rada, N. V. Richardson, W. G. Schmidt
Structure, energetics, and vibrational spectra of perylene adsorbed on Si(001): First-principles calculations compared with STM and HREELS
Phys. Rev. B **74**, 115402 (2006), selected for Virtual Journal of Nanoscale Science & Technology 14 (12) (2006)
3. **M. Preuss** and F. Bechstedt
Vibrational spectra of ammonia, benzene, and benzene adsorbed on Si(001) by first-principles calculations with periodic boundary conditions
Phys. Rev. B **73**, 155413 (2006)
4. W. G. Schmidt, K. Seino, **M. Preuss**, A. Hermann, F. Ortmann, F. Bechstedt
Organic molecule adsorption on solid surfaces: chemical bonding, mutual polarisation and dispersion interaction
Appl. Phys. A **85**, 387 (2006)
5. K. V. Emtsev, Th. Seyller, L. Ley, L. Broekmann, A. Tadich, J. D. Riley, R. G. C. Leckey, **M. Preuss**
Correlation effects at ideal SiC(0001)-1x1 surfaces
Phys. Rev. B **73**, 075412 (2006)
6. K. V. Emtsev, Th. Seyller, L. Ley, A. Tadich, L. Broekman, J. D. Riley, R. G. C. Leckey, **M. Preuss**
Electronic properties of clean unreconstructed 6H-SiC(0001) surfaces studied by angle resolved photoelectron spectroscopy
Surf. Sci. **600**, in press (2006)

7. **M. Preuss**, W. G. Schmidt, F. Bechstedt
Coulombic Amino Group-Metal Bonding: Adsorption of Adenine on Cu(110)
Phys. Rev. Lett. **94**, 236102 (2005), selected for Virtual Journal of Nanoscale Science & Technology 11 (25) (2005)
8. **M. Preuss**, W. G. Schmidt, K. Seino, F. Bechstedt
Methylchloride adsorbed on the Si(001) surface: an ab-initio study
Appl. Surf. Sci. **234**, 155 (2004)
9. **M. Preuss**, W. G. Schmidt, F. Bechstedt
Methyl Chloride Adsorption on Si(001) – Electronic Structure
J. Phys. Chem. B **108**, 7809 (2004)
10. P. H. Hahn, W. G. Schmidt, K. Seino, **M. Preuss**, F. Bechstedt, J. Bernholc
Optical absorption of water: Coulomb effects versus hydrogen bonding
Phys. Rev. Lett. **94**, 037404 (2005), selected for Virtual Journal of Biological Physics Research 9(3) (2005)
11. **M. Preuss**, W. G. Schmidt, K. Seino, J. Furthmüller, F. Bechstedt
Ground- and excited-state properties of DNA base molecules from plane-wave calculations using ultrasoft pseudopotentials
J. Comp. Chem. **25**, 112 (2004)
12. K. Seino, W. G. Schmidt, **M. Preuss**, F. Bechstedt
Uracil Adsorbed on Si(001): Structure and Energetics
J. Phys. Chem. B **107**, 5031 (2003)
13. W. G. Schmidt, **M. Preuss**, P. H. Hahn, K. Seino, F. Bechstedt
Optical Response of Semiconductor Surfaces and Molecules Calculated From *First Principles*, in *High Performance Computing in Science and Engineering Munich 2002*, pages 259–268. Springer, Berlin, 2002
14. W. G. Schmidt, P. H. Hahn, K. Seino, **M. Preuss**, F. Bechstedt
Gas-Phase Epitaxy Grown InP(001) Surfaces From Real-Space Finite-Difference Calculations, in *High Performance Computing in Science and Engineering Stuttgart 2003*, pages 155–166. Springer, Berlin, 2003
15. W. G. Schmidt, K. Seino, **M. Preuss**, P. H. Hahn, F. Bechstedt
Silicon Surfaces Functionalized with Organic Molecules: Uracil Adsorption as a Prototypical Example, in *Proceedings of the 2004 Symposium of the John von Neumann Institute for Computing*, pages 205–214. NIC Directors, Jülich, 2003

16. **M. Preuss**, K. Seino, W. G. Schmidt
DNA Base Properties from First Principles Plane-Wave Calculations, in *High Performance Computing in Science and Engineering Munich 2004*, pages 349–362. Springer, Berlin, 2004
17. **M. Preuss**, K. Seino, W. G. Schmidt
Methylchloride Adsorption on Si(001) – Electronic Properties, in *High Performance Computing in Science and Engineering Stuttgart 2004*, pages 115–128. Springer, Berlin, 2004

Some results contained in this thesis have been presented in oral or poster form at the following conferences and workshops:

1. Dresden, Germany, March 24th – 28th (2003), Spring Meeting of the German Physical Society (poster)
2. Madrid, Spain, September 15th – 19th (2003), 9th International Conference on the Formation of Semiconductor Interfaces (talk)
3. Isola Polvese, Italy, September 30th – October 2nd (2003), Heimbach seminar “Adsorbates on surfaces”, organized by the surface science group of Prof. W. Richter (em.), TU Berlin (talk)
4. Regensburg, Germany, March 8th – 12th (2004), Spring Meeting of the German Physical Society (talk)
5. Venice, Italy, June 28th – July 2nd (2004), 12th International Conference on Solid Surfaces (poster)
6. Berlin, Germany, March 4th – 9th (2005), Spring Meeting of the German Physical Society (poster)
7. Berlin, Germany, September 4th – 9th (2005), 23rd European Conference on Surface Science (talk)
8. Brasília, Brazil, February 13th – 15th (2006), Symposium on Electronic Structure and Molecular Dynamics (talk)
9. Dresden, Germany, March 27th – 31th (2006), Spring Meeting of the German Physical Society (talk)
10. Paris, France, September 4th – 8th (2006), 24th European Conference on Surface Science (poster)

Zusammenfassung

Bereits die Wechselwirkung des scheinbar einfachen Moleküls Methylchlorid mit der Si(001)-Oberfläche gibt Anlaß zu einer Vielzahl möglicher Adsorptionsgeometrien. Molekulare Dissoziation und Fragmentierung sind die bevorzugten Reaktionswege. In Abhängigkeit von der Struktur der Grenzschicht treten große Unterschiede in den Charakteristika des Ladungstransfers hervor. Der Oberflächendipol variiert über einen großen Bereich, so daß die Möglichkeit besteht, etwa die Austrittsarbeit des Systems zu beeinflussen. Die unterschiedlichen Bindungsarten – kovalente Anlagerung nach Dissoziation oder Fragmentierung bzw. Physisorption – zeigen sich deutlich in der elektronischen Bandstruktur, die halbleitendes, halbmetallisches und metallisches Verhalten der jeweiligen Strukturen vorhersagt. Während die Dispersion der besetzten Zustände im wesentlichen gleich bleibt, ändert sich der Charakter der unbesetzten Zustände nach der Adsorption von Methylchlorid deutlich.

Die Rechnungen zum Adsorptionsmechanismus von Pyrrol auf SiC-Oberflächen ergeben zwei Hauptreaktionswege: Dissoziation der NH-Gruppe und kovalente Anlagerung des Molekülrests sowie Physisorption des nicht-dissoziierten Moleküls. Die dissoziierte Adsorption stellt sich seitens Theorie und Experiment als bevorzugt heraus. Deutliche Unterschiede zwischen den beiden Reaktionspfaden bestehen, über die Geometrie hinaus, in den systematisch geringeren Adsorptionsenergien der physisorbierten Strukturen, die ihr Auftreten bei Raumtemperatur unwahrscheinlich erscheinen lassen. Darüber hinaus unterscheiden sich die berechneten Oberflächen-Rumpfniveaueverschiebungen bezüglich flüssigen Pyrrols unter Berücksichtigung von Endzustandseffekten um etwa den Faktor 2. Die entsprechenden Verschiebungen im Anfangszustandsbild hingegen streuen nicht nur stark, sondern haben Werte, die den Erwartungen aus chemischer Sicht zuwiderlaufen. In beiden Fällen werden die Unterschiede der Verschiebungen auf drastische Änderungen des N1s-Zustandes nach Entfernung eines Rumpfelektrons zurückgeführt, die in der vorliegend verwendeten Berechnungsmethode auch im Endzustandsbild nicht in ausreichendem Maße berücksichtigt werden.

Während die Geometrien der Si-Seite der reinen SiC(0001)- bzw. SiC(111)-Oberflächen in der $\sqrt{3} \times \sqrt{3}$ - und 3×3 -Rekonstruktion gut untersucht und durch Modelle erklärt worden sind, gibt es bislang keine allgemein anerkannten Strukturvorschläge für die C-Seite. Ein Ziel dieses Teils der vorliegenden Dissertation bestand darin, zur Aufklärung der C-Seiten-Struktur mit Hilfe des Pyrrolmoleküls als Sonde beizutragen: Die Röntgenphotoemissionsspektren deuten auf die Bildung einer kovalenten N-Si-Bindung hin und somit auf die Präsenz von Si auf der C-Seite. Es konnte jedoch bislang kein eindeutiges Modell der C-Seiten-Struktur erhalten werden. Nichtdestoweniger

könnte die Idee, ein kleines organisches Molekül als Sonde für eine Oberflächenstruktur zu verwenden, weitere Arbeiten auf diesem Gebiet anstoßen. Dazu werden kontrollierbare Wachstumsbedingungen während der Präparation und gut charakterisierte Proben benötigt, am besten durch verschiedene, einander ergänzende experimentelle Methoden, die zu einem vollständigen Bild führen, das mit parameterfreien Rechnungen interpretiert werden kann. Dieser kombinierte Ansatz bietet vielfältige Möglichkeiten für die fruchtbare Zusammenarbeit zwischen Theoretikern und Experimentatoren.

Das in diesem Teil der Dissertation vorgeschlagene Ad-Schicht/Ad-Trimer/Ad-Atom-Modell der C-Seite reicht aus, die Instabilität einer geordneten Pyrrolage zu erklären, denn die berechnete Adsorptionsenergie ist negativ. Dennoch kann das Modell nicht vollständig sein, weil aus Sicht der Probenpräparation die zur Bildung der Struktur benötigte Menge Si zu groß ist.

Die einfache, aber genaue Methode zur Berechnung der Frequenzen und Oszillatorstärken von Schwingungsübergängen, die in Abschnitt 2.4 eingeführt wurde, ist anwendbar für Systeme mit teilweise und vollständiger Lokalisierung. Der Ansatz eignet sich für isolierte Moleküle, beispielhaft gezeigt durch Anwendung der Methode auf Ammoniak und Benzol, und für ausgedehnte Oberflächensysteme, die in einer Slabgeometrie beschrieben werden wie das prototypische Adsorptionssystem Benzol/Si(001). Zusammen mit den Frequenzen und den Auslenkungsmustern der berechneten Schwingungsmoden können vollständige IR- und HREEL-Spektren reproduziert und vorhergesagt werden. Darüber hinaus erlauben die Ergebnisse dieser Berechnungen auch eine qualitative Interpretation im anschaulichen Bild der Normalmoden. Es wird gezeigt, daß das Substrat die Schwingungsspektren stark beeinflussen kann. Die Methode ermöglicht die eindeutige Identifikation vorgeschlagener Adsorptionsmodelle durch die quantitative und qualitative Auswertung experimenteller Schwingungsspektren.

Dies gilt insbesondere für das deutlich kompliziertere Adsorptionssystem Perylen/Si(001), das viele mögliche Bindungsgeometrien zuläßt, die sich deutlich in der langreichweitigen Ordnung hinsichtlich Orientierung und Topologie unterscheiden. Wegen der zahlreichen Freiheitsgrade des Systems sind mehr als reine Gesamtenergierechnungen nötig, denn Adsorptionsenergien allein reichen nicht aus, um die wahrscheinlichste Adsorptionsgeometrie zu ermitteln. Nur die genaue Auswertung von STM-Aufnahmen in Verbindung mit gemessenen und berechneten HREEL-Spektren erlaubt schließlich die Bestimmung der tatsächlich realisierten Struktur. Die beiden Perylenmoleküle in der Oberflächeneinheit zelle binden nach Wasserstoffabstraktion an der langen Molekülseite in einer Kreuzdimergeometrie, wobei die Molekülebene senkrecht zur Oberfläche steht.

Während die Adsorption organischer Moleküle auf Halbleiteroberflächen hauptsächlich mit der Bildung kovalenter Bindungen einhergeht, stellt sich die Situation auf Metalloberflächen deutlich anders dar. Hier existieren keine gerichteten Bindungen im Substrat bzw. in der Grenzflächenregion. Dennoch binden Adsorbatsmoleküle bzw. deren funktionelle Gruppen an sogenannten bevorzugten Plätzen, die durch die Oberflächensymmetrie und -topologie vorgegeben sind. Im Falle von Adenin/Cu(110) besteht eine gerichtete Wechselwirkung zwischen dem einsamen Elektronenpaar des Stickstoffatoms der Aminogruppe und dem nächstgelegenen Cu-Atom der obersten Lage des Substrats. Die berechnete Adsorptionsenergie von 0.34 eV liegt klar unterhalb der für ionische oder kovalente Bindungen typischen Werte,

aber oberhalb der üblicherweise für reine Dispersionswechselwirkungen auftretenden. Basierend auf den Charakteristika des Ladungstransfers wird die Bindung erklärt mit dem gemeinsamen Einfluß elektrostatischer und deformationsbedingter Beiträge. Die ungewöhnliche Adsorptionsgeometrie des stark verkippten Adeninmoleküls entsteht aus der Rehybridisierung des Stickstoffatoms der Aminogruppe von sp^2 zu sp^3 , die wiederum auf intramolekularen Ladungstransfer zurückgeführt wird.

Die Selbstorganisation dichtgepackter Adenin-Dimer-Ketten in einer mit dem Substrat kommensurablen Überstruktur auf der Cu(110)-Oberfläche erklärt sich aus stabilisierenden Beiträgen von Wasserstoffbrückenbindungen zwischen den Adeninmolekülen in einer Einheitszelle und zwischen benachbarten Zellen. Obwohl sich wie beim Einzelmolekül gerichtete Bindungen zwischen dem Stickstoffatom der Aminogruppe und dem nächstgelegenen Substratatom ausbilden, bleibt die Molekülschicht insgesamt im wesentlichen flach, weil der Tendenz zur Aufrichtung des Adeninrests die intermolekularen Wasserstoffbrückenbindungen entgegenstehen.

In dieser Dissertation wurden grundlegende Mechanismen der Adsorption von Molekülen auf Festkörperoberflächen mit Hilfe der Dichtefunktionaltheorie untersucht, um Adsorptionsgeometrien, Bindungscharakteristika, Bandstrukturen, Ladungstransfers und insbesondere Rastertunnelaufnahmen und Schwingungsspektren zu erhalten. Auf Halbleitern wie Si(001) oder SiC herrscht die kovalente Anlagerung vor oder, mit anderen Worten, die kovalente Immobilisierung: Nach der Adsorption bleiben die Moleküle in einer bestimmten Position und Orientierung fixiert. Dies bietet einen Vorteil für die Konstruktion etwa von Sensoren, die eine definierte Funktionalität in der Grenzschichtregion verlangen. Die Bildung kovalenter Bindungen ist typischerweise mit großen Energiegewinnen in der Größenordnung mehrerer Elektronenvolt verbunden. Darüber hinaus zeigen sich, in Abhängigkeit von der jeweiligen Adsorptionsgeometrie, große Unterschiede der elektronischen Eigenschaften, die sich in der Bandstruktur und in der Variation der Oberflächendipolschicht niederschlagen. Die Kenntnis derartiger Unterschiede kann zur mikroskopischen Kontrolle des Wachstumsprozesses verwendet werden. Allerdings behindern die starken Wechselwirkungen zwischen Adsorbat und Substrat häufig die Bildung langreichweitig geordneter Moleküllagen, die mit Standardmethoden der Oberflächenphysik *in situ* kontrolliert werden können. Auf Metallen hingegen wird oft eine langreichweitige Ordnung beobachtet, weil die Moleküle auf der elektro-nengasähnlichen Substratladungsdichte schweben, wobei die Wechselwirkung zwischen Adsorbat und Substrat eher gering und daher mit entsprechend kleinen Adsorptionsenergien verknüpft ist. Dies ermöglicht Selbstorganisation auf molekularer Ebene, bei der sich ausgedehnte Überstrukturen mit einer oftmals hohen Symmetrie bilden, die leicht mit der Rastertunnelmikroskopie abgebildet werden können. Der offensichtliche Nachteil besteht in der nur schlecht von außen zu gewährleistenden Kontrolle über die an der Oberfläche stattfindenden Prozesse als Folge der hohen Beweglichkeit innerhalb der Moleküllage. Dies erschwert die Konstruktion gut charakterisierter Bauelemente mit vorhersagbarem und reproduzierbarem Verhalten. Ungeachtet dessen dienen derartige System zur Untersuchung grundlegender Wechselwirkungen auf atomarer Ebene und stellen daher eine Spielwiese sowohl für Experimentatoren als auch für Theoretiker dar, die gerade erst begonnen haben, ein nahezu unentdecktes Land zu kartographieren.

Lebenslauf

Name	Martin Preuß
Geburtstag	5. November 1976
Geburtsort	Stadthagen
Familienstand	ledig
Staatsangehörigkeit	deutsch
Eltern	Angelika Preuß, geb. Berewinkel Egbert Preuß
1983 – 1989	Grundschule und Orientierungsstufe Obernkirchen
1989 – 1996	Gymnasium Bückeburg
05/1996	Abitur, Gesamtnote: 1,0
08/1996 – 09/1997	Zivildienst in der DRK-Sozialstation Obernkirchen
10/1997 – 09/2002	Studium der Physik an der Friedrich-Schiller-Universität Jena
09/2002	Diplom, Prädikat: mit Auszeichnung Thema der Diplomarbeit: “ <i>Ab-initio</i> -Berechnungen von Grund- und Anregungseigenschaften der DNA-Basen Adenin, Cytosin, Guanin und Thymin” (Betreuer: Dr. Wolf Gero Schmidt, Prof. Dr. Friedhelm Bechstedt)
10/2002 – heute	Arbeit an der Dissertation bei Dr. Wolf Gero Schmidt und Prof. Dr. Friedhelm Bechstedt, Friedrich-Schiller-Universität Jena
seit 10/2002	wissenschaftlicher Mitarbeiter am Institut für Festkörpertheorie und -optik im Rahmen des DFG-Projekts “Organic functionalization of semiconductor surfaces” (SCHM-1361/6)

Ehrenwörtliche Erklärung

Ich erkläre hiermit ehrenwörtlich, daß ich die vorliegende Arbeit selbständig, ohne unzulässige Hilfe Dritter und ohne Benutzung anderer als der angegebenen Hilfsmittel und Literatur angefertigt habe. Die aus anderen Quellen direkt oder indirekt übernommenen Daten und Konzepte sind unter Angaben der Quelle gekennzeichnet.

Bei der Auswahl und Auswertung des Materials haben mir die nachstehend aufgeführten Personen in der jeweils beschriebenen Weise unentgeltlich geholfen:

1. Prof. Dr. Friedhelm Bechstedt (als betreuender Hochschullehrer),
2. Prof. Dr. Wolf Gero Schmidt (als Betreuer der Promotion bis zum 31.08.2005).

Weitere Personen waren an der inhaltlich-materiellen Erstellung der vorliegenden Arbeit nicht beteiligt. Insbesondere habe ich hierfür nicht die entgeltliche Hilfe von Vermittlungs- bzw. Beratungsdiensten (Promotionsberater oder andere Personen) in Anspruch genommen. Niemand hat von mir unmittelbar oder mittelbar geldwerte Leistungen für Arbeiten erhalten, die im Zusammenhang mit dem Inhalt der vorgelegten Dissertation stehen.

Die Arbeit wurde bisher weder im In- noch im Ausland in gleicher oder ähnlicher Form einer anderen Prüfungsbehörde vorgelegt.

Die geltende Promotionsordnung der Physikalisch-Astronomischen Fakultät ist mir bekannt.

Ich versichere ehrenwörtlich, daß ich nach bestem Wissen die reine Wahrheit gesagt und nichts verschwiegen habe.

Jena, den 9. November 2006

Thesen zur Dissertation
Ab-Initio Investigations of
Fundamental Adsorption Mechanisms
of Organic Molecules on Solid Surfaces
von Dipl.-Phys. Martin Preuß

1. Unter geeigneten Präparationsbedingungen entstehen geordnete Strukturen organischer Moleküle auf Festkörperoberflächen. Wegen der großen Anzahl an Freiheitsgraden gibt es eine Vielzahl denkbarer Adsorptionsgeometrien, die lokalen Energieminima auf der Hyperfläche der potentiellen Energie entsprechen. Erst begleitende parameterfreie Rechnungen erlauben die Einschätzung der realisierten Strukturen hinsichtlich ihrer Stabilität.
2. Die Dichtefunktionaltheorie (DFT) mit einem Basissatz ebener Wellen ermöglicht systematische, auskonvergierte Rechnungen, so daß Energiedifferenzen mit einer Genauigkeit im Bereich weniger Millielektronenvolt pro Einheitszelle angegeben werden können. Abgeleitete Größen wie Dipolmomente und Schwingungsfrequenzen stimmen mit gemessenen Werten mit einer Abweichung von weniger als 5% überein.
3. Auf Siliziumoberflächen wird eine langreichweitige Ordnung hauptsächlich bei Alkenen beobachtet, die Zykoadditionsprodukte mit den Siliziumdimeren an der Oberfläche bilden, aber auch bei dissoziativen und koordinativen Reaktionsmechanismen.
4. Elektronische Bandstrukturen zeigen die Dispersion von Volumen- und Oberflächenzuständen in der Brillouin-Zone. Ein einfaches Molekül wie Methylchlorid auf Si(001) führt in Abhängigkeit von der Bindungsgeometrie zu Zuständen im fundamentalen Gap, die zu halbleitenden und metallischen Oberflächen Anlaß geben.
5. Obwohl die Valenzelektronen der Atome die Hauptbeiträge zu den chemischen Bindungen liefern, spüren auch die Rumpfelektronen kleinste Änderungen des effektiven äußeren Potentials, denen wiederum Änderungen der chemischen Umgebung des Atoms zugeordnet werden. Daher reagieren die Rumpfniveaus der Atome eines Adsorbats empfindlich auf eine Modifikation des Bindungscharakters im Vergleich zu einem Referenzsystem.
6. Das 1s-Rumpfniveau des Stickstoffatoms im Pyrrolmolekül kann als Sonde verwendet werden, um Informationen über die Oberflächenstruktur der polaren Seiten des Halbleiters SiC zu erhalten, da das Substrat keinen Stickstoff enthält. Gemessene Röntgenphotoelektronenspektren des Stickstoff-1s-Niveaus deuten auf die Bildung einer kovalenten Stickstoff-Silizium-Bindung auf der C-Seite der SiC(0001)-Oberfläche hin. Die erhaltenen Strukturmodelle und berechneten Rumpfniveaushiftungen favorisieren eine siliziumreiche C-Seiten-Struktur.
7. Wichtige experimentelle oberflächenempfindliche Methoden zur Symmetrie- und Strukturaufklärung von Adsorbaten sind Infrarot- und Elektronenverlustspektroskopie, die die Schwingungseigenschaften des System sondieren. In dieser Arbeit wird eine Methode vorgestellt und angewandt, um neben Schwingungsfrequenzen und Auslenkungsmustern der Normalmoden auch die Intensitäten der

Schwingungsübergänge im Rahmen der Dichtefunktionaltheorie mit periodischen Randbedingungen sowohl für Gasphasenmoleküle als auch für Adsorbate zu berechnen. Die so bestimmten Infrarotspektren für die isolierten Moleküle Ammoniak und Benzol stimmen hervorragend mit gemessenen Spektren überein. Die vollständige Symmetrieanalyse der erhaltenen Normalmoden anhand gruppentheoretischer Überlegungen belegt, daß die Auswahlregeln für elektrische Dipolstrahlung auch numerisch erfüllt sind.

8. Das prototypische aromatische Molekül Benzol adsorbiert bevorzugt in der sogenannten Schmetterlingsgeometrie auf der Si(001)-Oberfläche unter Bildung eines Zykloadditionsprodukts. Die langreichweitig geordnete Struktur erlaubt die Modellierung mittels der DFT und die Berechnung vollständiger hochauflösender Elektronenverlustspektren. Der Vergleich zum Experiment zeigt die Eignung der Methode zur Bestimmung der Oszillatorstärken der Schwingungsübergänge auch für kompliziertere ausgedehnte Systeme. Im niedrigeren Frequenzbereich wird der Einfluß des Substrats auf die Schwingungen des Adsorbats deutlich.
9. Perylen besteht aus fünf verschmolzenen Kohlenstoffringen. Da es im Schwingungsspektrum des isolierten Moleküls Normalmoden mit sehr kleinen Frequenzen gibt, ist Perylen trotz der hohen D_{2h} -Symmetrie leicht deformierbar. Wegen der Komplexität des Adsorbatsystems Perylen/Si(001) und möglicher hoher Reaktionsbarrieren reichen Gesamtenergierechnungen nicht aus, um die an der Grenzschicht realisierte Struktur eindeutig festzustellen.
10. Der Vergleich simulierter und gemessener Rastertunnelmikroskopieaufnahmen für das System Perylen/Si(001) schränkt die Anzahl möglicher Adsorptionsgeometrien ein, doch erst die vollständigen Schwingungsspektren ermöglichen eine endgültige Aussage. Danach binden die beiden Perylenmoleküle in der Flächeneinheit zelle nach Wasserstoffabstraktion an der langen Molekülseite in einer Kreuzdimergeometrie, wobei die Molekülebene senkrecht zur Oberfläche steht.
11. Bei Verwendung von Metalloberflächen ist die Wechselwirkung zwischen Adsorbat und Substrat schwächer, so daß durch Selbstorganisation ausgedehnte geordnete Moleküllagen auftreten können. Intermolekulare Wasserstoffbrückenbindungen stabilisieren dabei die Molekülschicht.
12. Das DNA-Basenmolekül Adenin nimmt auf der Cu(110)-Oberfläche eine ungewöhnliche Adsorptionsgeometrie an, in der sich die Aminogruppe und der Rest des Moleküls gegeneinander verkippen, so daß der Molekülrest einen Winkel von 26° mit der Kupferoberfläche einschließt. Es besteht eine attraktive, gerichtete Wechselwirkung mit dem Substrat zwischen dem nahezu tetraedrisch koordinierten Stickstoffatom der Aminogruppe des Adeninmoleküls und dem nächstliegenden Kupferatom der Oberfläche. Die Bindungsenergie von 0.34 eV pro Molekül wird erklärt mit dem gemeinsamen Einfluß elektrostatischer und deformationsbedingter Beiträge.
13. Die Selbstorganisation der Adeninmoleküle auf der Kupferoberfläche zu Dimerketten wird getrieben durch die Entstehung von Wasserstoffbrückenbindungen zwischen den Adeninmolekülen innerhalb der Einheitszelle der mit dem Substrat kommensurablen Überstruktur einerseits und zwischen benachbarten Zellen andererseits. Die dadurch erfolgende Stabilisierung verhindert ein starkes Aufstellen der Moleküle in der Schicht. Der Energiegewinn durch die Bildung der Molekülschicht beträgt 0.55 eV pro Molekül.